

**Construction and testing of a
realistic head phantom for
assessment of radiofrequency power
deposition in MRI**

Diplomarbeit

Christoph Leuze

* 13. November 1980 in Tübingen

Hauptfach: Physik / Diplom

Matrikelnummer: 9175740

Gutachter: Prof. Dr. Robert Turner
Prof. Dr. Josef Käs

Eingereicht: September 2008

Universität Leipzig, Institut für Physik und Geowissenschaften
&
Max Planck Institut für Kognitions- und Neurowissenschaften



MAX-PLANCK-GESELLSCHAFT

Contents

Appendix	1
1 Introduction	1
2 MRI basics	5
2.1 Overview	5
2.2 Spin physics	5
2.2.1 Resonance theory	5
2.2.2 Expectation Value equations of motion	7
2.2.3 Macroscopic Magnetization	8
2.2.4 Rotating frame of reference	8
2.2.5 Pulse shape	11
2.2.6 Transmit field B^+ and receive field B^-	12
2.2.7 Magnetic field strength \mathbf{H} and magnetic field \mathbf{B}	13
2.2.8 Relaxation Process and Bloch-equations	14
2.2.9 Free induction decay	16
2.2.10 Hahn Echo	16
2.2.11 Chemical shift	18
2.3 Image formation in MRI	22
2.3.1 Gradient Echo (GRE)	22
2.3.2 RF	25
2.3.3 Slice selection	25
2.3.4 Phase encoding	26
2.3.5 Frequency encoding	27
2.3.6 Signal	28

3	Phantoms	29
3.1	Overview	29
3.2	Materials	30
3.2.1	T_1 estimation	30
3.2.2	Examples of aqueous phantoms used in these studies . . .	33
3.2.3	Usage and properties of different gelling agents	35
3.2.4	Influence of the gelling agent on the B_1^+ distribution within phantom	39
3.2.5	Permittivity and conductivity modifiers	40
3.2.6	Preparation of a head phantom	44
3.2.7	Measuring the electrical parameters	49
3.3	Summary	55
4	B_1^+ field inhomogeneities	57
4.1	Overview	57
4.2	Reasons for B_1^+ field inhomogeneities	57
4.2.1	Problems at high fields	57
4.2.2	Electromagnetic waves inside medium	58
4.2.3	Damping	59
4.2.4	Explanations for B_1^+ field inhomogeneities - depending upon the conductivity of the sample	60
4.3	Overview of different B_1^+ mapping methods	66
4.3.1	Nominal and actual flip angle	66
4.3.2	Double angle method using Gradient Echo	67
4.3.3	Double angle method using Spin-Echo	71
4.3.4	Double angle method with saturation pulse and EPI readout	74
4.3.5	Multi angle approach	74
4.3.6	B_1^+ mapping method from SIEMENS Work-in-progress (WIP) package	77
4.3.7	Method using the signal null at 180°	79
4.3.8	Pulsed steady-state method	82
4.4	Summary	83
5	Hardware	85

5.1	Overview	85
5.2	Adjustable parameters for a simple GRE experiment	86
5.3	Performance comparison between coils	94
5.3.1	Input power - flip angle	95
5.4	Scanner adjustments and pulse shape	97
5.4.1	Comparison between the different adjustment methods	98
5.4.2	Validity of adjustment and pulse shape	99
5.5	Summary	102
6	B_1^+ field comparison	105
6.1	Overview	105
6.2	Simulations	107
6.2.1	Simulation programs	108
6.2.2	Reasons for asymmetries	109
6.3	Comparison procedure	110
6.3.1	Acquiring a 3D object and the position of the phantom	112
6.3.2	Comparison software	119
6.4	Magnitude comparison: Simulation and Experiment	125
6.4.1	Sinc pulse approximation	127
6.4.2	Pulse length according to the IDEA Poet Simulation	129
6.4.3	Acquiring the slices with a rectangular pulse	132
6.4.4	Loss between TALES and coil	133
6.4.5	Relation load - magnitude H_1^+ field	136
6.4.6	Influence of the mesh size used for the simulations	137
6.5	Profile comparison for several phantoms	138
6.6	Summary	151
7	Conclusion	153
	Appendix	157
.1	MatLab scripts	157
.1.1	Permutebox.m	157
.1.2	Import.m	158
.2	Productlist	159

List of figures	160
List of tables	165
References	167

Chapter 1

Introduction

Since the first days of magnetic resonance imaging, there has been a drive to increase the strength of the magnetic field acting within the operating system. Within the last 30 years, the strength of the magnetic field used for invivo studies has increased from 0.2 T to over 7 T . While scanners with field strengths of 3 T are already widely available also in clinical use, the new high-field standard of 7 T and field strengths even above, are still being explored just for scientific purposes.

One of the advantages of these high field strengths is the improved signal to noise ratio (SNR), which increases approximately linearly with the magnetic field strength. MRI techniques such as high resolution fMRI, which have reached their limits concerning SNR at the lower field strengths can be greatly improved at these higher field strengths.

Unfortunately, the improvements that come with these higher field strengths are accompanied by a number of problems which appear at stronger magnetic fields. Electromagnetic radiation in the RF range is necessary for the excitation of the protons during an MRI experiment. The frequency of this radiation is linearly proportional to the magnetic field strength. Since the energy of an electromagnetic wave is proportional to its frequency, a human subject in a 7 T scanner is exposed to higher amounts of energy than in a scanner operating at lower magnetic field strengths. Additionally the higher frequency comes along with a shorter wavelength of the radiation. Due to a slower propagation velocity of the RF radiation

in the human tissue, for $7T$ the wavelength approaches the size of organs such as the human brain. This may result in the interferences of the electromagnetic waves inside the human body. Besides the problem that these inhomogeneities, resulting from the interferences, pose on the image quality, they might result in an excessive power absorption of a certain area and therefore heating of the affected tissue.

As a result of these problems, there is a legal limit, the so called *SAR limit*, which regulates the maximum amount of electromagnetic radiation during a certain time, that a human subject may be exposed to during an MRI experiment. Since the behaviour of the electromagnetic radiation inside the human subject is not yet fully understood, this limit has been naturally set very low to exclude any possible harmful effects to the subject. The drawback of this low SAR limit is the restriction of imaging sequences using high power RF pulses, which therefore cannot tap their full potential at higher field strengths. Hence, only a limited number of new insights are possible. Many scientists therefore desire a better examination of the effect of the RF field on the subject and, if it proves to be safe for the subject, an increase of this SAR limit.

State-of-the-art simulations already can provide some very good information about the distribution of the electromagnetic field inside an examined object. It is the motivation of this thesis to provide experimental evidence for the simulations and verification of the simulation data.

A technique known as B_1^+ *mapping* is used, which makes it possible to visualize the disposition of the RF field, also called the B_1^+ *field*, inside the examined object. To exactly match the experiments with the simulations, the examined objects need to consist of well defined materials with well known parameters. For this purpose, so-called *phantoms* are constructed. These are models which resemble human organs, in this case the human brain, in the most realistic manner necessary. For some purposes they less realistic approximations such as simple water bottles are preferred. For other purposes they need to be more realistic, consisting of different gel types in the shape and with the electromagnetic properties of the human head.

It is necessary to find a reliable modality for comparing simulation and experimental data. This method can then be applied first for simpler phantoms. These

investigations are necessary for understanding the imaging coils that send and receive the electromagnetic waves, and for understanding the operation of the scanner. Secondly, there is a need for the construction of realistic head models, which may assist in the understanding of the behaviour of the electromagnetic field inside the human head. No commercial models are available for experiments and comprehensive research is lacking so far concerning the construction of head models suitable for MRI which incorporate the anatomy and electromagnetic properties of the human head. Accordingly, the development of a realistic head model will be required for the gathering of valuable experimental data.

Chapter 2

MRI basics

2.1 Overview

In *Spin physics* section 2.2, a short introduction on the general physical principles of MRI given. How can a spin and the behavior in a magnetic field be described? Which processes lead to the formation of a signal? How does the chemical environment influence the behavior of the spins?

In *Image formation in MRI* section 2.3, the example of a simple Gradient Echo sequence is given. With the help of a sequence timing diagram, the different components of the sequence such as the RF pulse and gradients are described.

2.2 Spin physics

2.2.1 Resonance theory

Depending on their inner structure, subatomic particles such as the nuclei of atoms possess a total magnetic moment μ and total angular momentum \mathbf{J} [Slichter, 1992]. These two vectors are parallel and their relation is given by:

$$\mu = \gamma \mathbf{J} \tag{2.1}$$

where γ is a scalar called the “gyromagnetic ratio”. The value of γ depends on the specific nucleus and the sensitivity during an experiment increases for higher values of γ . The highest value of γ in nature belongs to the single proton. This is a fortune for MRI technology as single protons, namely Hydrogen atoms, are the most abundant atoms in the human body.

In quantum theory \mathbf{J} is defined by a dimensionless angular momentum operator \mathbf{I} :

$$\mathbf{J} = \hbar \mathbf{I}. \quad (2.2)$$

The z-component I_z of the angular momentum operator has the eigenvalues m with m being any of the $2I + 1$ values $m = I, I - 1, \dots, -I$. I is also called the spin quantum number and can have the either integer or half-integer values, depending on whether the atom has an even or odd number of protons and neutrons.

The application of a magnetic field \mathbf{B}_0 results in an interaction between the magnetic moment and the field which can be described by the Hamiltonian:

$$\mathcal{H} = -\boldsymbol{\mu} \mathbf{B}_0 \quad (2.3)$$

Taking the field to be \mathbf{B}_0 along the z-direction, the Hamiltonian writes

$$\mathcal{H} = -\gamma \hbar B_0 I_z. \quad (2.4)$$

The eigenvalues of this Hamiltonian provide the allowed energy values, which are simply multiples of the eigenvalues of I_z :

$$E = -\gamma \hbar B_0 m \quad m = I, I - 1, \dots, -I \quad (2.5)$$

In the MRI experiments, that will be described in the course of this thesis, just the single proton will be considered. Since a proton has a spin of $I = 1/2$ it can occupy two different energy levels for $m = \pm 1/2$, resulting in an energy difference between the two levels (Fig. 2.1) of

$$\Delta E = \gamma \hbar B_0 \quad (2.6)$$

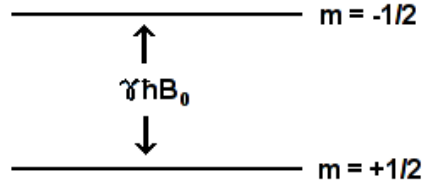


Figure 2.1: The two energy levels of the hydrogen atom.

This is then the energy which has to be provided to cause a transition between the two adjacent levels.

During an experiment this transition is accomplished by applying an alternating magnetic field B_1 with the frequency ω_0 perpendicular to the static field B_0 . With equation (2.6) this frequency is then given by:

$$\Delta E = \hbar\omega_0 \implies \omega_0 = \gamma B_0 \quad (2.7)$$

The frequency ω_0 is also called the *Larmor frequency*, which describes the precession frequency of a magnetic moment about an external magnetic field.

2.2.2 Expectation Value equations of motion

Now the time variation of the expectation value of μ under the influence of a magnetic field B will be considered. For this purpose, the commutator relation

$$[I_i, I_j] = i\varepsilon_{ijk}I_k \quad (2.8)$$

is used, with ε_{ijk} being ± 1 for $i \neq j \neq k$ and 0 otherwise. With $I_{x,y,z}$ having no explicit time dependence, it can be shown that the following holds for the time dependence of the angular momentum operator [Slichter, 1992]:

$$\frac{dI_x}{dt} = \gamma(B_z I_y - B_y I_z) \quad (2.9)$$

$$\frac{dI_y}{dt} = \gamma(B_x I_z - B_z I_x) \quad (2.10)$$

$$\frac{dI_z}{dt} = \gamma(B_y I_x - B_x I_y) \quad (2.11)$$

These equations are the component equations of the vector operator equation

$$\frac{d\mathbf{I}}{dt} = \gamma \mathbf{I} \times \mathbf{B} \quad (2.12)$$

Therefore, since $\boldsymbol{\mu} = \gamma \hbar \mathbf{I}$, the following holds for the expectation value of the magnetic moment:

$$\frac{d\langle \boldsymbol{\mu} \rangle}{dt} = \gamma \langle \boldsymbol{\mu} \rangle \times \mathbf{B} \quad (2.13)$$

2.2.3 Macroscopic Magnetization

If each in a group of N spins is considered as having an angular moment $\boldsymbol{\mu}$ in a certain sample, this sample has a magnetization \mathbf{M} with

$$\mathbf{M} = N\boldsymbol{\mu} \quad (2.14)$$

If the spins do not interact with one another, it is easy to prove that (2.13) also holds true for the total magnetization \mathbf{M} and therefore

$$\frac{d\mathbf{M}}{dt} = \gamma \mathbf{M} \times \mathbf{B}. \quad (2.15)$$

2.2.4 Rotating frame of reference

A circularly polarized time-dependent magnetic field $\mathbf{B}_1(t)$ can be described by

$$\mathbf{B}_1(t) = \frac{1}{\sqrt{2}} B_1 (\cos(\omega t) \mathbf{e}_x + \sin(\omega t) \mathbf{e}_y) \quad (2.16)$$

\mathbf{e}_x and \mathbf{e}_y are the unity vectors in the x- and y-directions in the laboratory frame of reference. With the static magnetic field lying along the z-direction, the time dependence of the magnetization in the laboratory frame of reference is given by

$$\frac{d\mathbf{M}}{dt} = \gamma \mathbf{M} \times (B_0 \mathbf{e}_z + \mathbf{B}_1(t)). \quad (2.17)$$

For further calculations it is convenient to eliminate the time dependence of the B_1 field by defining a rotating frame of reference x', y', z' which rotates about the z -axis at the Larmor frequency ω_0 . In such a frame of reference B_1 will be static (Fig. 2.2). Since the axis of rotation coincides with the direction of B_0 , B_0 will also remain static.

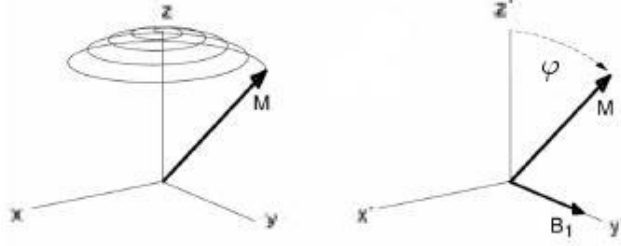


Figure 2.2: Motion of the magnetization vector M in the laboratory frame of reference (left) and the rotating frame of reference (right)

By definition the x -axis in the rotating frame may be along B_1 . Then (2.17) becomes

$$\frac{d\mathbf{M}}{dt} = \gamma \mathbf{M} \times \left[\left(B_0 - \frac{\omega}{\gamma} \right) \mathbf{e}_{z'} + B_1 \mathbf{e}_{x'} \right] = \gamma \mathbf{M} \times \mathbf{B}_{eff} \quad (2.18)$$

This equation states that in the rotating frame of reference, the magnetization acts as though it experiences an effectively static magnetic field \mathbf{B}_{eff} . The magnetization therefore precesses in a cone of fixed angle about the direction of \mathbf{B}_{eff} (Fig. 2.3) at angular frequency

$$\omega_{eff} = \gamma B_{eff} \quad (2.19)$$

The angle between \mathbf{B}_{eff} and B_0 can easily be calculated by trigonometry:

$$\tan \theta = \frac{B_1}{B_0 - \frac{\omega}{\gamma}} = \frac{\omega_1}{\omega_0 - \omega}. \quad (2.20)$$

Since the alternating B_1 is much weaker than the static B_0 field, ω must be near the Larmor frequency ω_0 to detect a difference. If

$$\omega_0 - \omega = \omega_0 - \gamma B_0 = 0 \implies \theta = 90^\circ \quad (2.21)$$

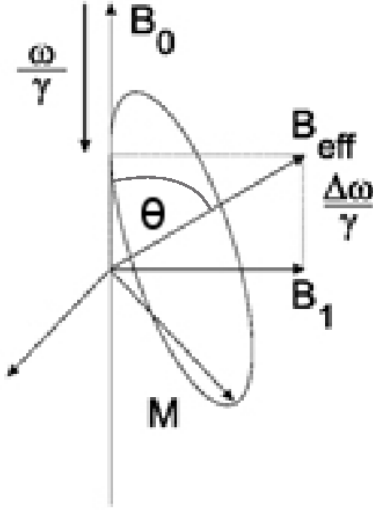


Figure 2.3: Motion of the magnetization M around the effective field B_{eff} [Slichter, 1992]

we have the resonance condition and the effective field will lie completely along B_1 without a component in the z -direction.

When applying an alternating magnetic field B_1 at exactly the resonance frequency $\omega = \gamma B_0$ for a certain time τ , the magnetization rotates away from the z -axis by the angle

$$\varphi(r) = \gamma B_1(r) \tau. \quad (2.22)$$

This angle is also called the *flip angle*. The size of the angle can therefore be varied by adjusting either the amplitude of the applied B_1 field or the time τ the B_1 field is applied. If the B_1 field is applied with a varying amplitude, the flip angle can be described by

$$\varphi(r) = \gamma B_1(r) \int_0^\tau f(t) dt. \quad (2.23)$$

where $f(t)$ is the shape of the varying magnetic field, also called the *pulse shape*. Equation (2.22) would therefore correspond to a pulse with a rectangular pulse

shape.

2.2.5 Pulse shape

When a B_1 field at a single frequency ν is applied, the resultant pulse shape is the sine function $y = \sin 2\pi\nu t$ (Fig.2.4):

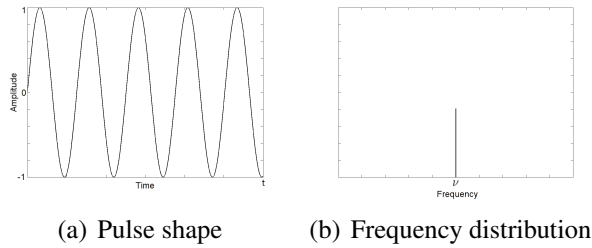


Figure 2.4: A pulse consisting of an infinite sine function at a single frequency excites spins at exactly one frequency

This shows that for the excitation of a single frequency, a continuous wave is necessary. In MRI, the B_1 field is applied in pulses which last a certain time τ , the pulse length. When a constant B_1 field should be applied for a certain time τ , the resultant rectangular pulse consists of a superposition of many different sine functions at various frequencies. The function describing the frequency distribution is called sinc function (Fig.2.5):

$$\text{sinc}(x) = \frac{\sin x}{x} \quad (2.24)$$

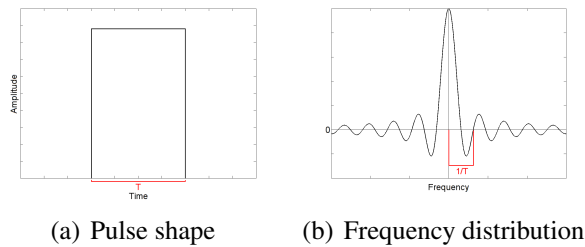


Figure 2.5: A rectangular pulse consists of a superposition of sine functions with varying amplitudes and various different frequencies.

If not the pulse should be rectangular but a rectangular frequency distribution is desired, the resultant pulse has the shape of a sinc function (Fig.2.6).

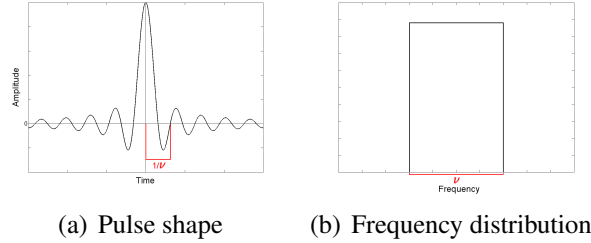


Figure 2.6: A sinc pulse consists of a superposition of sine functions with the same amplitudes but varying frequencies.

The fact that a rectangular frequency distribution is provided by a sinc pulse can be very useful for MRI. When the magnetic field is changing gradually along a certain axis, a sinc pulse with a well defined frequency distribution can be used to excite only a well defined part of the sample (Section 2.3.3).

2.2.6 Transmit field B^+ and receive field B^-

The B_1 mapping methods in section (4.3) usually refer to the measurement of the transmitted power distribution inside an object. In the positively rotating frame of reference (Section 2.2.4) the transmit field, that induces a rotation of the nuclei, would be rotating in the same direction as the net magnetization and is described by:

$$B_1^+ = \frac{\mathcal{B}_{1x} + i\mathcal{B}_{1y}}{2} \quad (2.25)$$

where \mathcal{B}_{1x} and \mathcal{B}_{1y} are complex values describing the field in the laboratory frame of reference. The spins that are excited by the transmit field produce a signal that can be received by the coil (Section 2.2.9). Provided that there is no device changing the phase of the receiving signal it can be shown [Hoult, 2000] that the receiving field precesses in the negatively rotating frame and can be described by:

$$B_1^- = \frac{(\mathcal{B}_{1x} - i\mathcal{B}_{1y})^*}{2} \quad (2.26)$$

For imaging purposes and SAR calculations only the transmit field described by the positively rotating component B_1^+ is necessary. Therefore, equation (2.22) can also be written as

$$\varphi(r) = \gamma B_1^+(r) \int_0^\tau f(t) dt. \quad (2.27)$$

and for a rectangular pulse

$$\varphi(r) = \gamma B_1^+(r) \tau. \quad (2.28)$$

In section (4.3), one B_1 mapping method¹ will be described which provides information about the receive field B_1^- .

2.2.7 Magnetic field strength \mathbf{H} and magnetic field \mathbf{B}

The simulations in chapter 6 always deliver the magnitude of the H_1^+ field. Therefore also many of the experiments, especially in the comparison chapter (6) show the magnitude of the H_1^+ field in A/m instead of the B_1^+ in T.

Since the examined materials are isotropic and linear, i.e. the magnetization is proportional to H , there is a simple relation between \mathbf{B} and \mathbf{H} :

$$\mathbf{B} = \mu_r \mu_0 \mathbf{H} \quad (2.29)$$

μ_r is the relative permeability of the material and for the water based phantoms assumed to be $\mu_r = 1$. μ_0 is the so called magnetic constant and $\mu_0 = 1,256 \cdot 10^{-6} \text{ N/A}^2$.

¹Multi angle approach - section 4.3.5

2.2.8 Relaxation Process and Bloch-equations

After turning off the B_1 field, the magnetization has moved away from its equilibrium position M_0 . The magnetization M is now precessing around the direction of the static magnetic field, the z-direction in this example. Under the influence of thermal perturbations and interactions between the spin and the surrounding system, the system transfers spin energy of the nuclei into kinetic energy of the atoms. The z-component of the magnetization M_z will return to its equilibrium position M_0 after a certain time, also called the *longitudinal* relaxation time [Bloch, 1946].

The rate of change of M_z can be described by

$$\frac{dM_z}{dt} = -\frac{M_z - M_0}{T_1} \quad (2.30)$$

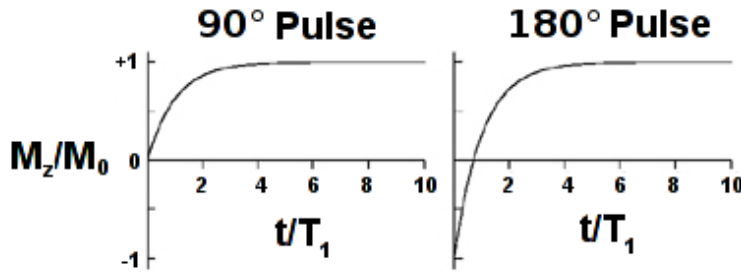


Figure 2.7: Recovery of the magnetization after a microwave pulse [Bruker, www.bruker-biospin.com]

The behaviour of the longitudinal relaxation after a 90° and a 180° pulse can be seen in Fig. (2.7). After the magnetization has been flipped into the xy-plane by a $\frac{\pi}{2}$ pulse, it relaxes back until it again reaches the equilibrium magnetization M_0 . After a 180° pulse, which flips the magnetization into the opposite direction of M_0 , the magnetization relaxes first into the xy-plane where the longitudinal magnetization vector reaches zero and then returns to the position of the equilibrium magnetization.

Another process which does not change the total energy of the spin system, but only affects the components of the polarization which are transverse to the field

is called *transversal* relaxation. This relaxation process appears due to interactions between neighbouring spins and the resulting small field inhomogeneities resulting in different precession frequencies of the spins. During this process, the transverse magnetization in x- and y-direction decreases to zero as described by the equations

$$\frac{dM_x}{dt} = -\frac{M_x}{T_2} \quad (2.31)$$

$$\frac{dM_y}{dt} = -\frac{M_y}{T_2} \quad (2.32)$$

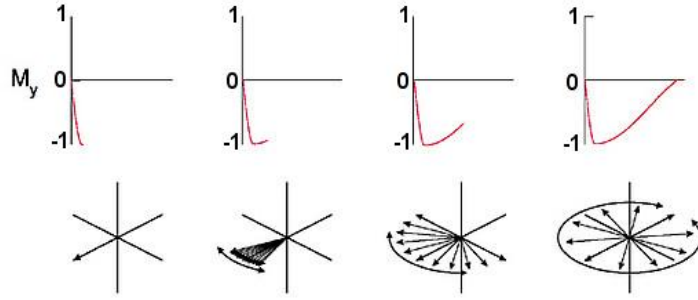


Figure 2.8: Upper row: Decay of the transverse magnetization with time; Lower row: Dephasing of the spins in the xy-plane [Bruker, www.bruker-biospin.com]

In Fig. (2.8) it is shown how all the magnetic moments are in phase right after the pulse and start dephasing after a short time resulting in an overall zero magnetization in the xy-plane.

The total rate of change of \mathbf{M} is obtained by adding to the expression (2.15), which takes into account the action of external fields only, the changes (2.30), (2.31) and (2.32) of its components due to internal actions. The following differential equations for the three components of \mathbf{M} can then be obtained:

$$\frac{dM_x}{dt} - \gamma(M_y B_z - M_z B_y) + \frac{M_x}{T_2} = 0 \quad (2.33)$$

$$\frac{dM_y}{dt} - \gamma(M_z B_x - M_x B_z) + \frac{M_y}{T_2} = 0 \quad (2.34)$$

$$\frac{dM_z}{dt} - \gamma(M_x B_y - M_y B_x) + \frac{M_z}{T_1} = \frac{M_0}{T_1} \quad (2.35)$$

These equations are called the Bloch-equations after Felix Bloch, who first used them in 1946 to describe the relaxation processes.

2.2.9 Free induction decay

In the most simple NMR experiment, the decay of the NMR signal after turning off the previously applied B_1 field is observed. As previously described, with only the static B_0 field remaining, the spins start dephasing and the transverse magnetization in the xy-plane therefore begins to decay. The magnetization in the x- and y-directions is given by solving the Bloch-equations and for a 90° pulse delivers the result for the magnetization

$$M_{xy}(t) = M_0(1 - e^{-\frac{TR}{T_1}})e^{-TE/T_2} \quad (2.36)$$

with $M_{xy}(t) = M_x(t) + iM_y(t)$. When a 90° pulse was applied, at $t = 0$ the magnetization is completely rotated into the transversal xy-plane and $M_{xy}(0) = M_0$. Right after that, the magnetic moments start to dephase which results in an exponential decay of the signal (see Fig. 2.9). The detection of the NMR signal is done with a RF coil, which is positioned perpendicular to the x,y plane. In this way, the rotating magnetization vector induces an alternating current in the coil.

2.2.10 Hahn Echo

Another component that can lead to transversal relaxation are small inhomogeneities of the static B_0 field. The resultant relaxation time T_2^* is a combination

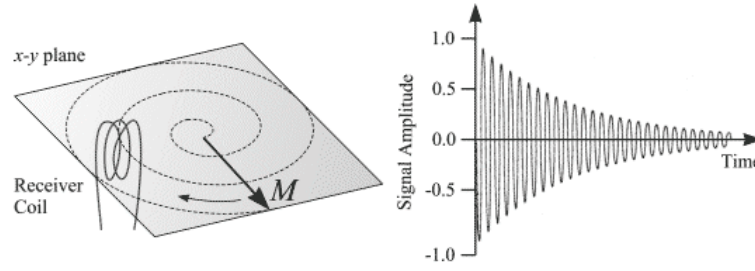


Figure 2.9: The exponential decay of the signal over time [Easy Measure, www.easymeasure.co.uk]

of relaxation effects due to spin-spin interactions as described before and those inhomogeneities of the static magnetic field represented by $T_{inhom.}$:

$$\frac{1}{T_2^*} = \frac{1}{T_2} + \frac{1}{T_{inhomog.}} \quad (2.37)$$

This consequently leads to a faster decay of the transversal magnetization. Erwin Hahn discovered in 1950 [Hahn, 1950] that another π pulse, applied a certain time τ after the first $\frac{\pi}{2}$ pulse, refocused the spins that ran out of phase due to the field inhomogeneities (Fig. (2.10)).

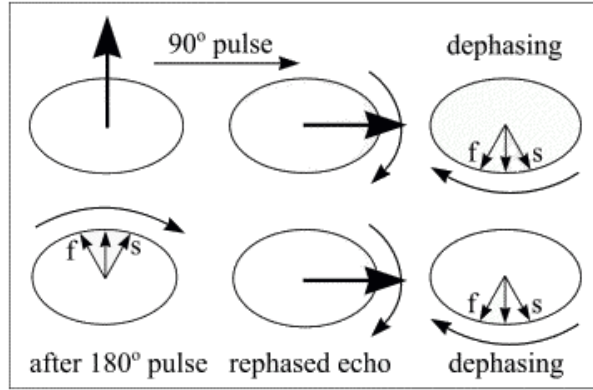


Figure 2.10: Dephasing of the magnetisation vector by T_2^* and rephasing by a $\frac{\pi}{2}$ pulse to form a spin echo. [Easy Measure, www.easymeasure.co.uk]

After time 2τ , an echo can be observed with exactly the same form but with a smaller amplitude than the normal FID signal. This decrease in the amplitude results from the decrease in the transversal magnetization and is also called T_2

decay(Fig. 2.11). It is also possible to repeat the π pulse several times after waiting a 2π period before each pulse. This will produce additional echoes, but with decreasing amplitude of each additional echo (Fig. 2.11).

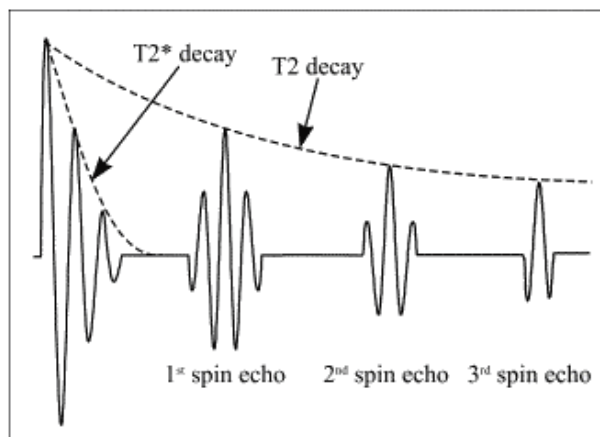


Figure 2.11: Decay of signal with time in a spin echo sequence [*Easy Measure*, www.easymeasure.co.uk]

2.2.11 Chemical shift

Upon inserting an atom into a magnetic field, the electrons start rotating about the direction of the applied magnetic field causing a small magnetic field which opposes the externally applied field (Fig. 2.12).

The nucleus is therefore shielded a small amount from the externally applied field and experiences a magnetic field B_s which is a fraction s smaller than the applied field B_0 .

$$B_s = B_0(1 - s) \quad (2.38)$$

Inside a molecule, the electron density around each nucleus differs according to the neighbouring nuclei and the bonds in the molecule. The opposing field and therefore the actually experienced magnetic field for each nucleus varies by a



Figure 2.12: Shielding of the magnetic field

small amount. This variation caused by a change in the environment of nucleus is called *chemical shift*. The chemical shift is usually defined in a frequency independent form, so that it can be applied for scanners working at different field strengths, by

$$d = \frac{(\nu - \nu_{ref}) \cdot 10^6}{\nu_{ref}}. \quad (2.39)$$

The units of d are *ppm*. In the literature, the chemical shift d is usually given relative to the standard substance tetramethylsilane (TMS).

Examples:

1. The hydrogen atoms in a sample of pure deionized water all experience the same applied magnetic field. Just one resonance frequency for all the hydrogen atoms exists (Fig. 2.13).
2. In a sugar-water mixture (Sugarphantom, Table 3.3), a gap of about 500 Hz between the resonance frequency of water and the resonance frequencies of the different hydrogen atoms of the sucrose molecule can be observed (Fig. 2.14). The chemical shift between these two types of nuclei is about $1,7 \text{ ppm}$.
3. Fat and water: Between fat and water there is a chemical shift of about

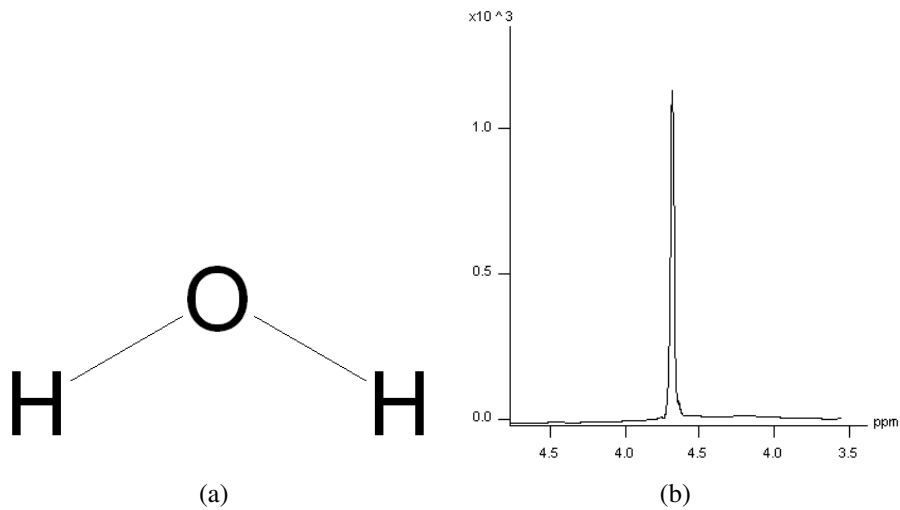


Figure 2.13: a) The structure of water b) The resonance frequency of water

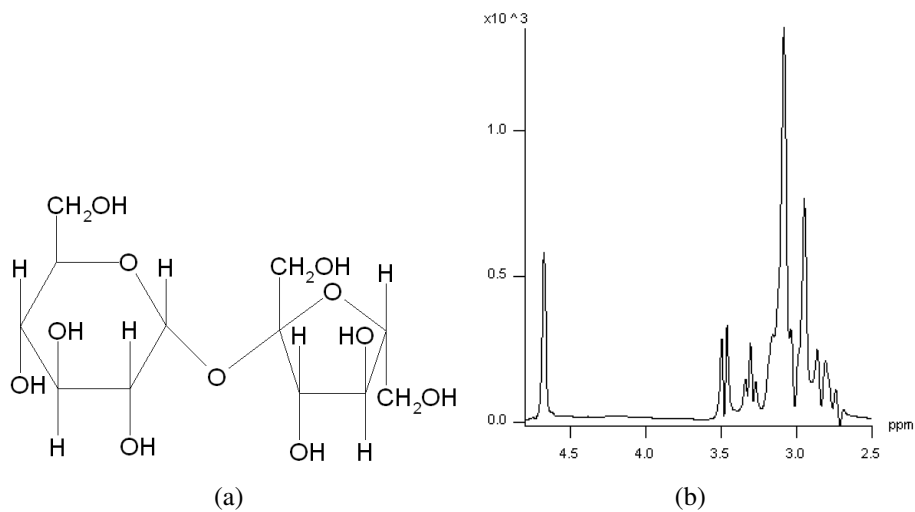


Figure 2.14: a) The structure of sucrose b) The spectrum of the Sugarphantom (Table 3.3). The peak on the left at 4,7 ppm belongs to the water while the bulk of peaks around 3 ppm on the right belongs to the sucrose. In the structure formula many different hydrogen atoms with different neighbours can be seen. This is represented by the spread into different peaks on the right³.

3, 5 *ppm*. At 300 MHz the resonance frequencies between fat and water therefore differ by 1040 Hz. This is an important fact that has to be considered later in this work (6.3.1).

2.3 Image formation in MRI

The values of T_1 and T_2 depend very much on the specific substance and its environment. For example, some parts in the brain such as the blood vessels have a higher water content than others and therefore have different relaxation times. In Magnetic Resonance Imaging this effect is used to image areas with different physiological properties. In this work the so called Gradient Echo Sequence is primarily used and will be described in this section.

2.3.1 Gradient Echo (GRE)

To acquire an image using magnetic resonance, we need some sort of spatial encoding of the spins at different locations. In order to encode the spatial characteristics of a sample, a controlled variation in the effective magnetic field can be created by applying a gradient magnetic field that perturbs the static magnetic field B_0 by an amount ΔB given by

$$\Delta B = \mathbf{G} \cdot \mathbf{r} \quad (2.40)$$

Here \mathbf{r} is the spatial coordinate of the spin in the resting reference frame and \mathbf{G} is the component of the gradient field. A simple magnetic gradient along the static magnetic field, in this case the z-direction, can be produced by a so called Maxwell coil (Fig. 2.15), where two coils are aligned along the axis and a current is running clockwise in the first and counterclockwise in the second coil. The first coil is increasing the magnetic field while the other one is decreasing it, therefore producing a varying magnetic field between the coils.

Gradient coils along the x and y axes have a more complicated saddle-like shape because a variation can always just take effect along the static B_0 field, whereas the gradient has in this case to be along the x or y direction.

With spatial encoding the Larmor frequency of the rotating spins depends on the corresponding local field the spins experience at their position and is given by

$$\omega_0(\mathbf{r}) = \gamma(B_0 + \mathbf{r} \cdot \mathbf{G}) = \gamma(B_0 + xG_x + yG_y + zG_z) \quad (2.41)$$

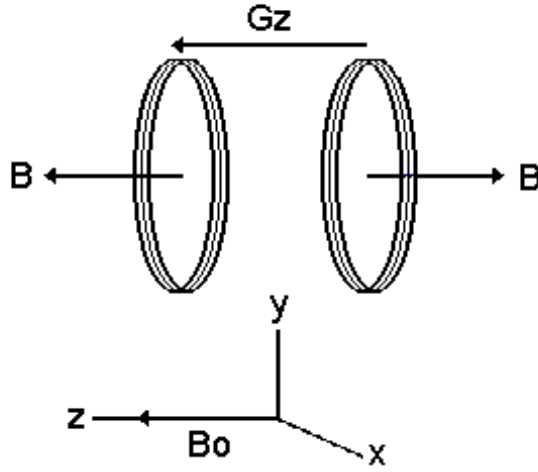


Figure 2.15: Schematic composition of a Maxwell coil [Hornak, <http://www.cis.rit.edu/htbooks/mri/>]

G_x , G_y and G_z are the gradients along the x,y and z-direction in the laboratory frame of reference. When a gradient G_1 is applied for a certain time t_1 along for example the x-axis, the spins with a negative x-coordinate will experience a lower field and precess slower than the spins with a positive x-coordinate. With a variation along the x-axis, the precessing spins will lose coherence and rotate out of phase resulting in a phase dispersion

$$\phi(\mathbf{r}, t_1) = \gamma \int_0^{t_1} \mathbf{r} \cdot \mathbf{G}_1(t') dt' \quad (2.42)$$

Neglecting other effects which cause the spins to dephase, it is possible to rephase the spins by applying another gradient G_2 for the time t_2 in the opposite direction of the first gradient. Then the spins with a negative x-coordinate precess faster than the ones with a positive x-coordinate and under the condition

$$\phi(\mathbf{r}, t_1) + \phi(\mathbf{r}, t_2) = \gamma \int_0^{t_1} \mathbf{r} \cdot \mathbf{G}_1(t') dt' + \gamma \int_0^{t_2} \mathbf{r} \cdot \mathbf{G}_2(t') dt' = 0 \quad (2.43)$$

the spins are rephased again. Notice the difference to the the Hahn Echo, where a similar effect was achieved by applying a $\frac{\pi}{2}$ and a π pulse. In the case of the gradient echo just the dephasing that was caused by the gradient is rephased again. In

the case of the Spin echo, the natural dephasing due to T_2^* relaxation is rephased again. Fig.(2.16) is a graphical representation of the timing of a basic GRE imaging sequence. The following sections give a description of the different lines presented in the timing diagram.

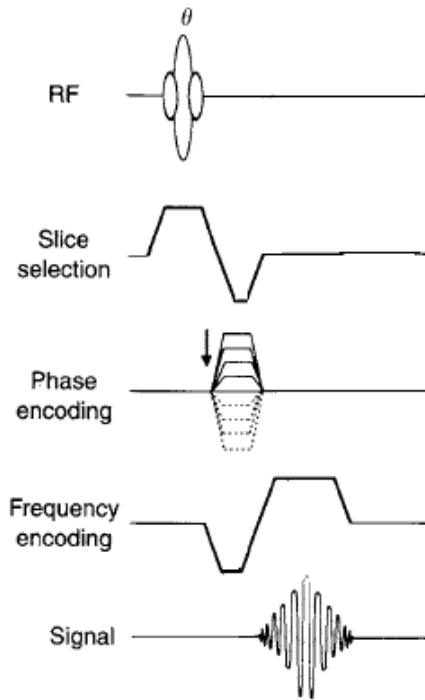


Figure 2.16: Timing diagram for a gradient echo (GRE) sequence [Bernstein et al., 2004]. The explanation of the different lines are given in sections (2.3.2) to (2.3.6).

2.3.2 RF

The first line shows the excitation pulse. It is also possible in a GRE sequence that the excitation pulse is less than 90° (Fig. 2.17). This allows a faster acquisition time, because the spins return faster to their equilibrium position M_0 , allowing shorter time periods between several excitation pulses. The drawback is a loss in signal since the transverse part M_{xy} does not reach its maximum value.

2.3.3 Slice selection

During the RF pulse a gradient along the z-axis is applied. At a static field strength of 7 T the RF pulse must have a frequency of $\omega_0 = 297,2 \text{ s}^{-1}$. With

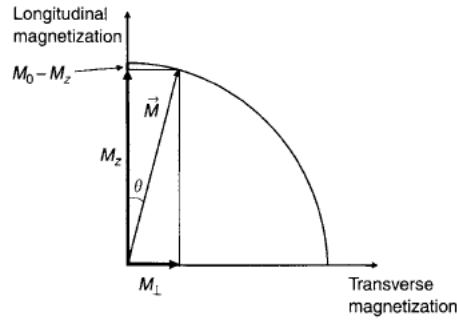


Figure 2.17: Amount of transverse magnetization M_{\perp} created by a RF pulse less than 90° [Bernstein et al., 2004]

the gradient along the z-direction, only spins at a particular z-position experience a field strength of 7 T. The other spins experience either a higher or a lower static magnetic field. Those which experience another field strength cannot be excited according to equation (2.7) and will not start to precess around the z-axis. Therefore, this gradient selects a particular transversal slice which will be excited.

In Section 2.2.5 the relation between the pulse shape and the frequency distribution provided by the pulse was given. If a slice selective gradient is applied during the pulse, this frequency distribution exactly resembles the slice profile that will be excited. Because a sinc pulse excites a rectangular slice it is also called *selective pulse*. The rectangular pulse on the other hand has a very bad slice selectivity. A rectangular pulse excites a slice with a sinc shape, resulting in different parts of the slice experiencing a different B_1^+ field.

Directly after the slice selective gradient a rephasing gradient is applied to ensure that all the spins within the slice possess the same phase.

2.3.4 Phase encoding

Right after the transversal slice has been selected, the spins in this slice all precess at the same Larmor frequency and are all in phase. Now let's presume a phase encoding gradient G_x is enabled along the x-direction. Then all the spins along the x-axis experience a varying static magnetic field B_0 . With the variation of the field ΔB given by equation (2.40) the new precession frequency ω changes

according to the equation

$$\omega = \gamma(B_0 + xG_x) = \omega_0 + \gamma xG_x. \quad (2.44)$$

While the phase encoding gradient is on, each transverse magnetization vector has its own unique Larmor frequency. But after turning off the phase encoding gradient, again all the transverse vectors again experience the same static magnetic field B_0 . They all continue to precess at the same frequency but out of phase, the phase depending on the time and the magnitude of the applied gradient. Since during an NMR experiment the total signal of all the different spins is detected, the spins with a different phase sum up to one resultant transverse magnetization and make it impossible to directly determine the spatial position of the spin (in our case the x-position) after applying one phase encoding gradient. For this reason the phase encoding gradient is applied N times, with a variation of the strength in equidistant steps from $-G_x$ to $+G_x$. The number N corresponds to the resolution of the final image.

2.3.5 Frequency encoding

The frequency encoding gradient consists of two parts, first the de-phasing gradient and after that the readout gradient. During the de-phasing gradient a gradient field is applied perpendicular to the phase encoding gradient, in this case in the y-direction. The dephasing gradient works similarly to that described in the previous section. The spins along the y-direction start to precess at different frequencies, providing this way a spatial encoding along the y-direction. But at the same time the spins start to dephase and lose coherence. This works as a preparation of the transversal magnetization for an echo signal during the readout gradient. As described in section (2.3.1) it is possible to create an echo by applying a gradient in the opposite direction. In the middle of the rephasing gradient the spins in y-direction all have the same phase and the echo is a maximum.

The overall signal from the net magnetization vector results from spins precessing at a different frequency (along y) and with a different phase (along x). A

2D Fourier Transformation of the echo signal splits the overall signal into the different frequency-phase pairs and, according to the amplitude of each pair, can determine the spin density at position x,y .

2.3.6 Signal

In the GRE sequence the signal consists of an echo that is prepared by the dephasing component of the frequency encoding gradient and which reaches its maximum during the middle of the readout component of the frequency encoding gradient.

Chapter 3

Phantoms

3.1 Overview

In MRI, phantoms play an important role in the calibration and checking of MRI equipment. The construction of such MRI phantoms will be explained in this chapter. In the first part various materials used for phantom construction are introduced. Ingredients for modifying the electromagnetic properties and relaxation times are presented and the advantages and disadvantages of aqueous and gel phantoms are explained. Many different gelling agents with their characteristics are tested and the one best suitable for the construction of head phantoms is chosen. After the introduction of the different materials, there will be a manual for the construction of a realistic head phantom.

Realistic phantoms concerning the anatomy (e.g.[Shmueli, Thomas, & Ordidge, 2007]) and the dielectric properties (e.g.[Yang et al., 2004]) already exist but a realistic phantom concerning both anatomy and dielectric properties is missing so far. In the last part of this chapter the measurement device for measuring the electromagnetic properties of the phantoms will be explained.

3.2 Materials

Various materials are used for phantom construction, depending on the purpose of the phantom. Important characteristics for MRI phantoms can be seen in the following list. The characteristics that are important for this thesis, B_1^+ mapping experiments to examine the behaviour of RF radiation in the human head, are printed in bold letters.

1. **electric properties equivalent to human tissues**
2. relaxation times equivalent to human tissue
3. **homogeneous relaxation times and dielectric properties throughout the phantom**
4. **sufficient strength to fabricate a torso without the use of physical reinforcement**
5. **ability to fabricate the shape of a human organ**
6. **ease of handling**
7. **chemical and physical stability over extended time periods**

Among the phantoms you can differentiate mainly between two types, the aqueous and the gel phantoms. The advantage of aqueous phantoms are the homogeneity throughout the phantom and the long-term stability. Several ingredients which can change the properties of the phantom to the desired values can be seen in table (3.1). The influence of the conductivity and the permittivity on the electromagnetic field distribution in a sample is explained in section 4.2.

3.2.1 T_1 estimation

In this work no effort was taken to simulate the relaxation times of body tissue. There exist several recipes for phantoms with realistic relaxation times ([Yoshimura et al., 2003],[Kato et al., 2005]). However, since relaxation times do

Ingredient	Purpose	+	-
Copper(II) sulfate pentahydrate ($CuSO_4 \cdot 5H_2O$)	T_1 modifier	<ul style="list-style-type: none"> • ease of handling, because of need of bigger doses 	<ul style="list-style-type: none"> • harmful • dangerous for the environment → disposal complicated
Manganese(II) Chloride tetrahydrate ($MnCl_2 \cdot 4H_2O$)	T_1 modifier	<ul style="list-style-type: none"> • ease of handling 	<ul style="list-style-type: none"> • harmful
Gadolinium(III) Chloride hexahydrate ($GdCl_3 \cdot 6H_2O$)	T_1 modifier	<ul style="list-style-type: none"> • high susceptibility 	<ul style="list-style-type: none"> • difficult to handle, because of need of very small doses • harmful
Nickel(II) sulfate hexahydrate ($NiSO_4 \cdot 6H_2O$)	T_1 modifier	<ul style="list-style-type: none"> • ease of handling 	<ul style="list-style-type: none"> • harmful • dangerous for the environment → disposal complicated
Sodium Chloride ($NaCl$)	conductivity modifier	<ul style="list-style-type: none"> • ease of handling • harmless 	<ul style="list-style-type: none"> • also influences relaxation times
Sucrose (<i>Saccharose</i>)	permittivity modifier	<ul style="list-style-type: none"> • ease of handling • harmless 	<ul style="list-style-type: none"> • sticky • needs large amounts
Polyethylene powder	permittivity modifier	<ul style="list-style-type: none"> • ease of handling 	<ul style="list-style-type: none"> • does not dissolve in water but just mixes into gels

Table 3.1: Different ingredients and their properties

not influence the distribution of the electromagnetic field inside the object, this area was not investigated. There are two other points which make a modification of the relaxation time useful.

1. With a shorter T_1 time, it is possible to use a shorter TR ¹ time when acquiring B_1^+ maps with certain B_1^+ mapping methods (Section 4.3). The scanning times therefore become much shorter. (4.3.2)
2. For phantoms which simulate different tissues, the segmentation process is easier, if there is a contrast between different materials. Different T_1 relaxation times for the different parts lead to a contrast in a T_1 weighted sequence like an inversion recovery sequence.

In an inversion recovery sequence an inversion pulse flips the longitudinal magnetization from the direction parallel to the stationary magnetic field to the direction antiparallel to the field (e.g. from +z to -z). From their new state the spins start relaxing for a certain time TI (Fig. 2.7, recovery after a 180° pulse), the inversion time. After TI has passed an excitation pulse is applied. At that time spins with a short T_1 are already almost completely relaxed. Spins with a long T_1 still might be almost not recovered. This pulse now converts the differences of the longitudinal magnetization into differences of the transversal magnetization, therefore producing a T_1 contrast among tissues with different longitudinal relaxation times. The signal intensity of an inversion recovery sequence is given by:

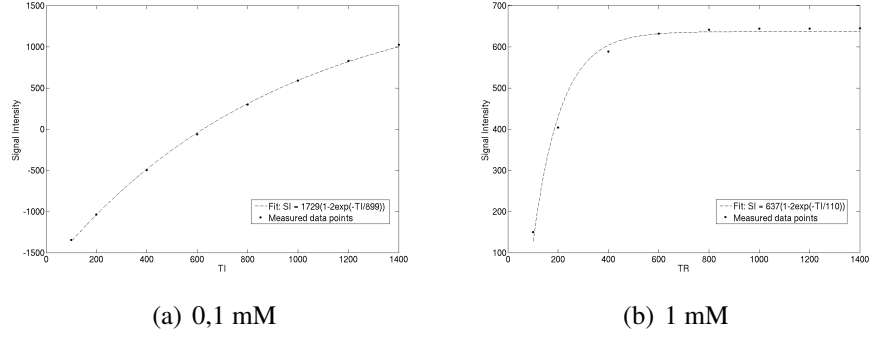
$$SI = M_0(1 - 2e^{-TI/T_1}). \quad (3.1)$$

It can be seen that if TI is chosen to be long enough, the exponential term vanishes and only the equilibrium magnetization M_0 remains.

Experiment: 3 solutions of $MnCl_2$ with concentrations 0.1 mM, 0.25 mM and 1 mM were prepared. An inversion recovery sequence with 90° excitation pulse, $TR = 10\text{ s}$, $TE = 7,8\text{ ms}^2$ was run for 8 different inversion times TI between $TI = 100\text{ ms}$ and $TI = 1400\text{ ms}$. The signal intensities SI for each phantom were fitted with MatLab to equation (3.1). The fitted curves can be seen in

¹Repetition time (Section 5.2)

²Echo time (Section 5.2)

Fig.(3.1)³.Figure 3.1: The signal intensities of sample 1 and 3 versus the inversion time TI .

The MatLab fit delivered the T_1 times shown in table 3.2.

0,1 mM $MnCl_2$ solution	$T_1 = 899ms$
0,25 mM $MnCl_2$ solution	$T_1 = 418ms$
1 mM $MnCl_2$ solution	$T_1 = 110ms$

Table 3.2: T_1 times for different concentrated $MnCl_2$ solutions

3.2.2 Examples of aqueous phantoms used in these studies

Table (3.3) shows a list of different aqueous phantoms that were used throughout this study.

³The scanner just delivers positive signal intensities. The negative signal intensities for sample 17 are achieved by manually multiplying -1 to each signal intensity before the *signal null* image. This method must be used sometimes when applying a fit, e.g. for the B_1^+ mapping method by Dowell and Tofts (Section 4.3.7)

Name	Ingredients	Characteristics
Orange Phantom Siemens 1018 5355 K2285	<ul style="list-style-type: none"> • 1 g <i>Tris</i> • 0,2 g <i>fat – orange</i> per 1 kg <i>dimethylpolysiloxaneoil</i>	$\varepsilon = 3,2$ $\sigma = 0,003 S/m$
Siemens phantom Siemens 5512 608 K2205	<ul style="list-style-type: none"> • 1,24 g $NiSO_4 \cdot 6H_2O$ • 2,62 g <i>NaCl</i> per 1 liter H_2O	$\varepsilon = 78$ $\sigma = 0,52 S/m$
Manganphantom	<ul style="list-style-type: none"> • 0,026 g $MnCl_2 \cdot 4H_2O$ • 5,18 g <i>NaCl</i> per 1 liter H_2O	$T_1 = 850 ms$ $\varepsilon = 80$ $\sigma = 0,87 S/m$
Sugarphantom	<ul style="list-style-type: none"> • 1230 g <i>sugar</i> • 0,5 g NaN_3 • 53,74 g <i>NaCl</i> per 1 liter H_2O	$T_1 = 250 ms$ $\varepsilon = 54$ $\sigma = 0,63 S/m$
Phantom091	<ul style="list-style-type: none"> • 0,026 g $MnCl_2 \cdot 4H_2O$ • 5,41 g <i>NaCl</i> per 1 liter H_2O	$\varepsilon = 80$ $\sigma = 0,91 S/m$
Phantom046	<ul style="list-style-type: none"> • 0,026 g $MnCl_2 \cdot 4H_2O$ • 2,60 g <i>NaCl</i> per 1 liter H_2O	$\varepsilon = 80$ $\sigma = 0,46 S/m$
Sunflower Oil	sunflower oil	$\varepsilon = 3,1$ $\sigma = 0,02 S/m$

Table 3.3: Different kinds of aqueous phantoms

3.2.3 Usage and properties of different gelling agents

The disadvantage of aqueous phantoms is that they need a container to remain in the desired shape, which makes it hard to mimic phantoms in the shape of human organs.

Additionally, using gels make it possible to construct a phantom in a realistic shape with various materials of different electromagnetic properties simulating the different body tissues.

Types of gelling agents

Jelly-like phantoms are constructed by the use of various gelling agents. The following gelling agents have been used in different works so far (e.g. [Onishi, 2005][Mazzara, Briggs, Wu, & Steinbach, 1996][Mano, Goshima, Nambu, & Iio, 1986][Chou, Chen, Guy, & Luk, 1984]). More information in the certain types is given in the next section and in the productlist (Table .2).

- agarose
- agar
- hydroxyethylcellulose (HEC)
- gelatin
- TX-151
- polyacrylamide
- carrageenan
- polyvinyl alcohol (PVA)

Agarose and agar agar

Agar is a heterogeneous mixture of two classes of polysaccharide: agaropectin and agarose. Since agaropectin is heavily modified with acidic side-groups, such

as sulfate and pyruvate, agarose is significantly purer than agar agar. This also makes agarose much more expensive⁴ and therefore not very practical when large quantities are needed for the construction of life-sized phantoms. Agar agar on the other hand is very cheap⁵ and experiments showed that it does not influence the conductivity or permittivity of the substance (Section 3.2.4).

In these phantoms the T_2 times depend strongly on the concentration of the gelling agent and therefore also on the physical strength of the phantom. For this reason the phantom should not be made too rigid, because this would lead to very short T_2 times, making it difficult to receive enough signal from the phantom.

- + : Can be easily dissolved in cold water, cheap, ease of handling
- : Starts molding, for different compartments intervening septa needed

Preparation: The agar agar powder can be easily dissolved in cold water and the solidification will start upon cooling once it has been heated to over 85° . It is recommended to dissolve all the parameter modifiers like NaCl etc. before. Then the agar agar should be inserted and heated. At high temperatures care has to be taken to avoid the incorporation of air bubbles. The amount of agar agar used directly influences the solidity of the gel.

Carrageenan

Carrageenans are also a family of polysaccharides extracted from seaweeds. There are three different kinds of carrageenans:

- κ - carrageenan: Forms strong and rigid gels when mixed with water. Best suitable for building rigid gel phantoms
- ι - carrageenan: Forms soft pudding-like gels when mixed with water. It is therefore not able to support a rigid phantom
- λ - carrageenan: Forms gels when mixed with proteins. Mainly used for dairy products and not suitable for constructing phantoms.

⁴50g \sim 100EUR(CarlRoth)

⁵25g \sim 2EUR(Asiamarket)

κ - carrageenan is the only one suitable for the desired purpose.

- + : Compared to agar agar minor influence on T_2 , cheap
- : Water turns into gel even at room temperature, therefore hard to mix especially for high concentration

Preparation: Before inserting the gelling agent all the other reagents like T_1 modifiers or NaCl should be dissolved in the water. When mixing in the carrageenan the mixing should occur slowly enough to avoid air bubbles but also fast enough to dissolve the whole powder before solidification of the gel. A small drop of washing detergent helps lowering the surface tension of water and prevents the carrageenan from accumulating at the water surface.

Hydroxyethylcellulose (Natrosol 250 Pharm HEC HX)

HEC, also called Natrosol, is a nonionic water-soluble polymerizing agent [Hartsgrove & Surowiec, 1987]. It is available in a wide range of viscosities. Since a rigid gel was desired, Natrosol 250 Pharm HEC HX was chosen, which has one of the highest viscosity values of the different Natrosol gelling agents.

- + : Durability
- : Water turns into gel even at room temperature and is therefore hard to mix especially at high concentration.

Preparation: Before inserting the gelling agent all the other reagents like T_1 modifiers or NaCl should be dissolved in the water. When mixing in the HEC the mixing should occur slowly enough to avoid air bubbles but also fast enough to dissolve the whole powder before solidification of the gel. For the concentrations where mixing to dissolve all the gelling agent was still possible, the gel never became rigid enough to support its own shape. For higher concentrations of HEC it was not possible to dissolve the whole gelling agent because either the stirring was too slow and the gel solidified too fast or the stirring was so fast that many air bubbles were generated within the gel.

TX-151

TX-151 is a polysaccharide material with some ingredients like e.g. a preservative agent. It solidifies already in cold water, which again makes the preparation difficult.

- + : more durable than agarose gels
- : solidifies in cold water; making mixing problematic because fast mixing causes unwanted air bubbles within the gel

Preparation: First all the modifiers like NaCl etc. should be dissolved in water. Because the gelling time increases with a decrease of water temperature, it is recommended to cool the water, the bowl and all the mixing ingredients before the insertion of TX-151. In addition the gelling time increases when the amount of TX-151 decreases. When inserting the TX-151, the mixing should happen at a slow speed to avoid the incorporation of air bubbles. On the other hand it must be fast enough to be able to completely mix the components.

A phantom was constructed using a TX-151 according to the recipe of Ito [Ito, 2001]. Polyethylene was used to modify the permittivity of the phantom. The electromagnetic parameters matched exactly with the desired values and the handling of the phantom was good. But unfortunately the phantom, which is usually used for temperature measurements with an infrared camera, contained many air bubbles and delivered not enough signal in the scanner.

Polyacrylamide

Polyacrylamide is a polymer formed from acrylamide subunits. Because some unpolymerized acrylamide, which is a neurotoxin, can always be present even in the usually nontoxic polyacrylamid gel, it has to be treated with great caution. Furthermore, the preparation is significantly more tedious than with agarose gels. Because oxygen inhibits the polymerization process, they must be poured between glass plates. This is not very practical for phantom construction, because the quantities used there are usually quite big ($> 2\text{ l}$).

- +: durable
- : poisonous, preparation difficult

3.2.4 Influence of the gelling agent on the B_1^+ distribution within phantom

An experiment was performed to ensure that using a gelling agent for the phantom solidification does not influence the B_1^+ distribution within the phantom.

Experiment: Two phantoms were prepared with the ingredients shown in table 3.4.

Type	Ingredients	Characteristics
Water	3,75 g <i>NaCl</i> per 1 liter H_2O	$\varepsilon = 80, \sigma = 0,64 S/m$
Gel	20 g <i>agar agar</i> + 3,75 g <i>NaCl</i> per 1 liter H_2O	$\varepsilon = 80, \sigma = 0,64 S/m$

Table 3.4: Ingredients of the gel and the water phantom

The ingredients were mixed thoroughly and the gel was solidified by heating the mixture up to $95^\circ C$. The water mixture and the still hot and liquid gel were poured into two 2 l bottles, both having exactly the same shape. After solidification of the gel both phantoms were measured.

Result: The resultant B_1^+ field maps can be seen in Fig. (3.2). It can be clearly seen that the gelling does not influence the distribution of the B_1^+ field.

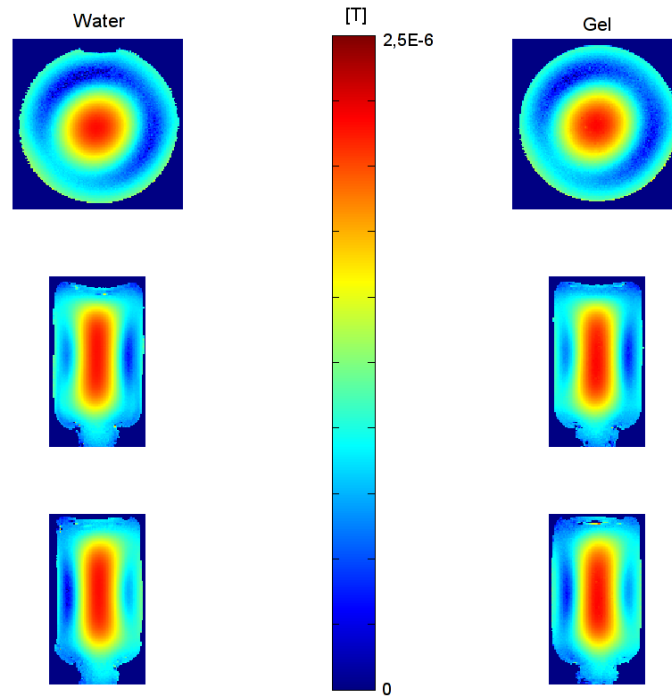


Figure 3.2: Left side: B_1^+ field map of the water phantom, Right side: B_1^+ field map of the gel phantom

3.2.5 Permittivity and conductivity modifiers

Biological tissue has specific dielectric properties dependent on the frequency of the electromagnetic field it is exposed to. The dielectric properties for various tissue types at a wide range of frequencies has already been examined [Gabriel, 1995]. The properties at 300 MHz for the average values of different tissue types can be seen in Table (3.5).

Tissue	Permittivity	Conductivity
Av. Brain	52	0,55 S/m
Av. Skull	18	0,15 S/m
Av. Muscle	59	0,79 S/m

Table 3.5: Dielectric properties of different tissue types

In the following section, the influence of NaCl and sucrose on the conductivity and permittivity respectively of a water sample is examined. In the diagrams the amount of substance g/l is plotted instead of the concentration in mol/l . Since the solvent used was always water, this seemed more practical for the experiments. Furthermore, no error estimation was done for the linear fits. The error for these fits is significantly smaller than the real error, because all of these samples were mixed under exactly the same conditions. Under different conditions, such as for very big samples, varying mixing times etc., the result may differ from the suggested values by more than 5%. For this reason, the electromagnetic parameters of the sample should always be measured before the gelling procedure to ensure the desired values. The error of the measurement of the parameters is estimated in section (3.2.7).

The influence of NaCl on the conductivity

For preparation of phantoms with a certain permittivity and conductivity, knowledge concerning the influence of permittivity and conductivity modifiers is necessary. Firstly, the influence of different quantities of sodium chloride (NaCl) on the conductivity of a sample were investigated. For this purpose, ten samples each with 50 ml deionized water and different quantities of NaCl ranging from 0 g to 14,9 g were prepared. The permittivities and conductivities of every sample were measured⁶. Then the conductivity was plotted versus the amount of NaCl.

The fitting was done with the MatLab fitting toolbox and the following linear relation between conductivity σ and amount m of NaCl in g per $1\ l$ deionized water could be acquired:

$$\sigma = 0,16 \cdot m + 0,04 \quad (3.2)$$

For higher amounts over 300 g NaCl per $1\ l$ this relation is no longer linear. However, since higher conductivities are far away from physiological values, those

⁶The measurement procedure is described in section 3.2.7

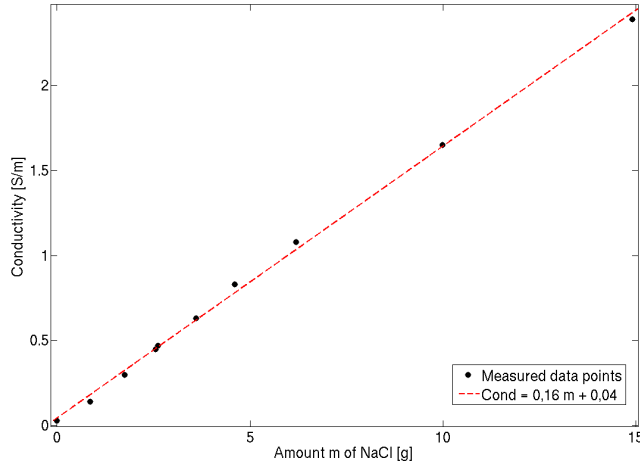


Figure 3.3: The conductivity versus the inserted amount of NaCl per 1 l of deionized water

regions were not of interest for the experiments. The permittivity of all the samples was $\varepsilon = 79$ and was not influenced by the NaCl.

The influence of sugar on the permittivity

In this experiment the influence of sugar on the permittivity of the sample was examined. 8 samples each with 1 l of deionized water and different amounts of sugar between 0 g and 2450 g were prepared. Due to the large quantity of sugar, long and thorough mixing was necessary. The permittivity of every sample was measured and plotted against the amount of sugar inserted.

With the MatLab fitting toolbox the following relation between the amount of sugar m and the permittivity of a 1 l sample of water could be observed:

$$\varepsilon = -0,017 \cdot m + 78 \quad (3.3)$$

It is important to mention that for amounts of sugar with $m > 2000$ g the sample had to be heated to dissolve all the sugar. The conductivity of the sample was also

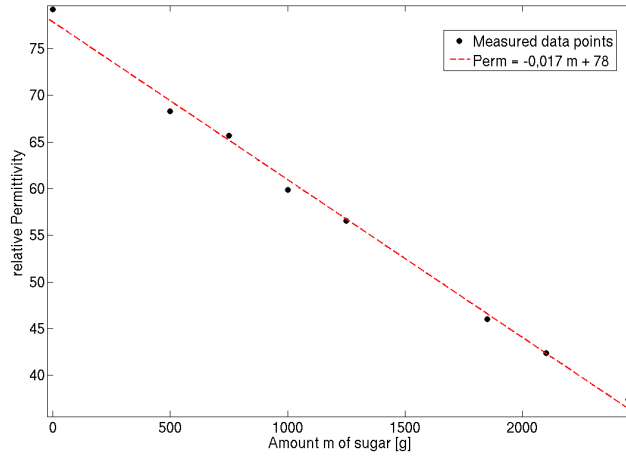


Figure 3.4: The permittivity versus the inserted amount of sugar in g per $1\ l$ of water

influenced by the quantity of sugar present since the relative amount of NaCl to the total sample was reduced. This influence is examined in the next section.

Mixture with sugar and NaCl

When large amounts of sugar are added to water, the relation between amount of NaCl and conductivity of the sample changes. For this reason a new sample was examined which consisted always of the same amount of water and sugar but a varying amount of NaCl. The sample consisted of a sugar-water mixture with a permittivity of $\varepsilon = 54$ which is close to the average value of the human brain. 4 samples were prepared with the amount of NaCl varying from 0% to 3%. The conductivity and permittivity were measured for each sample. While the permittivity remained unchanged as expected, the influence on the conductivity can be seen in the following graph:

A linear fit of the data points delivered the following relation:

$$\sigma = 0,19 \cdot m + 0,16 \quad (3.4)$$

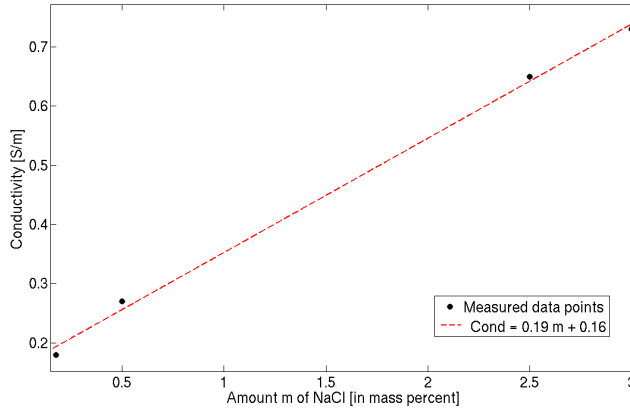


Figure 3.5: The conductivity of a sample with $\varepsilon = 54$ versus the mass percentage of NaCl inserted

This shows that with the addition of sugar, a much higher quantity of NaCl is needed to achieve the desired conductivity than what would be expected when just considering the same amount of pure water.

3.2.6 Preparation of a head phantom

Ingredients

In the following section the preparation of a phantom is described. The phantom consists of 3 different materials: The brain equivalent gel inside the skull, the plastic skull and the muscle equivalent gel around the skull. The materials needed for the construction of the phantom are listed in table 3.6.

Tools for the preparation

- Scale
- Electric heater with magnetic stirring function
- 2 big beakers (3 l)

Ingredient	Brain	Muscle	Purpose
Deionized water	1746 g	1900 g	basic ingredient
Sucrose	2280 g	2509 g	permittivity modifier
$NaCl$	136,2 g	90,8 g	conductivity modifier
NaN_3	0,8 g	0,5 g	preservative
$MnCl_2 \cdot 4H_2O$		0,5 g	T_1 modifier
Agar agar	80 g	80 g	gelling agent
Plastic skull			imitates human skull
Plasticine			sealing

Table 3.6: Ingredients for a realistic head phantom

- 1 small beaker (500 ml)
- 2 small plastic bottles
- bowl
- Head mold (Fig. 3.6)
- Kitchen wrap
- One bowl or plate large enough for the head phantom and small enough to fit into the coil



Figure 3.6: a) The still unpainted head mold b) The skull placed into the mold. Before putting the other half of the mold on the top, gel-spacers should be placed around the skull to prevent it from touching the walls when the mold is being moved.

Preparation of the mold

1. A cubic form (26cm x 26cm x 26cm) was filled up to a height of 11 cm with gypsum.
2. The head of a mannequin was placed into the still fluid gypsum so that half of the head was inside the gypsum and half of the head was outside.
3. After about 20 min when the gypsum has already started to solidify but was not yet completely solid, the head was removed from the gypsum. Therefore a negative form of the head remained in the gypsum. After solidification of the material, the same procedure was repeated with the other half of the head.
4. The finished mold was painted with some water-resistant colors. This preserves the gypsum from being attacked by liquid gels that are poured into the mold.

Preparation procedure

During preparation safety measures such as gloves should be taken, because of the high toxicity of Sodium Azide (NaN_3)!

1. Measure the mass of each ingredient.
2. Fill one big beaker with the deionized water, $NaCl$ and the NaN_3 for the brain equivalent phantom and dissolve all the ingredients thoroughly.
3. Fill the other big beaker with the deionized water, $NaCl$, NaN_3 and the $MnCl_2 \cdot 4H_2O$ for the muscle equivalent phantom and dissolve all the ingredients thoroughly.
4. During heating to approximately $50^\circ C$ and during constant stirring, dissolve all the sucrose in both the brain equivalent and muscle equivalent phantom.
5. Fill a portion of the liquid of both phantoms in a small plastic bottle each and measure the properties with the network analyzer. If some of the pa-

rameters vary from their designated value, adjust the mixtures by adding some more of the necessary ingredient.

6. Dissolve the agar agar in the brain equivalent mixture and heat it up to approximately 95°C . Pour the hot and still liquid gel into the plastic skull and let it cool down for solidification. After cooling seal the filling hole in the skull with some plasticine.
7. Fill about $\frac{1}{10}$ of the muscle equivalent liquid into a small beaker, add $\frac{1}{10}$ of the agar agar and heat it up to approximately 95°C . Pour the hot and still liquid gel into the bowl and let it cool down and solidify. After solidification cut the rigid gel into small stripes, which are then used as spacers between the mold and the skull.
8. With the help of the spacers place the skull into the mold (Fig. 3.6) so that the distance to each side is approximately equal. Close the mold and seal it tightly.
9. Dissolve about $\frac{9}{10}$ of the remaining agar agar in $\frac{9}{10}$ of the remaining muscle equivalent mixture and heat it up to approximately 95°C . Pour the still hot and liquid gel into the mold until the mold is completely filled. Let it cool down for at least a day for solidification.
10. Take the finished head out of the mold (Fig. 3.7). Because there is just a small layer of muscle gel between the skull and the head mold, it sometimes happens that some parts of the head phantom are ripped when taking it out. In this case dissolve the remaining agar agar in the remaining muscle equivalent liquid and heat it up until 95°C . Use this gel as a “repair kit” to repair any ripped parts of the phantom.
11. Wrap the phantom with some kitchen wrap and place it, to prevent squeezing of any parts, on a padded surface inside a large bowl.



Figure 3.7: The finished head phantom

3.2.7 Measuring the electrical parameters

The measurement of the permittivity and conductivity of the samples were performed with the network analyzer HB8510 by Agilent⁷. The network analyzer was made available for these measurements by Prof. Dr. Kremer⁸. The measurement setup for the network analyzer was done by Dr. Julius Tsuwi⁹ and an introduction on the measurement procedure was given by Joshua Rume Sangoro¹⁰.

Measurement system

A measurement of the reflection coefficient of a material provides the information to characterize the permittivity and permeability of the material. The network analyzer used consists of a signal source, a receiver and a display (Fig. 3.8).

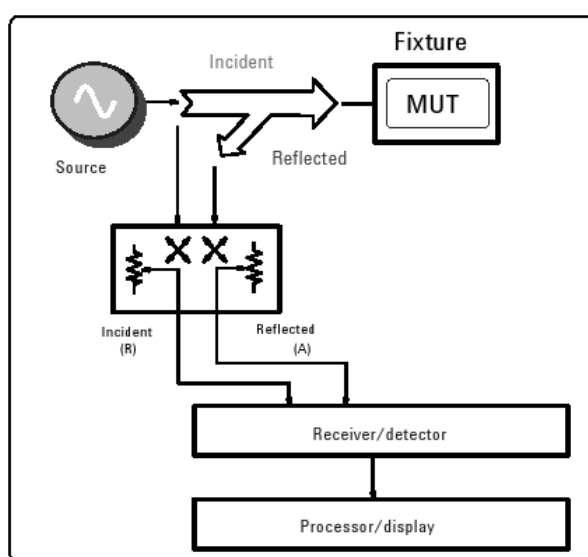


Figure 3.8: Network Analyzer [Agilent, 2005]

The source launches a signal at a single frequency to the material under test. The receiver is tuned to that frequency to detect the reflected signal from the material.

⁷formerly Hewlett Packard

⁸Department for molecular physics, University of Leipzig

⁹Department for chemistry and biochemistry, University of Bern

¹⁰Department for molecular physics, University of Leipzig

With the measured reflected signal \bar{R} (Fig. 3.9) and some known parameters about the measurement setup, the complex dielectric constant $\bar{\epsilon}$ of the examined substance can be calculated.

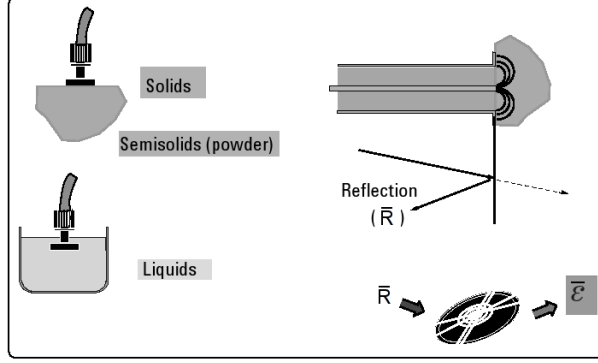


Figure 3.9: Coaxial Probe method. The coaxial probe is either inserted into the liquid or touching a flat face of the solid so that no air bubbles are between probe and sample¹². With the measured complex reflection coefficient \bar{R} the permittivity $\bar{\epsilon}$ of the sample can be calculated [Agilent, 2005]

The calculation of the complex dielectric constant $\bar{\epsilon} = \epsilon' - i\epsilon''$ of the sample is completed with equation (3.5) using a number of parameters acquired before and during measurement.

$$\frac{\bar{R} - P_x}{P_y - P_z} \cdot \frac{\bar{R} - P_y}{P_x - P_z} = \frac{\bar{\epsilon} - \bar{\epsilon}_x}{\bar{\epsilon}_y - \bar{\epsilon}_z} \cdot \frac{\bar{\epsilon} - \bar{\epsilon}_y}{\bar{\epsilon}_x - \bar{\epsilon}_z} \quad (3.5)$$

\bar{R} is the measured complex reflection coefficient of the sample. The values P_x, P_y, P_z are the reflection coefficients of the calibration substances. During calibration these values are measured and stored. The values $\bar{\epsilon}_x, \bar{\epsilon}_y, \bar{\epsilon}_z$ are the complex dielectric constants of the calibration substances. The values ϵ' and ϵ'' needed for their calculation are given by the Debye equations (3.6).

$$\epsilon'(\omega) = \epsilon_\infty + \frac{\epsilon_s - \epsilon_\infty}{1 + (\omega\tau)^2} \quad (3.6)$$

$$\epsilon''(\omega) = \frac{\epsilon_s - \epsilon_\infty}{1 + (\omega\tau)^2} \omega\tau \quad (3.7)$$

The calibration substances are air, deionized water and acetone. For air $\varepsilon_s, \varepsilon_\infty$ are taken to be 1, τ with $1 \cdot 10^{-16}$ is taken to be very small. The values for acetone are given in the literature [Tsuwi, 2007]. The values for deionized water are strongly temperature dependent and are calculated with Stogryn's equations [Stogryn, 1971]:

$$\varepsilon_0(T) = 87,74 - 4,0008T + 9,398 \cdot 10^{-4}T^2 + 1,410 \cdot 10^{-6}T^3 \quad (3.8)$$

$$\tau(T) = \frac{1}{2\pi} 1,1109 \cdot 10^{-10} - 3,824 \cdot 10^{-12}T + 6,938 \cdot 10^{-14}T^2 - 5,096 \cdot 10^{-16}T^3 \quad (3.9)$$

T is the temperature. The value ε_∞ for deionized water does not depend strongly upon the temperature and was taken to be 4,9.

Measurement procedure

1. *System calibration:* For this step the file "HP8510B System Calibration Tsuwi.vi" is required. The following settings are important for proper usage: Parameter (choose S11), Cal set (3.5mm Cal kit), sweep type (frequency list), sweep time (0.1), format (left: Real, right: Imaginary), Frequency list section, choose Num Points 401, Average (ON), factor (256), smoothing (ON), aperture (1%).

After starting the calibration the probes called "Open", "Short" and "Broad-band load" are needed for this calibration (Fig. 3.10 a)).

2. *Line calibration:* This step requires the file "Line Calibration Tsuwi.vi". Important settings are: VISA session (GPIB 17), Calibration type (1: open/water/2nd liquid)¹³, temperature (choose the approximate/nearest value to the current lab temperature).

During calibration again follow the pop-up instructions. As the second calibration liquid only acetone has proven to deliver reasonable results. Ethanol

¹³This is the ONLY programmed working option! The other options that are shown, do not deliver the right results according to Dr. Tsuwi

which is also available on the list and seems, due to its higher conductivity, more suitable for these experiments unfortunately did not deliver reasonable results.

3. *Sample measurement:* As the first sample measurement right after the calibration it is recommended to measure a sample with well known parameters such as deionized water or acetone and compare the measurement results with literature values. If the deviation between measured and literature values is very high, a new calibration is recommended (Fig. 3.10 b)).

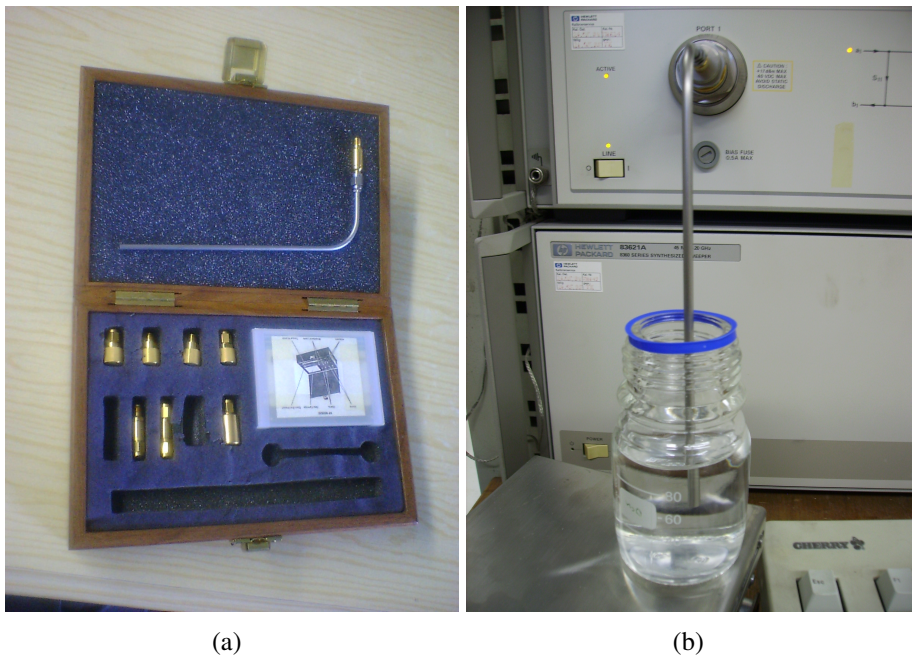


Figure 3.10: a) The different probes used for the calibration b) Measurement of a liquid sample

Error estimation

After each calibration of the network analyzer, a variation in the results could be observed. These variations are caused by random errors which cannot be excluded such as noise, drift or changes in the environment like temperature, humidity or pressure. Another cause of the errors may be due to some inconsistencies between the different calibration processes. For example, some contamination

of the connectors or physical movement of the test port cables after calibration. While the first random errors cannot be avoided, the second cause for errors was minimized as much as possible by e.g. inspecting the connectors and carefully handling the measurement device.

Method:

1. Measuring the parameters for acetone on 9 different days for 9 different calibrations. The distribution of the measured permittivities and conductivities can be seen in the histograms in fig.(3.11).

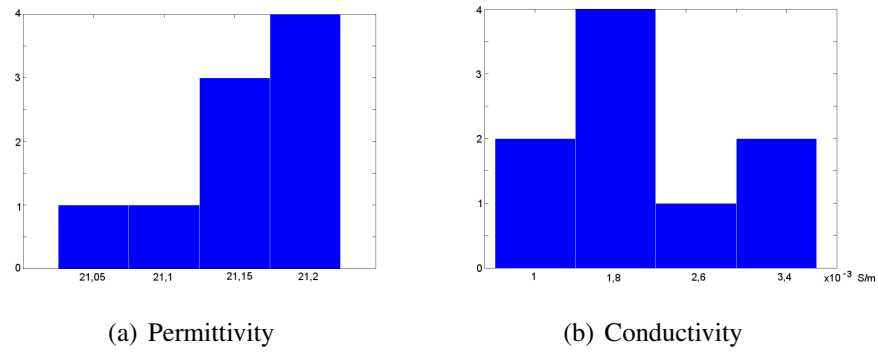


Figure 3.11: The measured parameters of acetone

The mean value for the permittivity is $\varepsilon = 21,16$ with a standard deviation of $STD = 0,05$.

The mean value for the conductivity is $\sigma = 0,002 \text{ S/m}$ with a standard deviation of $STD = 0,0008 \text{ S/m}$. This comparably high STD for the conductivity arises from the high noise at these low conductivities.

2. Measuring the parameters for a mixture of 61 g of sugar and 50 g of deionized water on 5 different days for 5 different calibrations. The distribution of the measured permittivities and conductivities can be seen in Fig.(3.12).

The mean value for the permittivity is $\varepsilon = 55,4$ with a standard deviation of $STD = 1,7$.

The mean value for the conductivity is $\sigma = 0,12 \text{ S/m}$ with a standard deviation of $STD = 0,01 \text{ S/m}$.

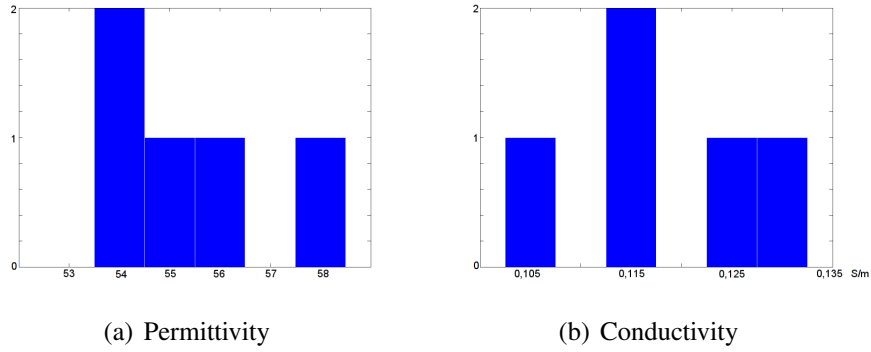


Figure 3.12: The measured parameters of the sugar-water mixture

3. Measuring the parameters of the Siemens phantom 5512 608 K2205, consisting of a mixture of 1, 24 g $NiSO_4 \cdot 6H_2O$ and 2, 62 g $NaCl$ per 1 l H_2O on 5 different days for 5 different calibrations. The distribution of the measured permittivities and conductivities can be seen in Fig.(3.13).

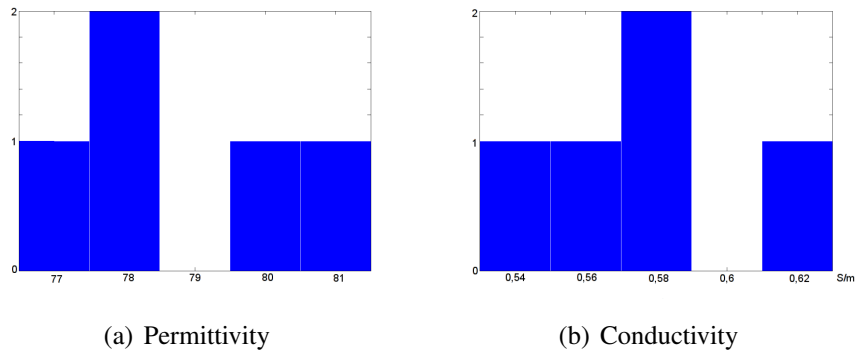


Figure 3.13: The measured parameters of the Siemens phantom 5512 608 K2205

The mean value for the permittivity is $\varepsilon = 79,1$ with a standard deviation of $STD = 1,5$.

The mean value for the conductivity is $\sigma = 0,58 S/m$ with a standard deviation of $STD = 0,03 S/m$.

3.3 Summary

Many different materials for the construction of MRI phantoms were examined. Numerous aqueous phantoms have been constructed, that are suitable for checking the equipment and validation of the numerical simulations. For the T_1 modification of the phantoms the usage of $MnCl_2 \cdot 4H_2O$ was preferred due to the comparable low toxicity of the substance. As a conductivity modifier $NaCl$ has been the best choice already for years. For the modification of the permittivity sucrose delivered very reliable values. Almost all of the gelling agents had the big disadvantage of solidifying in cold water. Even though the preparation of a homogeneous and solid substance succeeded on several occasions, the issue of air bubbles within the phantom was always present. Agar agar mixtures on the other hand are very easy to prepare and do not solidify in cold water. Therefore all the agar agar can be dissolved before heating up the mixture, this way almost completely avoiding air bubbles. Furthermore the durability of agar agar could also be extended to a great degree by adding preservatives and tightly sealing the phantom to prevent evaporation of the water. For the construction of the realistic head phantom, a mold made of gypsum was cast that has already proven very good stability even after the preparation of several phantoms. The head phantom incorporating 3 different materials is one of the most realistic head model available, with both anatomy and electrical parameters similar to the human head. Finally the measurement of the parameters with the network analyzer worked very reliably and delivered an error that was low enough to ensure the validity of simulations for the measured parameters.

Chapter 4

B_1^+ field inhomogeneities

4.1 Overview

In the first part of this chapter *Reasons for B_1^+ field inhomogeneities* (4.2) the behaviour of an electromagnetic wave in a dielectric medium and the reason of power absorption due to damping is described. Several explanations for the typical bright center that can often be observed in MRI images at high fields are discussed. In the second part *Overview over different B_1^+ mapping methods* (4.3) an overview of different methods for the measurement of the distribution of the B_1^+ field in the object are given. Finally the methods, which are most suitable for the current experiments are chosen. The experiments are performed with two different kinds of imaging coils. A birdcage coil from *Invivo* (similar to [Saylor & Reza, 2006]) and an 8-channel coil from *Rapid* [Weisser & Lanz, 2006].

4.2 Reasons for B_1^+ field inhomogeneities

4.2.1 Problems at high fields

In some older works [Röschmann, 1987][Bottomley & Andrew, 1978] it was suggested that due to the limited RF penetration dependent upon the frequency

of the radiation, MRI would be limited to field strengths below 5 Tesla. Later experiments have shown that it is still possible to perform MRI at higher field strengths (e.g. [Vaughan2001]). Unfortunately, the B_1^+ field can become very heterogeneous at higher field strengths.

4.2.2 Electromagnetic waves inside medium

When a RF wave with wavelength λ is travelling through a medium with relative permittivity ε_r and relative permeability μ_r its velocity of propagation in this medium compared to the vacuum is

$$c = \frac{c_0}{\sqrt{\varepsilon_r \mu_r}} = \frac{1}{\sqrt{\varepsilon_0 \varepsilon_r \mu_0 \mu_r}} \quad (4.1)$$

where c_0 is the speed of light in the vacuum. Since the B_1^+ field must be according to (2.7) applied at frequency ω_0 its wavelength in the medium is given by

$$\lambda = \frac{2\pi c_0}{\omega_0 \sqrt{\varepsilon_r \mu_r}} \quad (4.2)$$

When this wavelength is much larger than the dimensions of the sample, the assumption of a constant B_1^+ field throughout a homogeneous sample is justified. For small fields with a small ω_0 this condition is fulfilled but at for example 7 Tesla with an $\omega_0 = 297,2 \text{ MHz}$ the wavelength in the brain with an average relative permittivity of $\varepsilon = 52$ is about 12 cm . Thus the wavelength is comparable to or even smaller than the object to be imaged. The problems that accompany this fact will be discussed in the sections to follow.

Another problem is the interaction between the electric field component of the electromagnetic wave and the imaged medium. Since the medium can absorb power from the electromagnetic wave, heating of certain areas may occur. These interactions may vary significantly depending upon the electrical properties of the medium such as its conductivity.

4.2.3 Damping

Note: This explanation is using the far field approach. It considers a wave travelling far from the source. This is sufficient for explaining the effects that occur such as damping¹.

To describe the behaviour of an electromagnetic wave in a dielectric medium first the Maxwell equations for a conductive medium should be considered:

$$\operatorname{div} \mathbf{E} = \frac{\sigma}{\varepsilon_r \varepsilon_0} \quad (4.3)$$

$$\operatorname{div} \mathbf{B} = 0 \quad (4.4)$$

$$\operatorname{rot} \mathbf{E} = -\frac{\partial \mathbf{B}}{\partial t} \quad (4.5)$$

$$\operatorname{rot} \mathbf{B} = \mu_r \mu_0 \left(\sigma \mathbf{E} + \varepsilon_0 \varepsilon_r \frac{\partial \mathbf{E}}{\partial t} \right) \quad (4.6)$$

Using these equations it can be shown [Demtröder, 1999] that the behaviour of the electromagnetic field can be described by the following differential wave equation

$$\Delta \mathbf{E} = \varepsilon \mu \frac{\partial^2 \mathbf{E}}{\partial t^2} + \mu \sigma \frac{\partial \mathbf{E}}{\partial t}. \quad (4.7)$$

The term $\mu \mu_0 \sigma \frac{\partial \mathbf{E}}{\partial t}$ is responsible for the dampening of the wave in a conductive medium. When the conductivity is very small as is the case for oil, this term vanishes and the wave equation for an electromagnetic wave in vacuum can be acquired. A solution for the differential equation (4.7) is of the form

$$\mathbf{E}(\mathbf{r}, t) = \mathbf{E}_0 e^{i(\bar{\mathbf{k}}\mathbf{r} - \omega t)} \quad (4.8)$$

with $\bar{\mathbf{k}}$ denoting the complex wave vector

¹For an explanation of the field distribution of the electromagnetic field within the object in MRI, the near field approach is necessary, where the source of electromagnetic radiation is near the medium.

$$\bar{\mathbf{k}} = \mathbf{k}_0 + i\mathbf{k}_1 = \frac{\omega\bar{n}}{c_0}\mathbf{e}_{\mathbf{k}} + i\frac{\omega\Gamma}{c_0}\mathbf{e}_{\mathbf{k}}. \quad (4.9)$$

$\mathbf{e}_{\mathbf{k}}$ is the unity vector in direction of wave propagation, Γ is the extinction coefficient. It can be shown [Nolting, 1997] that for very low conductivities Γ approaches zero.

The physical meaning of Γ can be seen by inserting (4.9) into (4.8) which leads to

$$\mathbf{E}(\mathbf{r}, t) = \mathbf{E}_0 e^{-\Gamma(\omega/c)(\mathbf{e}_{\mathbf{k}} \cdot \mathbf{r})} e^{i[(\omega/c)\bar{n}(\mathbf{e}_{\mathbf{k}} \cdot \mathbf{r}) - \omega t]}. \quad (4.10)$$

This equation has the form of a damped wave travelling in the direction of \mathbf{k} . The strength of the damping is given by the extinction coefficient Γ . As the damping results in heating of the conducting medium, this effect may also cause problems during MRI due to unwanted excessive heating of the examined tissue. strong damping within body tissue was thought to make MRI experiments at frequencies over 220 MHz impossible [Röschmann, 1987].

But there exist effects which oppose the strong damping (Section 4.2.4).

4.2.4 Explanations for B_1^+ field inhomogeneities - depending upon the conductivity of the sample

Fortunately there exist additional effects which oppose the limited RF penetration and therefore make MRI possible at higher frequencies. Some of these are the same effects, which might also lead to typical B_1^+ field inhomogeneities like the bright center in MRI images.

Two of these effects are called field focusing and dielectric resonance. In the next section it will be shown that their effect depends very much on the conductivity of the sample. At conductivities like in the human head dielectric resonances are almost not observable anymore while the field focusing effect might still contribute to decrease the effects of damping. But recent experiments have shown that at higher conductivities the main reason for B_1^+ field inhomogeneities like a

high B_1^+ field magnitude in the center and a weak magnitude in the periphery are interferences of multiple coil elements.

Field Focusing and dielectric resonance

Two terms that were very often used in MRI to explain bright spots (Fig.4.1) especially in the middle of certain phantoms with high dielectric constant or the human brain, are the so called *Dielectric Resonance* and the *Field Focusing*.

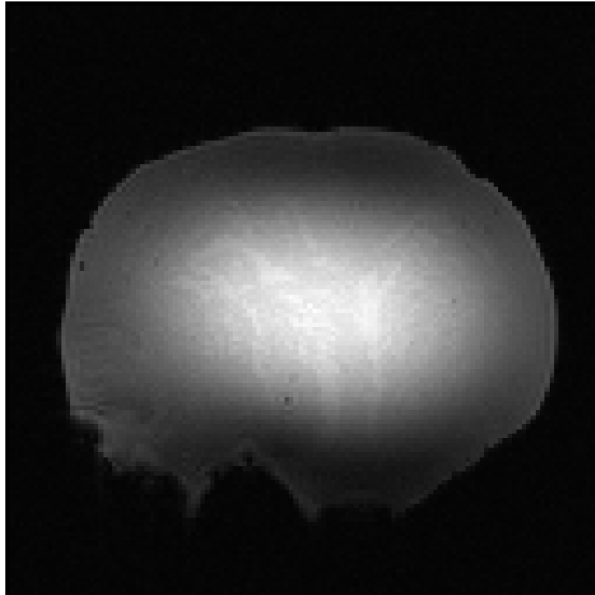


Figure 4.1: Picture of a headphantom taken with a GRE sequence showing the typical bright center in the middle of the phantom

According to Hoult [Hoult & Phil, 2000] dielectric resonance only occurs at specific frequencies related to the size of the sample and its dielectric constant. As described above, this would occur if the wavelength λ is related to the radius a of the phantom by the relation

$$n\lambda = 2a. \quad (4.11)$$

When a wave with a wavelength comparable to the phantom is reflected at the

boundary back into the phantom², interference between the waves inside the phantom can occur.

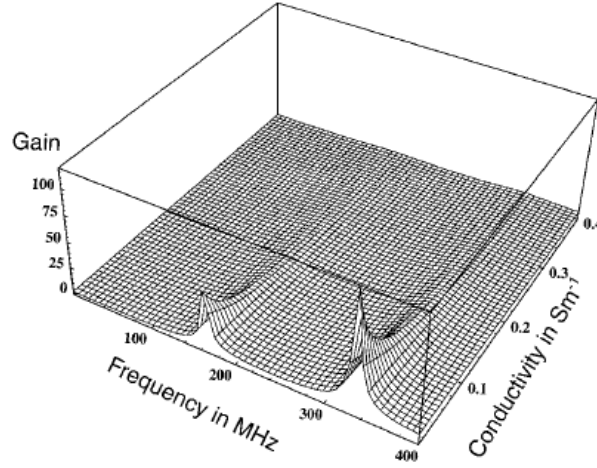


Figure 4.2: Enhancement of B_1^+ field strength towards the center as a function of frequency and conductivity of the sample. The radius of the sample is $r = 10 \text{ cm}$. At $\sigma = 0,4 \text{ S/m}$ almost no effect of the dielectric resonance can be observed anymore. [Hoult & Phil, 2000]

As can be seen in Fig. (4.2) with high conductivities such as in the human head³, the effect of dielectric resonance is reasonably damped.

An additional effect he referred to as field focusing. This effect always occurs at high frequencies, independent of the dimensions of the object, and also results in an increase in the B_1^+ field towards the center of the phantom.

(Fig.4.3) shows the relative amplitude of the B_1^+ field in a sample of pure water and a sample with conductivity $\sigma = 1 \text{ S/m}$ as a function of distance from

²For the refraction coefficient it holds:

$$n \propto \sqrt{\epsilon_r} \quad (4.12)$$

At the interface between medium 1 with n_1 and medium 2 with n_2 some part of the wave is reflected back into medium 1 and the other part can transmit into medium 2. It is possible to show that the reflectivity is larger when the difference between the refraction indices n_1 of medium 1 and n_2 of medium 2 is big [Demtröder, 1999].

³in the head $\sigma > 0,5 \text{ S/m}$

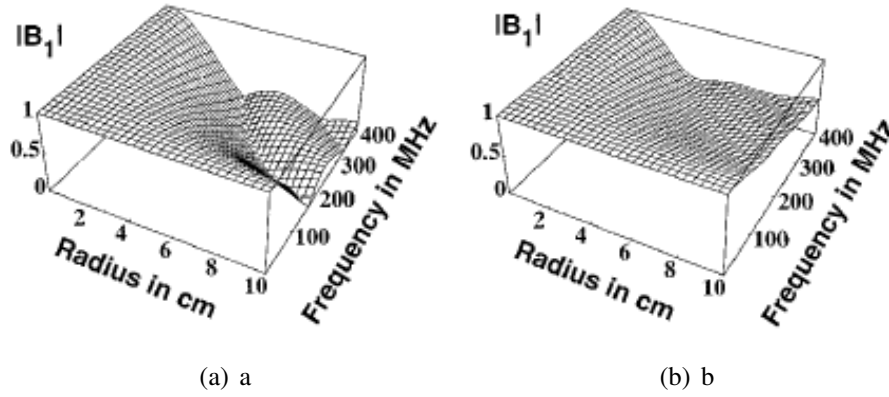


Figure 4.3: a) In a sample of deionized water, the B_1^+ field is very inhomogeneous at high frequencies. The field at the origin is much stronger than further out. b) In a water sample with conductivity $\sigma = 1 \text{ S/m}$ the field focusing effect is damped reasonably and the field at the periphery has risen appreciably compared to a) [Hoult & Phil, 2000].

the center of the phantom and the frequency. For even higher conductivities the field at the periphery would rise even more compared to the central part leading to a decreasing penetration depth of the electromagnetic radiation due to the strong damping (Section 4.2.3). To get a physical understanding of the field focusing effect, first the fourth Maxwell equation (4.6) will be considered. The term $\sigma \mathbf{E}$ stands for the free current density \mathbf{J}_e while the term $\epsilon_0 \epsilon_r \frac{\partial \mathbf{E}}{\partial t}$ represents the displacement current density \mathbf{J}_d . [Vaughan, Hetherington, Otu, Pan, & Pohost, 1994]

The equation can be rewritten by introducing the magnetic vector potential \mathbf{A} and the electric scalar potential ϕ

$$\text{rot} \mathbf{B} = \mu_r \mu_0 (\sigma + i\omega \epsilon_r \epsilon_0) (-i\omega \mathbf{A} - \text{div} \phi) \quad (4.13)$$

The eddy current density $\mathbf{J}_e = -i\omega \sigma \mathbf{A}$ is induced by the alternating B_1^+ field. Due to Lenz', law it again induces a magnetic field that is opposed to the applied B_1^+ field and therefore weakens it. The displacement current density $\mathbf{J}_d = \omega^2 \epsilon_r \epsilon_0 \mathbf{A}$ is negligible for low frequencies. In this case the counteracting eddy

current shielding prevails and lowers the B_1^+ field with increasing distance from the source.

However, at high frequencies this second term becomes quite significant. The magnetic field induced by the displacement current points in the same direction as the applied alternating field and therefore enhances the B_1^+ field towards the center.

B_1^+ field inhomogeneity due to interference between coil elements

Recent studies have shown that the explanations in section (4.2.4) for observed B_1^+ field inhomogeneities such as the central brightening are insufficient. These effects would also have to be visible, if just one simple coil adjacent to the object, also called a *surface coil* is the source of the RF radiation. But in simulations with just one surface coil and a sample of water, the middle of the phantom stayed dark. And in objects with the same conductivity as the human head, the damping is so high that the reflected waves do not play an important role anymore. Dielectric resonances, if they appear at all, are almost unobservable (see also Fig. 4.2).

Another explanation for the central brightening is delivered by Collins and Moortele [Collins, Liu, Schreiber, Yang, & Smith, 2005][de Moortele et al., 2005]. If there are two sources of travelling waves with currents in opposing directions (= 180° out of phase) and the waves from each source travelling through the same media for the same distance, there is a location of constructive magnetic field interference midway between the sources (Fig. 4.4).

This effect can even be observed when increasing the conductivity to further dampen resonance effects. While a single coil at a certain frequency might only deliver a brightening in the region adjacent to the coil with a dark spot in the center of the phantom, two coils in a symmetric system would result in a brightening of the center. On the other hand, destructive interference between coil elements that can occur in the other regions can result in a reduced SNR of the periphery compared to the center of the coil. By comparing images which contained

1. the magnitude of sums (MOS) of the several images from each coil element,

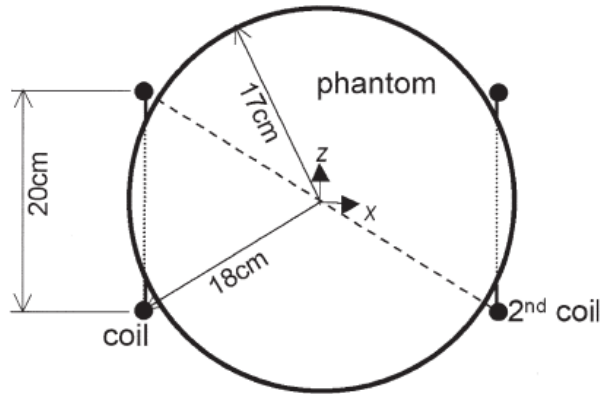


Figure 4.4: Two circular surface coils with a spherical phantom in the middle. The dashed line goes between currents of opposite directions. Constructive interference takes place at the midpoint of the dashed line. [Collins et al., 2005]

that means, that interferences between the coil elements play an important role and can cause interferences

2. and the sum of magnitudes (SOM) which just added up the absolute value of each coil element and where interferences therefore do not play a role

Moortele showed that these destructive interferences are responsible for the typical image intensity profile at high fields. However, he also stated that these problems may be overcome by using multichannel receiver arrays.

Even if the object is not a sphere and not symmetrical such as the head phantom (Section 3.2.6), interferences may occur. Furthermore interferences between more than two coil elements may occur when using certain coils. But these interferences are not necessarily in the center of the phantom but may also appear in the periphery. Additionally there may be several regions with interferences within the object. These effects make an a-priori B_1^+ field estimation within an object very difficult. Therefore electromagnetic field simulations (Section 6.2) and B_1^+ field mapping experiments are used for acquiring information about the B_1^+ field distribution during a MRI experiment.

4.3 Overview of different B_1^+ mapping methods

In this section an overview of several different B_1^+ mapping methods is given. Before the description of the methods a short introduction to the nominal and actual flip angle is given, which is necessary for the understanding of the B_1^+ mapping methods described. At the end of the chapter after consideration of the advantages and disadvantages of the methods, two methods are chosen that are best suitable for the experiments in this thesis. If the method described was actually applied, images with the results can be seen within the description of the method. If the effort to implement a method such as programming a new sequence surpassed the advantages the method could deliver for the desired purposes, only the description is provided.

4.3.1 Nominal and actual flip angle

As shown in equation (2.28), the flip angle is dependent upon the strength of the B_1^+ field of a rectangular pulse by

$$\varphi(r) = \gamma B_1^+(r) \tau. \quad (4.14)$$

The B_1^+ field strength is determined by the power delivered to the RF coil. When the B_1^+ field is completely homogeneous throughout the phantom, the power required to produce a RF pulse which will give the maximum signal in a normal GRE sequence is therefore the power that is needed for a 90° pulse. However, as explained above there are usually variations in the B_1^+ field. This may result in several problems:

During imaging, a variation in flip angle over the whole phantom might result in strong variations of the signal in different regions of the object to be imaged.

Another problem is that the power needed for achieving a desired flip angle at a certain region of interest in the phantom, may produce a higher flip angle in another region. If this delivered power is strong enough to heat up the examined tissue in that region, this B_1^+ field inhomogeneity is an additional major issue and

may be hazardous for the subject. The flip angle that is set in the protocol is called the *nominal flip angle* φ_n . When a certain region in the phantom is considered, the flip angle in this region might differ from the nominal flip angle due to inhomogeneities of the B_1^+ field. The flip angle that is actually achieved in a given voxel is called the *actual flip angle* φ_a and it is related to the nominal flip angle by the flip angle scaling factor ζ :

$$\varphi_a(r) = \zeta(r)\varphi_n. \quad (4.15)$$

The B_1^+ mapping methods to be described later are utilised for obtaining information concerning the actual flip angle $\varphi_a(r)$ at a certain position r in the imaged object.

4.3.2 Double angle method using Gradient Echo

Insko proposed in 1993 a method for mapping the B_1^+ field by taking the ratio of two images with different flip angles [Insko & Bolinger, 1993]. In an ideal steady-state gradient-echo sequence, the signal intensity is given by [Wang, Mao, Yang, Smith, & Constable, 2005]:

$$SI_{GE}(r) = M_0(r) \cdot \sin \varphi(r) \cdot \frac{(1 - E_1)}{1 - E_1 E_2 - (E_1 - E_2) \cos \varphi(r)} \cdot e^{-TE/T_2(r)} \cdot B_1^-(r) \quad (4.16)$$

where $E_1 = \exp -TR/T_1(r)$, $E_2 = \exp -TR/T_2^*(r)$, the $B_1^-(r)$ field is the reception sensitivity at position x and M_0 the equilibrium longitudinal magnetization. Since in our experiments it is always $TR \gg T_2^*$, the term E_2 can be set to zero.

The term steady-state refers to the fact that there are several repetitions of RF pulses during the sequence. If the TR is too short, the longitudinal magnetization is unable to completely recover to its equilibrium value, but will instead approach

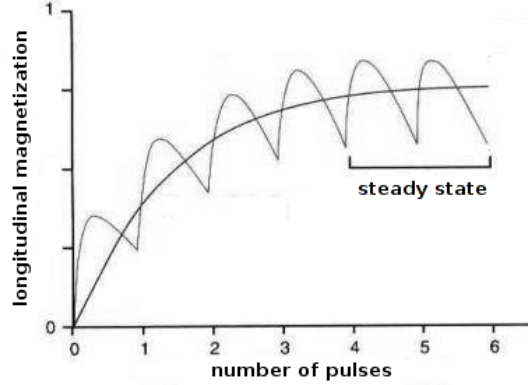


Figure 4.5: When the longitudinal magnetization cannot completely relax before each new pulse, it finally reaches a constant value called the steady state.

steady-state conditions with a constant flip angle after several repetitions⁴.

To prevent the system from entering a steady-state and produce with every pulse the same flip angle, TR has to be chosen so that $TR \gg T_1$. Then equation 4.16 can be simplified to:

$$SI_{GE}(r) = M_0(r) \cdot \sin(\varphi(r)) \cdot e^{-TE/T_2(r)} \cdot S(r) \quad (4.17)$$

$$= M_0(r) \cdot \sin(\gamma B_1^+(r)\tau) \cdot e^{-TE/T_2(r)} \cdot B_1^-(r) \quad (4.18)$$

Some of the values in this equation are known and some of them are unknown. Since typically nothing is known a priori about the sample, the length of the magnetization vector M_0 is unknown. Furthermore the strength of the B_1^+ field and other coefficients of the signal strength are also unknown. The only known values are the duration of the application of the B_1^+ field⁵ and the nominal flip angle.

⁴If there is for example a repetition of several 10° pulses, the first pulse flips the magnetization into the transversal plane, producing a flip angle of 10° to the z-axis. When the magnetization does not completely relax to its starting position, the next 10° pulse will flip it not into the same plane, but will produce a flip angle $> 10^\circ$, resulting in a different transversal magnetization than before. After several repetitions the system enters a *steady-state*, producing with every repetition the same transversal magnetization (Fig. 4.5).

⁵Also called the pulse length

To remove the unknowns, the ratio of two gradient echo images is taken with different flip angles φ_1 and φ_2 but with all the other parameters held constant. The following calculations consider always one voxel, therefore the notation φ instead of $\varphi(r)$ is used. Choosing the pulse length or the pulse amplitude such that

$$\varphi_2 = 2\varphi_1 \quad (4.19)$$

the signal ratio is:

$$\frac{S_1}{S_2} = \frac{\sin(\varphi_2)}{\sin(\varphi_1)} = \frac{\sin(2\varphi_1)}{\sin(\varphi_1)}. \quad (4.20)$$

With the following relation for the sinus function:

$$\sin(2\varphi) = 2 \cos(\varphi) \sin(\varphi) \quad (4.21)$$

the relation between signal ratio and flip angle can be acquired:

$$\frac{S_1}{S_2} = \frac{2 \cos(\varphi) \sin(\varphi)}{\sin(\varphi)} = 2 \cos(\varphi) \quad (4.22)$$

With the signal of two measurements the flip angle can therefore be determined by:

$$\varphi = \arccos\left(\frac{S_1}{2S_2}\right) = \gamma B_1^+ \tau \quad (4.23)$$

and the magnitude of the transmit field by:

$$B_1^+ = \frac{1}{\gamma \tau} \arccos\left(\frac{S_1}{2S_2}\right). \quad (4.24)$$

Experiment: A B_1^+ map of the orange oil phantom in the Invivo coil was acquired with the described method. The sequence was a gradient echo sequence with $TR = 5000 \text{ ms}$, $TE = 4, 8 \text{ ms}$, resolution $1 \text{ mm} \times 1 \text{ mm} \times 5 \text{ mm}$ and nominal flip angle of $\varphi_1 = 60^\circ$. A transversal, coronal and sagittal⁶ slice through the center of the coil were acquired. Figure 4.6 shows the flip angle distribution acquired by

⁶The orientation of the slices is described in section 5.2.

the double angle method.

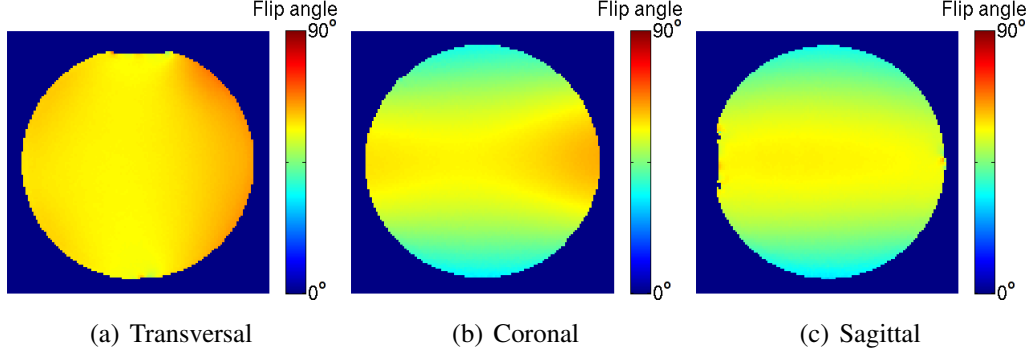


Figure 4.6: B_1^+ maps of the orange oil phantom in the Invivo coil with a nominal flip angle of $\varphi_n = 60^\circ$ acquired with the double angle method. The scale shows the flip angle in degrees.

The problem for a weak B_1^+ field is that the results are very noisy (Fig. 4.7).

Due to the fact that the total signal received consists of the desired signal from the sample and the unwanted noise

$$S_{total} = SI_{GE} + noise \quad (4.25)$$

the ratio $\frac{SI_1 + noise_1}{2(SI_2 + noise_2)}$ becomes very sensitive to slight changes due to the noise. And because for small flip angles

$$\sin(\varphi) \approx \varphi \quad (4.26)$$

it can easily happen that the ratio in (4.25) becomes greater than “1” which would result in an error when taking the arccos of that value. Instead of an error, in an image reconstructed with MatLab such a pixel would contain the value “0”.

$$\frac{S_1 + noise_1}{2(S_2 + noise_2)} = \frac{\sin(2\varphi_1) + noise_{1b}}{2(\sin(\varphi_1) + noise_{2b})} \approx \frac{2\varphi_1 + noise_{1b}}{2(\varphi_1 + noise_{2b})} \approx 1 \quad (4.27)$$

According to equation (4.17) $noise_{1b/2b}$ are $\frac{noise_{1/2}}{M_0 \cdot e^{-TE/T_2} \cdot B_1^-(r)}$. Since with increasing SNR the values $noise_{1b/2b}$ decrease, smaller flip angles can be distinguished.

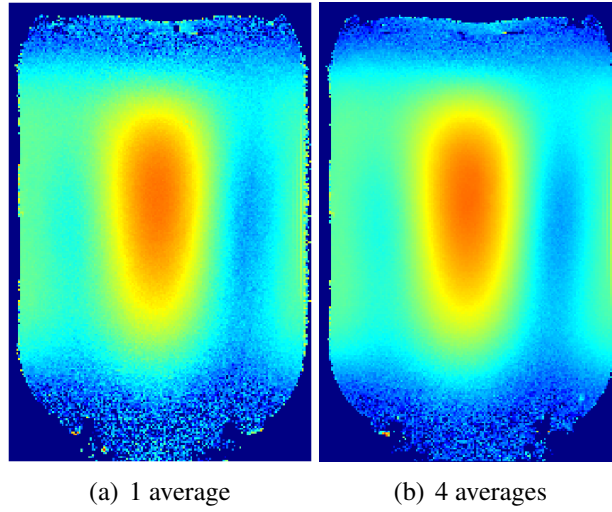


Figure 4.7: B_1^+ maps of a coronal slice of the Sugarphantom (Table 3.3) in the Rapid coil with a nominal flip angle of $\varphi_n = 60^\circ$ acquired with the double angle method. For low flip angles even improving the SNR of the images by taking 4 averages does not increase the final B_1^+ map considerably. On the other hand the scanning times increase by a factor of 4.

But in Fig. (4.7) it can be seen that the improvement of the B_1^+ map quality by increasing the SNR is not very high. For the reasons shown above, better results may be acquired when measuring with higher flip angles. The nominal flip angles which deliver the best results are $\varphi_1 = 60^\circ$ and $\varphi_2 = 120^\circ$ [Stollberger & Wach, 1996].

Another drawback of the double-angle method is the long time duration of the sequences. Since before each φ_1 and φ_2 pulse the magnetization must be allowed to completely relax, sequences with a $TR > 5T_1$ have to be used. This makes this method very time consuming and not very practical for invivo studies.

4.3.3 Double angle method using Spin-Echo

Insko proposed in 1993 another B_1^+ mapping method using the ratio of two images acquired with a spin-echo sequence [Insko & Bolinger, 1993]. The signal intensity $I(r)$ of a spin echo sequence without transversal coherence and non-interacting spins may be written as [Bernstein et al., 2004]:

$$SI_{SE}(r) = M_0(r) B_1^-(r) \sin(\varphi_1(r)) \sin^2\left(\frac{\varphi_2(r)}{2}\right) \cdot \frac{1 + (\cos \varphi_2(r) - 1)e^{-(TR - \frac{TE}{2})/T_1(r)} - \cos \varphi_2(r) E_1}{1 - \cos \varphi_1(r) \cos \varphi_2(r) E_1} E_2 \quad (4.28)$$

where TR is the repetition time, TE the echo time, $\varphi_1(r)$ the angle of the excitation pulse, $\varphi_2(r)$ the angle of the refocusing pulse, $E_1 = \exp -TR/T_1(r)$, $E_2 = \exp -TE/T_2^*(r)$ and $B_1^-(r)$ the reception sensitivity of the coil. The following calculations are performed for a single voxel, therefore the notation φ instead of $\varphi(r)$ is used. A $\varphi_1 - \tau - \varphi_2 - \tau$ spin echo image and a $\varphi_{1b} - \tau - \varphi_{2b} - \tau$ spin echo image with $\varphi_2 = 2\varphi_1$ and $\varphi_{2b} = 2\varphi_{1b}$ provide the following ratio between the two images:

$$R = \frac{\sin^3 \varphi_1}{\sin^3 \varphi_{1b}} \quad (4.29)$$

For the spin echo sequence a phase cycling scheme [Bodenhausen, Freeman, & Turner, 1977] must be used to eliminate signals other than the signal from the spin echo.

If φ_{1b} is chosen so that $\varphi_{1b} = 2\varphi_1$, the relation can be rewritten as:

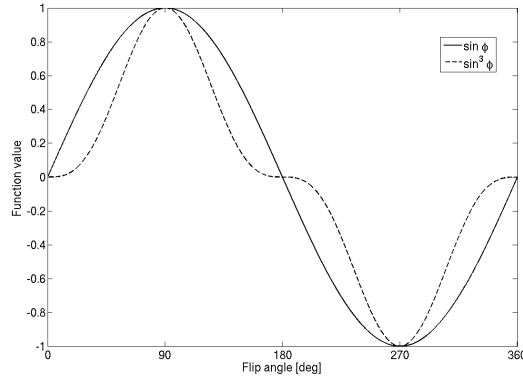
$$R = \frac{1}{(2 \cos \varphi_1)^3} = \frac{1}{(2 \cos(\gamma B_1^+ \tau))^3} \quad (4.30)$$

The magnitude of the B_1^+ field can then be calculated by:

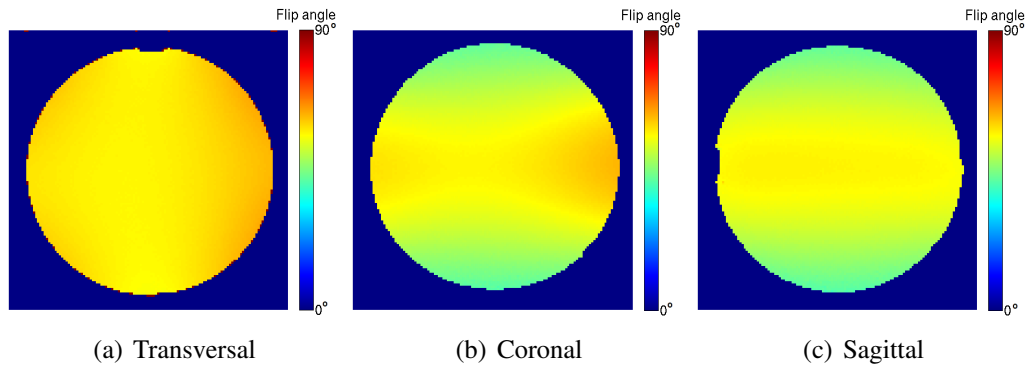
$$B_1^+ = \frac{1}{\gamma \tau} \arccos\left(\frac{1}{(8R)^{\frac{1}{3}}}\right) \quad (4.31)$$

It can be seen in Fig.(4.8) that the function is very steep between 20° and 160° but very flat at 0° and 180° . Therefore the best choice for flip angles are $\varphi_1 = 60^\circ$ and $\varphi_2 = 120^\circ$ or $\varphi_1 = 120^\circ$ and $\varphi_2 = 240^\circ$, both because they are symmetric around the $90^\circ - 180^\circ$ and because they lie at a rapidly changing part of the function, therefore being very sensitive to even small changes in B_1^+ . This behaviour can be very useful when measuring slight changes in very homogeneous slices.

Experiment: A B_1^+ map of the orange phantom in the Invivo coil was acquired

Figure 4.8: The functions $\sin \varphi$ and $\sin^3 \varphi$

using the described method. The sequence parameters were $TR = 4000 \text{ ms}$, $TE = 15 \text{ ms}$, resolution $1 \text{ mm} \times 1 \text{ mm} \times 5 \text{ mm}$, $\varphi_1 = 60^\circ$ and $\varphi_2 = 120^\circ$. The resultant images can be seen in Figure (4.9).

Figure 4.9: B_1^+ maps of the orange oil phantom in the Invivo coil acquired with the double angle method using a SE sequence

The images show basically the same quality like the double angle method using a GRE sequence. The better quality for homogeneous images is, if it exists at all, almost invisible.

4.3.4 Double angle method with saturation pulse and EPI readout

Since the standard double angle method (Section 4.3.2) described before requires a very long TR ($TR > 5T_1$) to prevent saturation effects from occurring this method is very slow. Therefore, Cunningham addressed this issue by using a saturation pulse and an EPI⁷ readout [Cunningham, Pauly, & Nayak, 2006]. The saturation pulse ensures that an identical M_z is achieved before the φ_1 and φ_2 pulses. Therefore it is not necessary to wait for full relaxation to avoid a T_1 bias. Additionally, the EPI readout speeds up the image acquisition. In a comparison between the standard method and the modified version by Cunningham, Wade found that for achieving the same quality of the images, both sequences needed almost the same scanning time [Wade, 2007]. Due to the strong possibility of a decrease of the image quality with an implementation of an EPI readout, this method was not implemented.

4.3.5 Multi angle approach

This B_1^+ mapping method is similar to the method described above. Equation (4.17) shows that the signal is proportional to the sine of the flip angle is used. Using (4.15), equation (4.17) can be also written as

$$SI_{GE}(r) = a_1(r)(\sin(a_2(r) \cdot \varphi_n)). \quad (4.32)$$

Several images taken at different nominal flip angles φ_n deliver a different signal $SI_{GE}(r)$ at the position r . These data pairs for each voxel can be fitted to equation (4.32) [Ibrahim, Mitchell, Abraham, & Schmalbrock, 2007], delivering the fitting parameters $a_1(r)$ and $a_2(r)$. Fig.(4.10) shows the fitting procedure for one voxel.

Parameter $a_1(r)$ contains both the proton density and the B_1^- -field dependence as a function of position. Therefore, for a phantom with uniform proton density as is a homogeneous oil or water phantom, $a_1(r)$ is linearly proportional to the

⁷Echo Planar Imaging [Schmitt, Stehling, Turner, & Mansfield, 1998]

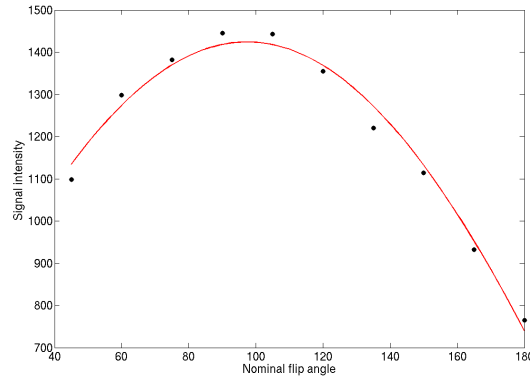


Figure 4.10: The signal intensity of one voxel for different nominal flip angles is fitted to the sinus curve from equation (4.32).

magnitude of the B_1^- -field at position r . For the absolute value of B_1^- , the values of M_0 and e^{-TE/T_2} according to equation (4.17) must be known. The product $a_2(r) \cdot \varphi_n$ gives the actual flip angle at position r and is therefore proportional to B_1^+ . The magnitude of the B_1^+ field can be acquired by using equation (4.14).

Experiments:

- The orange oil phantom was placed in the Invivo coil. With a GRE sequence, $TR = 5000\text{ ms}$, $TE = 4,8\text{ ms}$ and resolution of $1,5\text{ mm} \times 1,5\text{ mm} \times 3\text{ mm}$, 5 images were acquired for 5 different nominal flip angles ranging from 60° to 120° .
- The orange oil phantom was placed in the Rapid coil. With a GRE sequence, $TR = 5000\text{ ms}$, $TE = 4,8\text{ ms}$ and resolution of $1\text{ mm} \times 1\text{ mm} \times 3\text{ mm}$, 10 images were acquired for 10 different nominal flip angles ranging from 45° to 180° (Fig. 4.10).

The acquired data was fitted to equation (4.32). The resultant fitting parameter maps which are proportional to B_1^+ and B_1^- can be seen in figure 4.11.

Due to the fact that more than two images are taken, the flip angle maps acquired with the multi angle approach are less noisy than the ones taken with the normal double angle method. The problem with this method is the long scanning time due to the larger number of images that have to be taken. This makes it even more

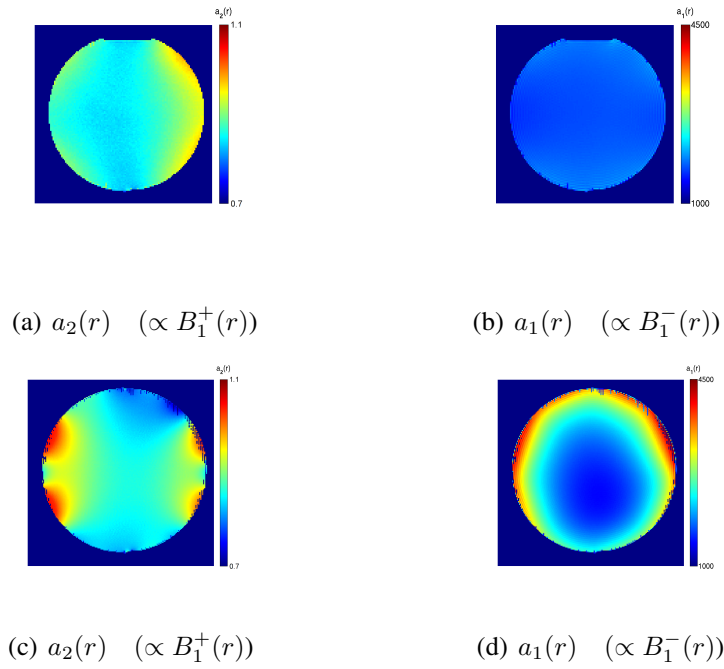


Figure 4.11: The transmit field B_1^+ and the receive field B_1^- for a transversal slice of the orange oil phantom in the Invivo coil (upper row) and in the Rapid coil (lower row). The scaling bars show the magnitude of the fitting parameters $a_1(r)$ (proportional to $B_1^-(r)$) and $a_2(r)$ (proportional to $B_1^+(r)$). The lines at the side of the phantom are a result of problems with the fitting procedure in noisy regions.

time consuming than the double angle method. In addition, figure 4.11 shows that both the field distribution of the B_1^+ field and the B_1^- field are more homogeneous for the Invivo coil⁸.

4.3.6 B_1^+ mapping method from SIEMENS Work-in-progress (WIP) package

Similar to the double angle method, this B_1^+ mapping sequence basically calculates the B_1^+ field from the ratio of the signal of two images, but this time a spin echo and a stimulated echo [Feiweier, 2006]. The timing diagram of the sequence can be seen in figure (4.12).

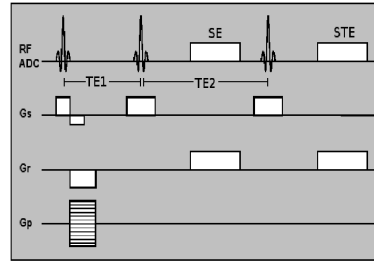


Figure 4.12: Schematic timing diagram of the B_1^+ mapping sequence from the SIEMENS WIP package.

For a stimulated echo (STE) and a spin echo (SE) the signal intensities are given by [Hennig, 1991]:

$$SI_{STE}(r) = \frac{1}{2} \sin(\varphi_1(r)) \sin(\varphi_2(r)) \sin(\varphi_3(r)) e^{-TE_2/T_1(r)} \cdot C(M_0(r), B_1^-(r), TE_1, T_2(r)) \quad (4.33)$$

$$SI_{SE}(r) = \sin(\varphi_1(r)) \sin\left(\frac{\varphi_2(r)}{2}\right) \cdot C(M_0(r), B_1^-(r), TE_1, T_2(r)) \quad (4.34)$$

where φ_1 is the flip angle of the excitation pulse, φ_2 the flip angle of the first refocusing pulse and φ_3 the flip angle of the second refocusing pulse. TE_2 is the

⁸Recent experiments have shown that these inhomogeneities for the Rapid coil can be decreased by a retuning of coil.

time duration between the two refocusing pulses and T_1 the longitudinal relaxation time. The constant C depends on the magnetization vector length M_0 , the reception sensitivity B_1^- , the time duration TE_1 between the excitation and the first refocusing pulse and the transversal relaxation time T_2 . For a multislice experiment the flip angles are chosen so that $\varphi_1 = \varphi_2 = \varphi_3$. Then the ratio of the two signals is given by:

$$SI_{STE}(r)/SI_{SE}(r) = (\cos \varphi_1(r) + 1)e^{-TE_2/T_1(r)} \quad (4.35)$$

The flip angle can then be evaluated using

$$\varphi_1(r) = \arccos\left(\frac{SI_{STE}(r)}{SI_{SE}(r)} \cdot e^{TE_2/T_1(r)} - 1\right) \quad (4.36)$$

For each additional slice three more pulses $\varphi_1, \varphi_2, \varphi_3$ are applied within the same TR . This is in contrast to the normal double angle method using a GRE sequence, where each new slice demands a new pulse in a new TR . Therefore taking too many slices can lead to problems with the SAR.

To minimize the effect of the term e^{TE_2/T_1} the smallest possible TE_2 is chosen. Additionally, several measures are taken to reduce deteriorating T_1 effects. The different methods for reducing these effects are:

1. Merge the results of multiple measurements
2. Assume constant mean T_1 for whole object
3. Perform T_1 estimation measurement

Method 1. and 3. lead to an increase in the scanning time.

Experiment: The orange oil phantom was scanned in the Invivo coil using the described method. A transversal, coronal and sagittal slice were acquired with the sequence “b1map_397_hires”. The imaging parameters were $TR = 1000 \text{ ms}$ and $TE = 14 \text{ ms}$, resolution $1 \text{ mm} \times 1 \text{ mm} \times 5 \text{ mm}$ and nominal flip angle of $\varphi_n = 90^\circ$. The acquired image can be seen in Fig.(4.13).

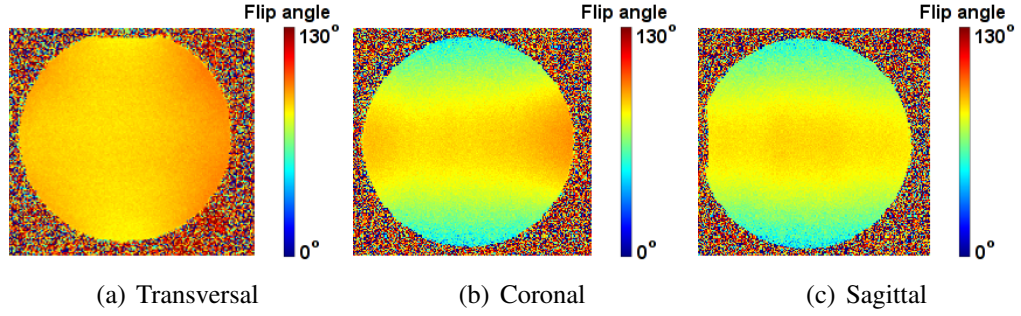


Figure 4.13: B_1^+ maps of the orange oil phantom in the Invivo coil acquired with the sequence *blmap397hires* from the SIEMENS WIP package

4.3.7 Method using the signal null at 180°

Dowell and Tofts provide another method to deal with the long scanning times that are necessary for many of the B_1^+ mapping methods [Dowell & Tofts, 2007]. This method uses the 180° signal null to construct a flip angle map independent of T_1 , T_2 and proton density. For a gradient echo experiment, the signal intensity can be describe by equation (4.16).

In the double angle method TR was chosen to be very long to prevent any saturation effects from occuring. The behaviour of the signal intensity for different ratios of TR and T_1 can be observed in Fig.(4.14).

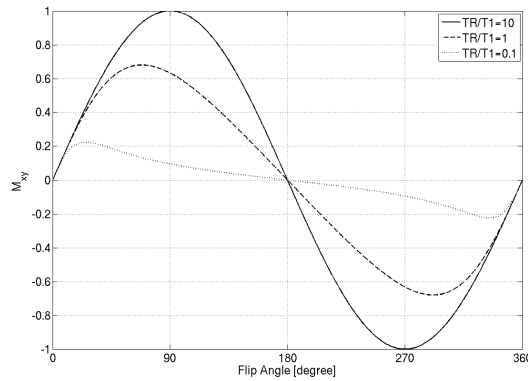


Figure 4.14: The transverse magnetization versus the actual flip angle for different ratios of TR/T_1

The signal intensities are dependent on the ratio TR/T_1 as long as $\varphi_a \neq 180^\circ$.

Therefore, it is impossible to determine the factor ζ between φ_n and φ_a in equation (4.15) without the knowledge of T_1 . But at $\varphi_a = 180^\circ$ the signal intensity is zero irrespective of T_1 . Hence, at every location r the nominal flip angle $\varphi_n(r)$, that yields a signal null, corresponds to $\varphi_a = 180^\circ$. Thus, the flip angle scaling factor $\zeta(r)$ (4.3.1) can be determined by:

$$\zeta(r) = \frac{180^\circ}{\varphi_n^{null}(r)} \quad (4.37)$$

To determine the flip angle distribution over the whole object, the fact that the signal intensity varies approximately linearly with respect to the flip angle in the region where $\varphi_a \approx 180^\circ$ is used. Therefore, by acquiring sets of images with different flip angles in this linear region, the corresponding signal intensity from position r may be fitted to a straight line to determine $\varphi_n^{null}(r)$, and hence $\zeta(r)$, over all r in the presence of B_1^+ inhomogeneity.

Experiment: A B_1^+ measurement of the orange oil phantom in the Invivo coil with the described method should be taken. 3 images at nominal flip angles of $\varphi_n = 145^\circ, 180^\circ, 215^\circ$ were acquired. The sequence was a GRE sequence with $TR = 700\text{ ms}$, $TE = 4, 8\text{ ms}$ and a resolution of $3\text{ mm} \times 3\text{ mm} \times 3\text{ mm}$. The scanner only produces positive image magnitudes. But since for the linear fit some signal intensities have to be negative (Fig. 4.14), the signal intensity of the same voxel in the 3 different images was allocated the signs (+ + +), (+ + -) and (+ - -) and finally the signs which delivered the best fit were taken for these voxels⁹. The repetition time for all sequences was $TR = 700\text{ ms}$ and the echo time $TE = 4, 8\text{ ms}$. A B_1^+ map acquired with this method can be seen in Fig.(4.15).

Problems: Due to the high flip angle used for that method, the SAR value can become very high, therefore requiring a long TR to stay within the limits. With the orange phantom in the Rapid coil and using a flip angle of 215° , a TR time of $TR = 700\text{ ms}$ had to be used to stay within the SAR limit. With such long TR times the major advantage of this method, the shorter scanning time, is reduced. The next problem is that the linearity approximation is just valid for a

⁹The sign (- - -) delivers the same φ_n like (+ + +)

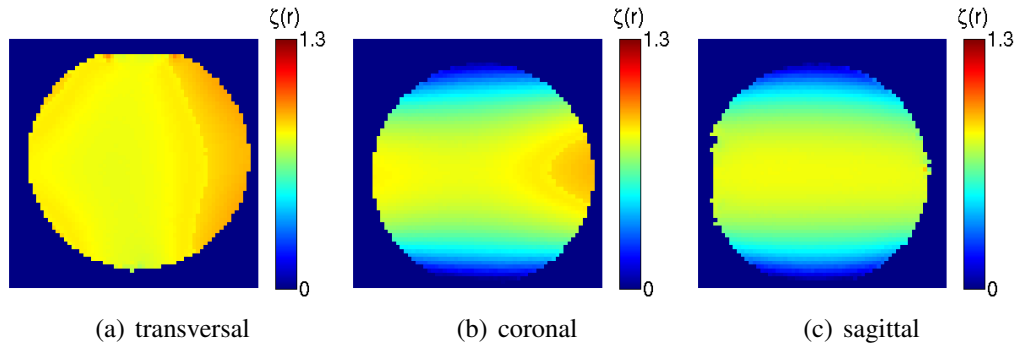


Figure 4.15: A flip angle map of the orange oil phantom in the Invivo coil using the signal null method developed by Dowell and Tofts. The scale bar shows the scaling factor $\zeta(r)$. The reason for these “jumps” in the magnitude is given below.

limited range of flip angles. For selective pulses there is the strong possibility, as described in section (5.4.2), that a flip angle that is much lower than the nominal flip angle of $\varphi_n = 180^\circ$ will be delivered to the phantom. This could lead to regions where the linear approximation is not valid anymore. In figure (4.16) it can be seen that this might lead to a wrong estimation of φ_n^{null} , leading to “jumps” in the scaling factor (Fig. 4.15). As already mentioned in Dowell’s paper, these problems may be overcome by using more than just 3 flip angles, which would of course lead to an extended scanning time.

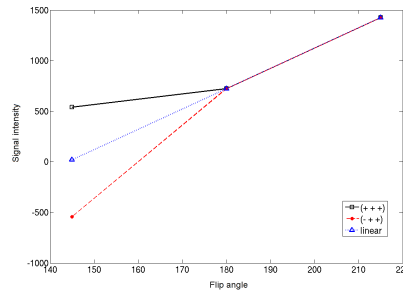


Figure 4.16: This graph shows what can happen, when the flip angle is in regions where the linear approximation is not valid anymore. The black and the red lines show the signal intensity of a certain voxel allocated to the signs (+ + +) and (- + +). The blue line shows the value that would deliver perfect linearity. For both possibilities (+ + +) and (- + +) the fit would be equally exact while the resultant φ_n^{null} would differ by more than 30° .

4.3.8 Pulsed steady-state method

Yarnikh describes a single-measurement flip angle measuring technique based upon a fast GRE sequence with identical RF pulses [Yarnikh, 2007]. Like in all the other sequences again the ratio of two observed signals is taken for the calculation of the flip angle.

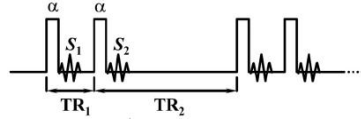


Figure 4.17: Double-delayed spoiled gradient-echo pulse sequence

The timing diagram can be seen in Fig. 4.17. The consists of two identical RF pulses with nominal flip angle φ followed by two delays TR_1 and TR_2 with $TR_1 < TR_2 < T_1$. The FID signals S_1 and S_2 are observed after the corresponding pulses in a gradient-echo form. Furthermore the sequence is ideally spoiled so that all transverse coherencies are dephased at the end of TR_1 and are then irreversibly destroyed at the end of T_2 . The ratio of the signals S_1 and S_2 in a single voxel is given by:

$$R = \frac{S_1}{S_2} = \frac{1 - \exp(-TR_1/T_1) + (1 - \exp(-TR_2/T_1)) \exp(-TR_1/T_1) \cos \varphi}{1 - \exp(-TR_2/T_1) + (1 - \exp(-TR_1/T_1)) \exp(-TR_2/T_1) \cos \varphi} \quad (4.38)$$

$$\approx \frac{1 + \frac{TR_2}{TR_1} \cos \varphi}{\frac{TR_2}{TR_1} + \cos \varphi} \quad (4.39)$$

For short TR_1 and TR_2 using the first order approximation for exponential terms, the ratio r can be used as a measure of the flip angle: $\varphi = \arccos((r \frac{TR_2}{TR_1} - 1 / \frac{TR_2}{TR_1} - r))$. At small flip angles ($< 10^\circ$) this method is said to provide a better SNR than the double flip angle method [Wade, 2007]. However, since mainly higher flip angles were of interest throughout this study, this method was not implemented.

4.4 Summary

In the first part it was shown that two of the reasons for B_1^+ field inhomogeneities in high field MR images, dielectric resonance and field focusing, become reasonably dampened at conductivities present in the human head. Instead it could be shown that the main reason for inhomogeneities in the B_1^+ field are interferences between different coil elements. In the second part and the overview of the B_1^+ mapping methods, many advantages and disadvantages of the different techniques could be observed (Table 4.1).

Method	+	-
Double angle (GRE)	one pulse per TR, therefore simple B_1^+ magnitude estimation	low SNR for low flip angles
Double angle (SE)	sensitive for small changes in homogeneous images	not suitable for flip angles $< 20^\circ$
Double angle - saturation pulse, EPI readout	better scanning time than double angle (GRE) possible	more pulses per TR than double angle (GRE)
Multi angle	best image quality; delivers information on B_1^-	scanning time
Siemens WIP sequence	scanning time	low SNR for low flip angles
Signal Null	scanning time	flip angles must be in well defined region for fitting procedure to work
Pulses steady-state	scanning time, SNR can be optimized for either high or low flip angles	valid just for a small range of flip angles

Table 4.1: Advantages and disadvantages of the different B_1^+ mapping methods

For the subsequent experiments three methods were chosen:

1. The double angle method using the gradient echo: This is basically the tank among the B_1^+ mapping sequences. It is slow but very robust and works perfectly. The only drawback of this method is the long scanning time and bad SNR for low flip angles. But for scanning of phantoms time is not a big

issue so far. The part that is most crucial for the comparisons are the parts with higher flip angles.

The big advantage of this method is the very good image quality and the simplicity of the sequence that is used. Just one pulse per repetition is very convenient for the calculations of the delivered power during a measurement. And since the source code of the sequence is available, changes of the sequence like changing the pulse used, or extending the pulse length, can be easily performed.

2. The multi angle method: Only this method also delivers information about the receive B_1^- field. For this reason it was used for coil testing and the examination of asymmetries in the receive field.
3. The B_1^+ mapping sequence from the WIP package from SIEMENS: Two reasons why this sequence was used, were the short scanning times even for multislice experiments and the good image quality that reached the quality of the double angle method. The third reason was the similarity of this B_1^+ mapping sequence with the procedure for the transmitter adjustment of the scanner. Because there are known problems with the adjustments (5.4.1) it was also in the interest of SIEMENS to test out this method. Many measurements were performed, comparing the results of this B_1^+ mapping method with the results from the scanner adjustments. The B_1^+ mapping method delivered significantly improved results for non-homogeneous phantoms, which sometimes caused big problems to the adjustments. A precise discussion of the results will be given in the Diploma thesis of Stefanie Ohrel¹⁰.

¹⁰Stephanie Ohrel, 2008, - Siemens / Erlangen

Chapter 5

Hardware

5.1 Overview

A proper examination of the imaging hardware was necessary before starting the experiments. This explanation is given in the first part of this chapter with images of all the taskcards and marks at the places, where adjustments should be made. The purpose of this explanation is to give a well explained overview of the parameters that should be adjusted when running a simple GRE sequence for the double angle method at the 7T whole body MR scanner¹.

In the second part of this chapter some problems with the scanner hardware and software are described, that appeared during the course of this thesis. Examined will be the SAR values for different coils, several adjustment methods for the reference amplitude and the calculation of the amplitude for different pulse shapes.

¹MAGNETOM 7T, Siemens Medical Solutions, Erlangen, Germany

5.2 Adjustable parameters for a simple GRE experiment

Several parameters have to be adjusted when running a gradient echo sequence used for acquiring the B_1^+ maps. The different taskcards of a standard GRE sequence are shown and the different adjustments that can be made are explained.

- **Taskcard Routine:** Figure (5.1) shows the opened taskcard “Routine”.

The screenshot displays the 'Routine' taskcard interface. It features a grid of adjustable parameters, each with a red number indicating its sequence position. The parameters include:

- 1 Slices:** A numeric input field set to 1.
- 2 Dist. factor:** A numeric input field set to 20, with a '%' symbol next to it.
- 3 Position:** A dropdown menu set to 'Isocenter'.
- 4 Orientation:** A dropdown menu set to 'Transversal'.
- 5 Phase enc. dir.:** A dropdown menu set to 'A >> P'.
- Phase oversampling:** A numeric input field set to 0, with a '%' symbol next to it.
- 6 FoV read:** A numeric input field set to 300, with 'mm' next to it.
- 7 FoV phase:** A numeric input field set to 100.0, with '%' next to it.
- 8 Slice thickness:** A numeric input field set to 5.0, with 'mm' next to it.
- 9 TR:** A numeric input field set to 4000.0, with 'ms' next to it.
- 10 TE:** A numeric input field set to 4.8, with 'ms' next to it.
- 11 Averages:** A numeric input field set to 1.
- Concatenations:** A numeric input field set to 1.
- Filter:** A dropdown menu set to 'None'.
- Coil elements:** A dropdown menu set to 'PH1-8'.
- 12 TR:** A slider bar ranging from 9.1 to 5000.0, with a green bar indicating the current value of 4000.0.

At the bottom, there is a tabbed interface with the following tabs: Program, Routine (selected), Contrast, Resolution, Geometry, System, Physio, Inline, and Sequence.

Figure 5.1: Taskcard “Routine”

1. *Number of slices:* For the gradient echo sequence, which is used for the double angle method (Section 4.3.2), each additional slice results in a longer scanning time. Therefore for comparisons of more than one slice, a sequence is recommended, where there are repeated slice selective gradients within one TR and therefore more slices excited and read out within one repetition period. The only problems that might appear in such a case are the increased SAR values due to a higher number of pulses during one TR period.
2. *Distance between the slices:* The distance factor is related to the slice thickness. For example, a slice thickness of 5 mm and a distance factor of 100% results in a gap of 5 mm between two adjacent slices.
3. *Position of the slice:* The position of the slices can either be set manually (Figure 5.2) or in this field. It is important to note that isocenter is just the center of the magnet but not necessarily the center of the coil, which is

5.2. ADJUSTABLE PARAMETERS FOR A SIMPLE GRE EXPERIMENT 87

usually preferred for comparison with the simulations. Methods for exactly determining the center of the coil are described in chapter (6.3.1)

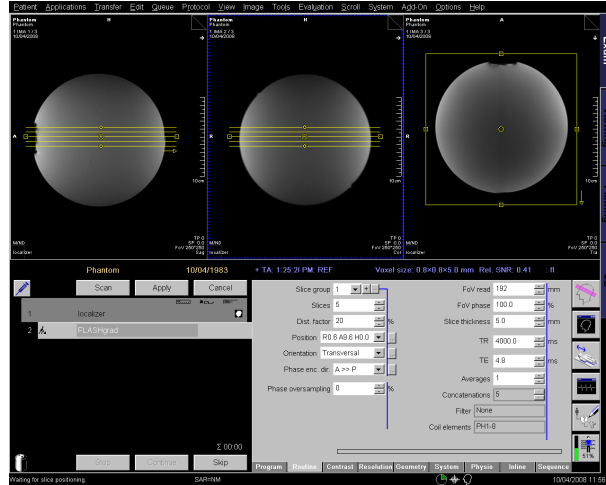


Figure 5.2: Positioning the slices

4. *Orientation of the slice*: The orientation can either be transversal, coronal or sagittal.

When the patient or the phantom is registered as “head first-supine”, which is usually the case, the corresponding planes from the simulations are shown in table 5.1.

Scanner	Simulations
transversal	z-plane
coronal	y-plane
sagittal	x-plane

Table 5.1: The orientation of the slices in the scanner and the corresponding slices in the simulations

When the patient is registered for some different position, the corresponding planes change!

5. *Phase encoding direction*: As the name already proposes, this field shows the direction of the phase encoding gradient. When the slice should not be quadratic this direction should be chosen along the shorter edge.

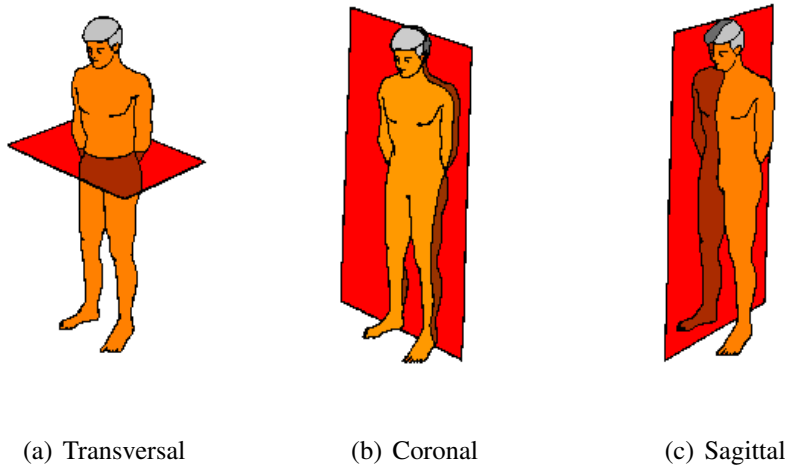


Figure 5.3: The 3 different imaging planes [Hornak, <http://www.cis.rit.edu/htbooks/mri/>]

Then in field 7 the field of view in the phase encoding direction can be decreased in order to shorten the scanning time.

6. *Field of view (FOV)*: The FOV is lowered by applying a steeper read-out gradient without changing the size of the Matrix. The FOV should be chosen such that along the phase encoding direction the whole phantom fits inside. If this is not the case, wrap-around might occur which means that voxels that are outside the FOV have the same spatial encoding as some voxels inside the FOV (Figure 5.4).

Explanation for Wrap-around: A voxel inside the FOV possesses a phase between $-\pi$ and $+\pi$. A voxel outside the FOV along the direction of the phase encoding gradient now might receive a phase higher than $+\pi$ like $+\pi + x$ with $0 < x < 2\pi$. For the spatial encoding this gives the same position as given by $+\pi + x - 2\pi = -\pi + x$ which would then lie within the FOV. Voxels outside the FOV are therefore overlapped onto voxels inside the FOV.

7. *Field of view in the phase encoding direction*: Please notice point 5.

8. *Slice thickness*: The slice thickness is determined by adjusting the slope of the slice selection gradient. A steeper gradient gives a thinner slice. A thinner slice gives a better resolution in z-direction, while a thicker slice

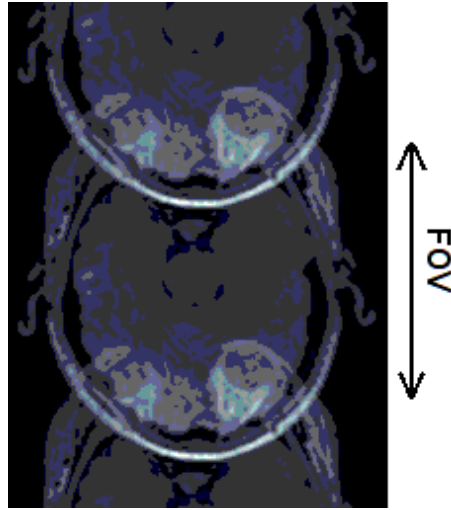


Figure 5.4: When the FOV in phase encoding direction is smaller than the object, the parts that are outside the FOV are folded back into the image.

provides a stronger signal because the voxels are bigger and therefore more spins can induce a current in the receiver coil.

9. *Repetition time TR* : This is the time in ms that exists between successive pulse sequences applied to the same slice. It is the time between the first RF pulse of the sequence and the first repetition of the same RF pulse after a certain period. The repetition time for the B_1^+ mapping experiments was chosen such that $TR > 5 \cdot T_1$. This ensures that the magnetization can always completely relax before each new pulse (Section 4.3.2) [Stollberger & Wach, 1996].

10. *Echo time TE* : TE represents the time in ms between the application of the excitation pulse and the peak of the echo signal in Spin Echo and Inversion Recovery pulse sequences. Since no T_2 weighting was intended, the echo time was set to the minimum value to get the maximum signal.

11. *Averages*: Taking N averages improves the SNR of the image by \sqrt{N} but at the same time extends the measurement time by a factor of the number of averages taken. Some experiments with the Sugarphantom in the Rapid coil showed no big improvement to the B_1^+ maps by taking more averages (Fig. 4.7). On the other hand more averages especially during the 3D scan for acquiring the voxel data of the phantom are necessary to ensure

good enough SNR, especially for parts with low signal intensity (Section 6.3.1).

12. *Possible values:* The possible values together with their respective minimum and maximum values can be seen at this bar. E.g. in the current picture a minimum repetition time of $TR = 9.1ms$ and a maximum of $TR = 5000ms$ can be chosen. The current repetition time selected is $TR = 4000ms$.

- **Taskcard Contrast:** Figure (5.5) shows the opened taskcard “Contrast”.

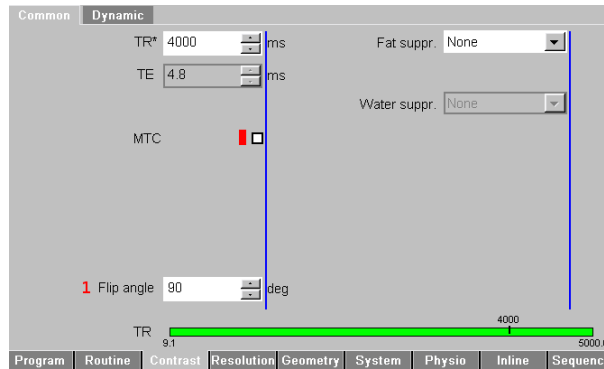


Figure 5.5: Taskcard “Contrast”

1. *Flip angle:* The flip angle shows the nominal flip angle (Section 4.3.1) of the sequence. According to this value, the amplitude of the pulse for the sequence is calculated. Some experiments have shown that this recalculation from the reference amplitude to the amplitude for the particular pulse does not always work correctly. While there were no problems for rectangular pulses, selective pulses delivered actual flip angles which were about 15% too low (Section 5.4.2).

- **Taskcard Resolution:** Figure (5.6) shows the opened taskcard “Resolution”.

1. *Base resolution:* For a better resolution a steeper read out gradient is needed. A worse resolution means a bigger voxel size and therefore more

5.2. ADJUSTABLE PARAMETERS FOR A SIMPLE GRE EXPERIMENT 91

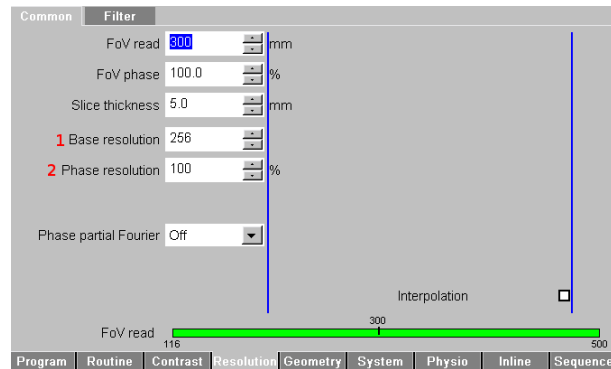


Figure 5.6: Taskcard “Resolution”

signal per voxel.

2. *Phase resolution*: This is the resolution in the phase encoding direction. For the B_1^+ mapping experiments where time did not play a major role, always 100% was used to get the same resolution in the phase encoding direction.

- **Taskcard Geometry**: Figure (5.7) shows the opened taskcard “Geometry”.

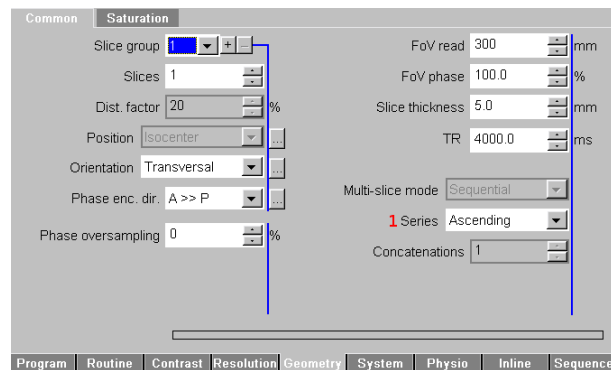


Figure 5.7: Taskcard “Geometry”

1. *Series*: The series can be either Ascending, Descending or Interleaved. This means the order in which the slices are scanned. It does NOT mean the numbering of the images. So for example if several transversal slices with the patient in position “head first-supine” are scanned, the numbering

always goes from $F \gg H$, that is from feet to head.

- **Taskcard System - Transmitter/Receiver:** Figure (5.8) shows the opened taskcard “System - Transmitter/Receiver”.

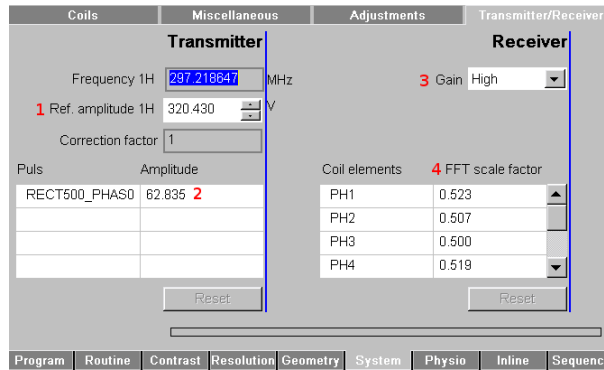


Figure 5.8: Taskcard “System, Transmitter/Receiver”

1. *Reference amplitude:* This is the reference amplitude for this phantom or patient in the current position. There are several ways to adjust the reference amplitude (Section 5.2). If the reference amplitude has to be changed for a measurement, it should not be done here, because then it shows for future measurements the value $Ref.Amp. = 0V$ in this particular field. Instead it should rather be done under the $[Options > Adjustments]$ menu.

Reference Amplitude

In the protocols of the SIEMENS pulse sequences, the value of the reference amplitude refers to the voltage that is needed for sending a rectangular pulse with pulse length $\tau = 1 ms$ that will rotate the magnetization of a slice with thickness $d = 1 cm$ in the isocenter of the magnet by 180° (Section 5.2). The B_1^+ field of this pulse will be called $B_{1,180}^+$. If now the flip angle setting in the protocol is changed to a certain value, e.g. 90° , the actual amplitude of the pulse will also be changed to the desired value. For a rectangular pulse with pulse length $\tau = 1 ms$, the B_1^+ field would then just

5.2. ADJUSTABLE PARAMETERS FOR A SIMPLE GRE EXPERIMENT 93

have to be $\frac{1}{2}B_{1,180}^+$ because of (4.14) and accordingly the required voltage would be just half of the reference voltage (Fig. 5.9).

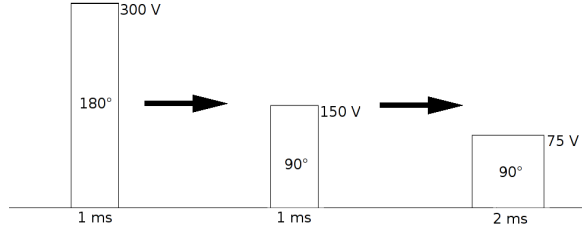


Figure 5.9: Recalculation of the reference amplitude to 90° pulses with similar and different pulse lengths

Note: Due to the following relation between power P , voltage U and resistance R

$$P = \frac{U^2}{R} \quad (5.1)$$

the power required for a 90° pulse would be not half the value for a 180° pulse but just one quarter of this value!

For other pulse shapes the amplitude would be adjusted according to the shape (Section 5.4.2).

2. *Pulse:* The name of the pulse and its amplitude: There are several ways to get information about the pulse shape from the name of the pulse (Section 6.4.2). When the source code of the sequence is available, the sequence can be opened and then simulated with IDEA². In the field RF-signal data of the simulation tool, the pulse shape can be viewed and fitted with MatLab. The other possibility is to open the pulsetool in IDEA and view the pulse there if it is available. Unfortunately the information concerning the pulse is very limited. It is very difficult to get the exact mathematical description of the pulse, because only SIEMENS has access to this information. The amplitude shown is the maximum amplitude of the pulse.

3. *Receiver gain:* The receiver gain can be chosen to be either low or high.

²Integrated Development Environment for Applications; Siemens tool for programming pulse sequences

There might be cases, where the signal of the imagined object is so high, that the signal level is larger than the maximum input. That means that above a certain threshold the receiver just experiences a maximum signal but can't differentiate anymore between the different values of the very high signal. This problem is called clipping and results in parts of the image just having the maximum value.

4. *Fast Fourier Transform (FFT) scale factor*: The FFT scale factor is the factor that is multiplied with the amplitude of the signal, to extend the range of values for the signal to the maximum range that is possible. In our case the maximum range for a 12-bit dicom-image would be the range from 0 to 4095³. For a multichannel coil each channel has it's own FFT scale factor. The ratio between the FFT scale factors for each channel should be kept constant. The FFT scale factor has to be lowered in some cases when, due to the multiplication with the factors, the values of the signal amplitude exceed the maximum of the possible range. This can easily happen when e.g. imaging a water phantom with low conductivity, which show a very bright center. Because the FFT scale factors are coil specific, they are reset after every scan. And since changing the values of each channel by a certain factor before each new scan is very cumbersome, it is recommended to rather implement some image factor into the protocol that rescales each channel by a constant factor.

5.3 Performance comparison between coils

There is a big difference between the *Power-to-SAR-conversion-factor* provided by Siemens of the 8-channel coil from *Rapid* and the circular polarized (CP) coil from *Invivo*. The Power-to-SAR-conversion-factor⁴ for the Rapid coil is “2 kg⁻¹” while for the Invivo coil is just “0,93”. This has a major influence on the

³So far the FFT factors are not optimized for all the sequences, which results in the values ranging very often just from 0 to a maximum value of less than 1000.

⁴Coil-specific value for the recalculation from input power to local SAR value. The higher this value, the higher the SAR value for a certain input power.

performance of the coils for experiments, which are restricted due to high SAR values. The effect of this can be seen on the following experiment:

Experiment: For each coil the orange silicon oil phantom was placed in the coil center and a Turboflash⁵ sequence with 192 slices, selective pulse with pulse amplitude=174,872 V and $TR = 1030\text{ ms}$ was applied. The extent to which the SAR limit and the TR time would need to be exceeded in order to reach a SAR value of 100% is compared in table 5.2.

	SAR value	recommended TR
Rapid coil	333%	3460 ms
Invivo coil	148%	1540 ms
↓		
SAR(Rapid) : SAR(Invivo) 2,09 : 0,93		

Table 5.2: Comparison of the SAR values for the Invivo and the Rapid coil

It can be seen that there is quite a difference between the SAR values for the two coils and that the same experiment would need a much shorter scanning time if run with the Invivo coil. But the result that could be expected from the Power-to-SAR-conversion values would be a ratio of 2 : 0,93. Therefore there must be some other factors that also influence the different Siemens SAR estimation of the coils.

5.3.1 Input power - flip angle

Additional to the difference in the SAR values, there might be a difference in the delivered flip angle according to the input power for both coils.

Question: The question that arose was: Do both coils for the same input power produce the same flip angle in a certain sample?

Experiment: For each coil the orange silicon oil phantom was placed in the coil center and then a flip angle map with the standard two angle method was taken. The reference amplitude was set manually to make sure that the experiments with both coils were run with exactly the same pulse amplitude. The reference am-

⁵Turbo Fast Low Angle Shot - Gradient echo sequence with 180° preparation pulse [Atkinson, Burstein, & Edelmann, 1990].

plitude throughout the whole experiment was 320 V. The nominal flip angle was $\varphi_n = 60^\circ$, $TR = 5000\text{ ms}$ and $TE = 4,8\text{ ms}$ and the a selective pulse was used. Figure (5.10) shows the transversal slices through the phantom and figure (5.11) the corresponding profiles.

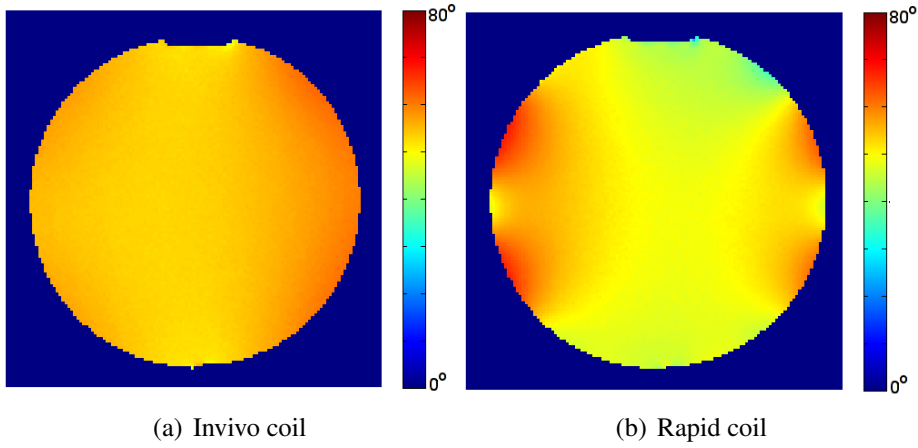


Figure 5.10: Flip angle maps of the orange oil phantom taken with the Invivo and the Rapid coil

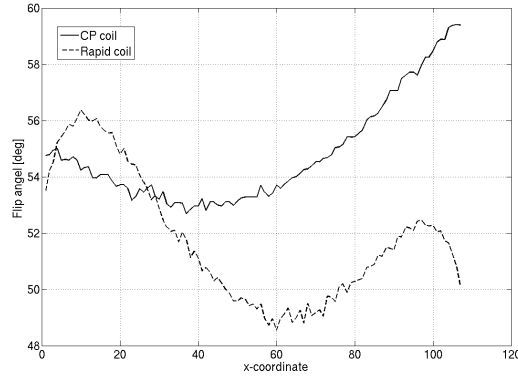


Figure 5.11: Profiles of the flip angle maps from Invivo coil and Rapid coil. The profiles are along the x-direction with y- and z-coordinates being in the coil centers.

The mean flip angle over the whole transversal slice for both coils can be seen in Table 5.3.

The result shows that the Invivo coil delivers, for the same power input, a higher

	mean flip angle
Rapid coil	51, 8°
Invivo coil	55, 4°

Table 5.3: The mean flip angles for the transversal slice through the coil center of Invivo and Rapid coil

flip angle of approximately 7% than the Rapid coil. This means that the Invivo coil delivers not just lower SAR values than the Rapid coil due to its lower Power-to-SAR-conversion-factor. It also produces higher flip angles for the same input power. This underlines the known advantage of the Invivo coil for SAR-intensive sequences, which need much higher constraints when run with the Rapid coil than when run with the Invivo coil.

5.4 Scanner adjustments and pulse shape

Problem: During many B_1^+ mapping experiments even for phantoms with a very homogeneous B_1^+ field such as the orange oil phantom a significant difference between the nominal flip angle and the actual flip angle could be observed. This suggests that either the transmitter adjustments of the scanner are not working perfectly or the recalculation from the amplitude acquired with the adjustments to the amplitude of the actual pulse is not correct in all cases. Firstly, the adjustments were examined. To avoid misunderstandings three different kinds of transmitter adjustments are used:

1. The *automatic adjustment*: This is performed without personal intervention right before starting the first measurement.
2. The *manual adjustment*: With the sequence protocol opened, the transmitter adjustments are done manually under the [controls] task bar. For this purpose a starting voltage is applied, and starting from that voltage numerous iterations are performed, that finally converge to a certain value.
3. The *experimental adjustment*: A gradient echo sequence with 90° nominal flip angle is run for several reference amplitudes. The volume of interest

within the phantom that was considered for the evaluation was a transversal slice with thickness 1 cm around the isocenter of the scanner. This is the same region that is according to Siemens used for the other adjustment methods. The reference amplitude which delivers the maximum signal for this region is then taken as the correct reference amplitude for the experiments. A TR with $TR > 5T_1$ was taken to ensure the full relaxation of the magnetization before each new pulse.

The first two adjustment methods are built-in features of the scanner. A modification of them can just be performed by Siemens. The third method, the *experimental adjustment*, was designed by myself and can be modified by e.g. changing the pulse shape of the GRE sequence. This method will be applied first with a rectangular pulse (section 5.4.1) and second with a selective pulse (section 5.4.2). If the pulse recalculation works correctly both pulse shapes should deliver the same results!

5.4.1 Comparison between the different adjustment methods

Experiments: The experiments were performed with the Invivo coil. The orange oil phantom was placed in the coil center.

1. For the *automatic adjustment*, a gradient echo sequence was started, and the reference amplitude was taken, that was shown in the protocol.
2. Next, with the opened protocol and 5 different starting values ranging from 100 V to 300 V , the *manual adjustment* was performed several times.
3. Finally, for the *experimental adjustment* a gradient echo sequence with 90° nominal flip angle, $TE = 4,8\text{ ms}$ and a $TR = 4000\text{ ms}$ to prevent saturation effects was run for different reference amplitudes between 150 V and 400 V . The mean signal over the whole phantom was taken and the data pairs of the different reference amplitudes with the corresponding mean signal were fitted with MatLab to a sinus function⁶. With the help of this

⁶In section (4.3.2) it is shown that the signal intensity for a GRE sequence is proportional to the sinus of the flip angle

curve the reference amplitude for the maximum signal, in other words the real 90° flip angle was determined.

Results:

1. The *automatic adjustment* delivered a reference amplitude of $299,5\text{ V}$.
2. The *manual adjustment* gave the results shown in table 5.4.

Starting value	Final value
294 V	298,7 V
180 V	299,1 V
160 V	298,8 V
100 V	298,6 V
300 V	298,5 V
mean value	298,7 V

Table 5.4: Results of the manual adjustment for different starting values

3. The *experimental adjustment* for a sequence with rectangular pulses delivered 5 data pairs of reference amplitude and corresponding signal for a 90° pulse. Taking the mean value of the signal over the whole phantom, the graph that can be seen in Fig.(5.12) could be obtained. The data pairs were fitted and delivered the following function:

$$Signal = 1105 \cdot \sin(0,005388 \cdot Refamp + 12.53). \quad (5.2)$$

The maximum of the signal could be found for a reference amplitude of $300\text{ V} \pm 5\text{ V}$, which is less than 2% difference to the value acquired by the automatic adjustment.

5.4.2 Validity of adjustment and pulse shape

Some experiments with a slice selective pulse shape showed significant discrepancies between the nominal and the actual flip angle, even when the flip angle distribution over the phantom was very homogeneous as for the transversal slice of

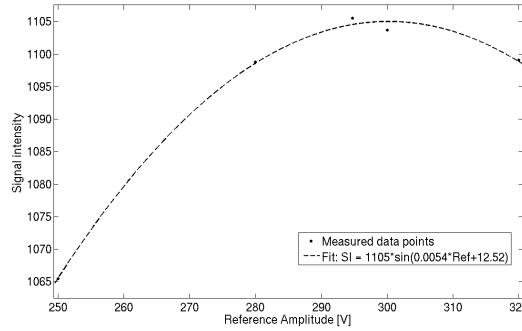


Figure 5.12: Relation between the mean signal of the whole phantom using a GRE sequence with rectangular pulse shape and the reference amplitude

an oil phantom. Since the experimental adjustments before were performed with a rectangular pulse shape, there is the possibility that this big discrepancy has to do with the pulse shape of the sequence used for the B_1^+ mapping experiment. It must be examined whether the recalculation from the reference amplitude for a 180° pulse to the amplitude of the particular pulse of the sequence is working correctly.

Experiment: The orange phantom was placed in the coil center of the *Rapid* coil. Two flip angle maps were acquired using the double angle method and nominal flip angles of 60° and 120° . For the first map a rectangular pulse was used, for the second map a slice selective pulse was used. The acquired maps can be seen in Figure (5.13).

From the flip angle maps the mean flip angle over the whole phantom and the flip angle at the center of the phantom were determined (Table 5.5).

Pulse shape	Mean flip angle	Flip angle at center
slice selective	52, 1°	52, 1°
rectangular	59, 6°	57, 5°

Table 5.5: The difference in flip angle for different pulse shapes

The difference in the results suggested a strong influence of the pulse shape on the actual flip angle. To further test this connection, another *experimental adjust-*

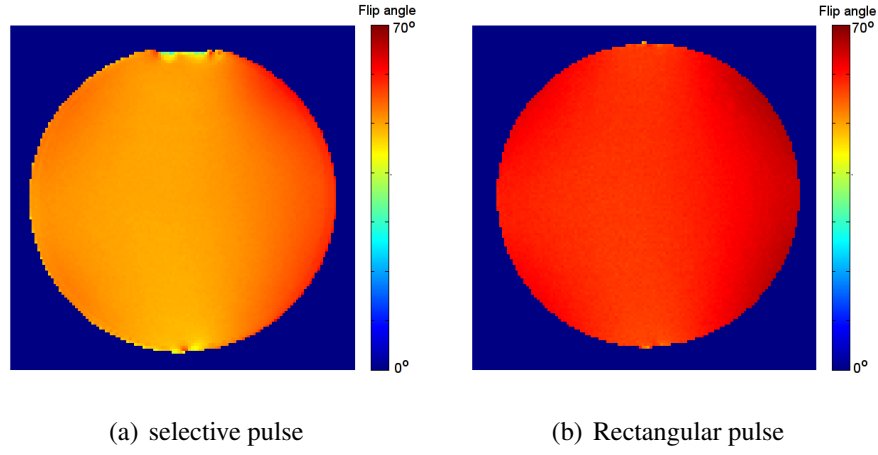


Figure 5.13: Flip angle maps of the orange oil phantom in the Invivo coil using different pulse shapes

ment with a slice selective pulse shape for 13 different reference amplitudes was performed. The fitting function can be described by:

$$Signal = 3709 \cdot \sin(0,004347 \cdot Refamp + 0,04729). \quad (5.3)$$

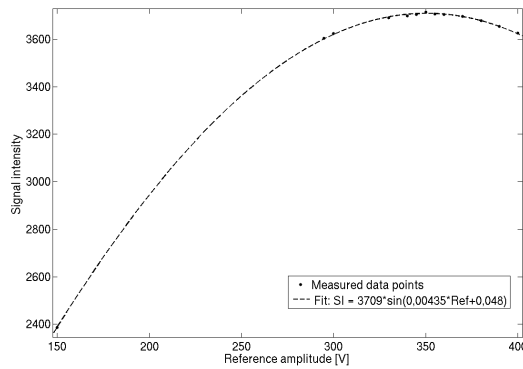


Figure 5.14: Relation between the mean signal of the whole phantom using a GRE sequence with selective pulse shape and the reference amplitude

The maximum of the signal could be found for a reference amplitude of $351 \text{ V} \pm 2 \text{ V}$.

5.5 Summary

The SAR comparison of the coils validated that there is a much lower SAR value for sequences run with the Invivo coil due to the smaller “Power-to-SAR-conversion factor” of the Invivo coil. At the same time, the Invivo coil delivered for the same reference amplitude an approximately 6% higher flip angle than the Rapid coil.

These points might be in some cases a big advantage of the Invivo coil. While the Rapid coil delivers a better SNR than the Invivo coil, the lower SAR makes the Invivo coil very valuable for SAR intensive sequences, which contain many strong pulses within a short time.

The investigation of the adjustment types and different flip angles delivered a strong variation in the results for different pulse shapes.

Adjustment type	Reference amplitude
Automatic adjustment	300 V
Manual adjustment	299 V
Experimental adjustment rectangular	300 V
Experimental adjustment selective	351 V

Table 5.6: The reference amplitude estimated with different adjustment methods for the orange oil phantom in the Invivo coil

For the orange oil phantom in the Invivo coil the following findings occurred. From the values shown in Table 5.6, it can be seen that built-in adjustment methods and the experimental adjustment using a rectangular pulse delivered the same result. This suggests that the recalculation from the reference pulse to the amplitude of the pulse used in the sequence works correctly, if the pulse of the imaging sequences also possesses a rectangular shape. If the recalculation to different pulse shapes is correct, all the different adjustment methods should deliver the same results. But during the experiments, flip angle maps acquired with a sequence with a slice selective pulse shape demanded an approximately 15% higher reference amplitude to achieve good agreement between the actual and the nominal flip angle. At the same time, it could be observed that while the difference

between nominal and actual flip angle for a rectangular pulse in a very homogeneous phantom was less than 1%, for pulses with a slice selective pulse shape the deviation of the actual flip angle from the nominal flip angle is over 13%. These results very strongly indicate that the recalculation from the rectangular pulse shape of the reference amplitude to a non-rectangular pulse shape is erroneous.

Chapter 6

B_1^+ field comparison

6.1 Overview

In the beginning of this chapter an overview of the simulation programs used is given. A short investigation is done to check the cause of some asymmetries that can be observed in the B_1^+ profiles.

In the middle sections, the comparison procedure between experimental and simulation data is described. The first step is the conversion of the MRI data into a format that can be used by the simulation programs. Subsequently, the software is described for the comparison of the processed simulation data and the experimental results.

For comparison of the magnitude of the B_1^+ field some knowledge about the pulses and the measurement setup is necessary. Therefore, an explanation of the comparison procedure of the magnitude values is given separately.

In the last part of the chapter, the comparison of the B_1^+ distribution and the B_1^+ field magnitude between simulation and experiment for several phantoms is presented. The comparisons are performed with various types of phantoms depending on the purpose of acquiring the B_1^+ map.

In the early stages of this work, the major problem with the simulations was the missing or incorrect geometrical and electrical data provided by the vendor for the imaging coils. Therefore, initial simulations delivered quite different results

from the experimental data (Fig. 6.3). For these reasons, the first experiments were performed with simple, symmetric phantoms such as the spherical oil phantom or bottles filled with various substances (Table 3.3). B_1^+ measurements with such simple phantoms were used to validate the simulations by providing general information about the field profile. After getting sufficient knowledge about the coil, the water based Siemens phantom 5512 608 K2205 (Table 3.3) was used¹ to retune the coil in the simulations in order to improve the agreement² between magnitude of the B_1^+ field in simulations and experiment (Fig. 6.1).

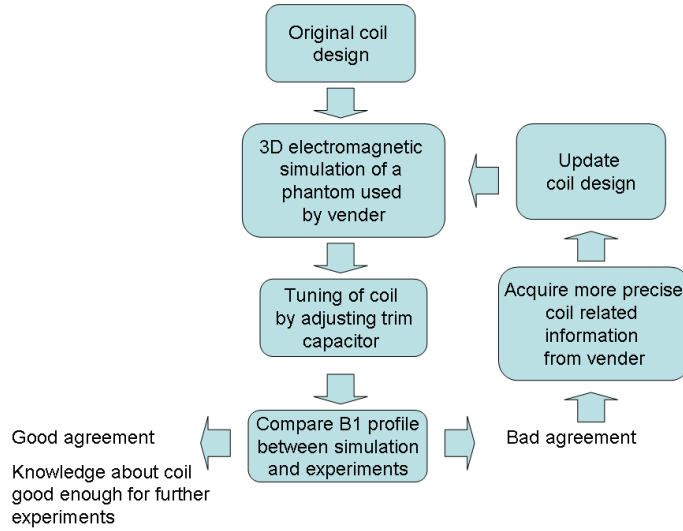


Figure 6.1: Procedure of using simple phantoms for verification of the coil design.

With the validated information about the simulated coils it was possible to check information about various phantoms. After construction of the phantom, the B_1^+ profile can be compared with the simulation data. If the comparison delivers a good match between experiment and simulation, the information concerning the phantom that was delivered to the simulations can be considered to be correct. This can help verifying the electrical properties of the phantom, the positioning

¹As it was done by the vender Rapid. The information about the coil from Invivo was not sufficient for exact comparisons.

²Up to now the simulation setup does not include second order effects like variation of the capacitor values in the real coil that could be the reason for some observed B_1^+ field asymmetries of the coils.

inside the coil as well as information about the mass of different phantom parts which can be derived from the voxel data if the mass density is known (Fig. 6.2).

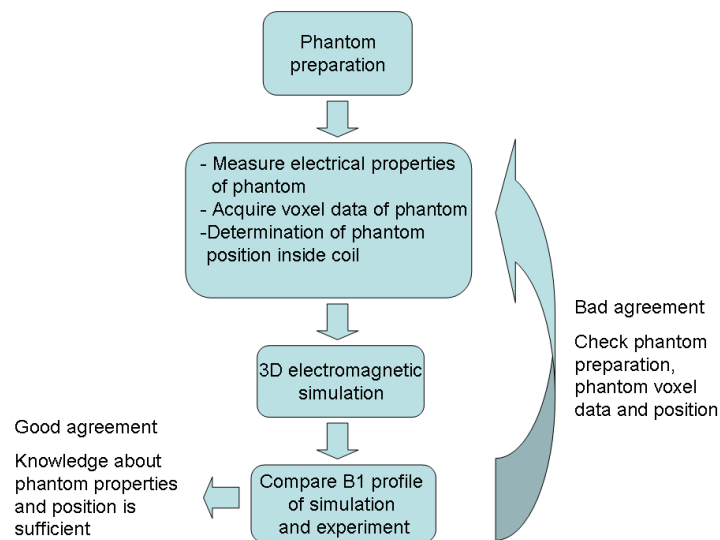


Figure 6.2: The procedure how 3D electromagnetic simulations can be used for acquiring knowledge about more sophisticated phantoms.

6.2 Simulations

The simulations were conducted by Dr. Mikhail Kozlov³ and the results made available for the comparison procedure. As simulations and experiments did not match right from the beginning, the parameters of the coils in the simulations had to be adjusted until a satisfying agreement between simulation data and experimental data could be observed.

³Max Planck Institute for human cognitive and brain sciences, Leipzig

6.2.1 Simulation programs

The simulations were performed with two different simulation programs, the *High frequency structure simulator*⁴ (HFSS) and the *CST Studio Suite 2008*⁵

HFSS This program is solving the Maxwell equations numerically in the frequency domain by using the finite element method. First the boundary conditions of the given structure including the power of the given RF source or parameters of the coil and the tissue need to be configured. Then, during the calculation process the given space is divided into a mesh grid consisting of tetrahedrons of varying size. Within these small tetrahedrons, the Maxwell equations are solved using the finite element method.

It was just possible to compare analytical objects like sets of spheres or cylinders with HFSS because no tool for converting the 3D MRI data to the format necessary for HFSS was available so far. Therefore, objects such as bottles or spherical phantoms were approximated by cylinders with the same length or radius, or spheres with the same radius as the phantom.

CST The CST microwave studio uses the finite-difference time-domain (FDTD) method to solve the behaviour of an electromagnetic field. The time dependent Maxwell's equations are discretized into finite-difference equations. With the resulting equations, the electric field component and the magnetic field component are solved alternately at a given instant in time. This process is repeated until the electromagnetic field behaviour is fully evolved. In CST, the simulation space is divided into a hexahedral mesh with the electromagnetic field behaviour being evaluated for every single mesh cell. For the CST simulations it was also possible to compare objects with an arbitrary voxel shape such as the skull phantom (Fig. 6.33). For this reason, the 3D MRI data had to be converted and then imported into the simulation program (6.3.1).

⁴HFSS, Ansoft Corp., Pittsburgh, USA

⁵Computer Simulation Technologie, Darmstadt, Germany

6.2.2 Reasons for asymmetries

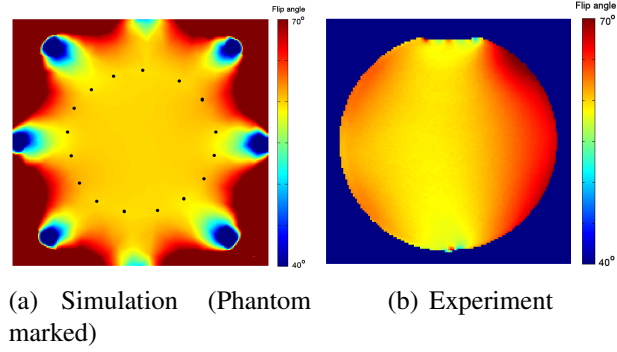
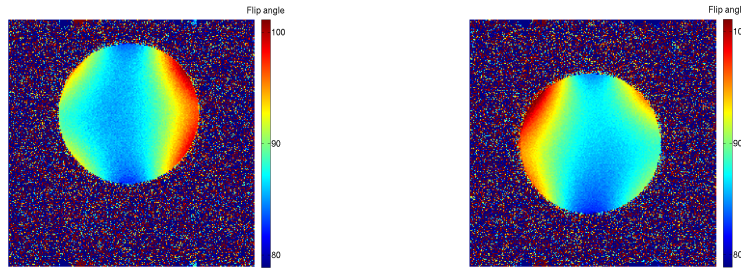


Figure 6.3: A B_1^+ map of the orange oil phantom in the Invivo coil. The simulation shows almost no asymmetry, while an increase of the B_1^+ field towards the right can be observed in the experiment.

In Fig. (6.3) a B_1^+ map of the orange oil phantoms in the Invivo coil can be seen. There are asymmetries visible in the experimental data that are not visible in the simulation data. Several experiments were conducted to exclude the possibility that these asymmetries resulted either from the phantom or from the scanner. The experiments described below were performed with the Invivo coil.

Experiments:

1. Since the orange oil phantom is not a perfect sphere but has some small asymmetric parts like the lid, the influence of the phantom shape on the B_1^+ map was examined. For this purpose the phantom was turned around and the same scan was repeated. The resulting image again showed the increase in magnitude of the B_1^+ field towards one side. Therefore the asymmetry of the B_1^+ field due to some asymmetries in the phantom could be excluded.
2. The static magnetic field in the scanner might have inhomogeneities, which influence the B_1^+ map. To examine this possibility, the coil was turned upside down. In the resultant B_1^+ map, the increase in magnitude now went to the opposite site (Fig. 6.4). The asymmetry therefore had to be due to the coils.



(a) Coil in normal position

(b) Coil turned upside down

Figure 6.4: Inhomogeneity of the B_1^+ field for different coil positions

6.3 Comparison procedure

An overview of the comparison procedure using CST can be seen in Fig.(6.5) and for HFSS in Fig.(6.6). The exact description to the particular steps are given in sections (6.3.1) and (6.3.2).

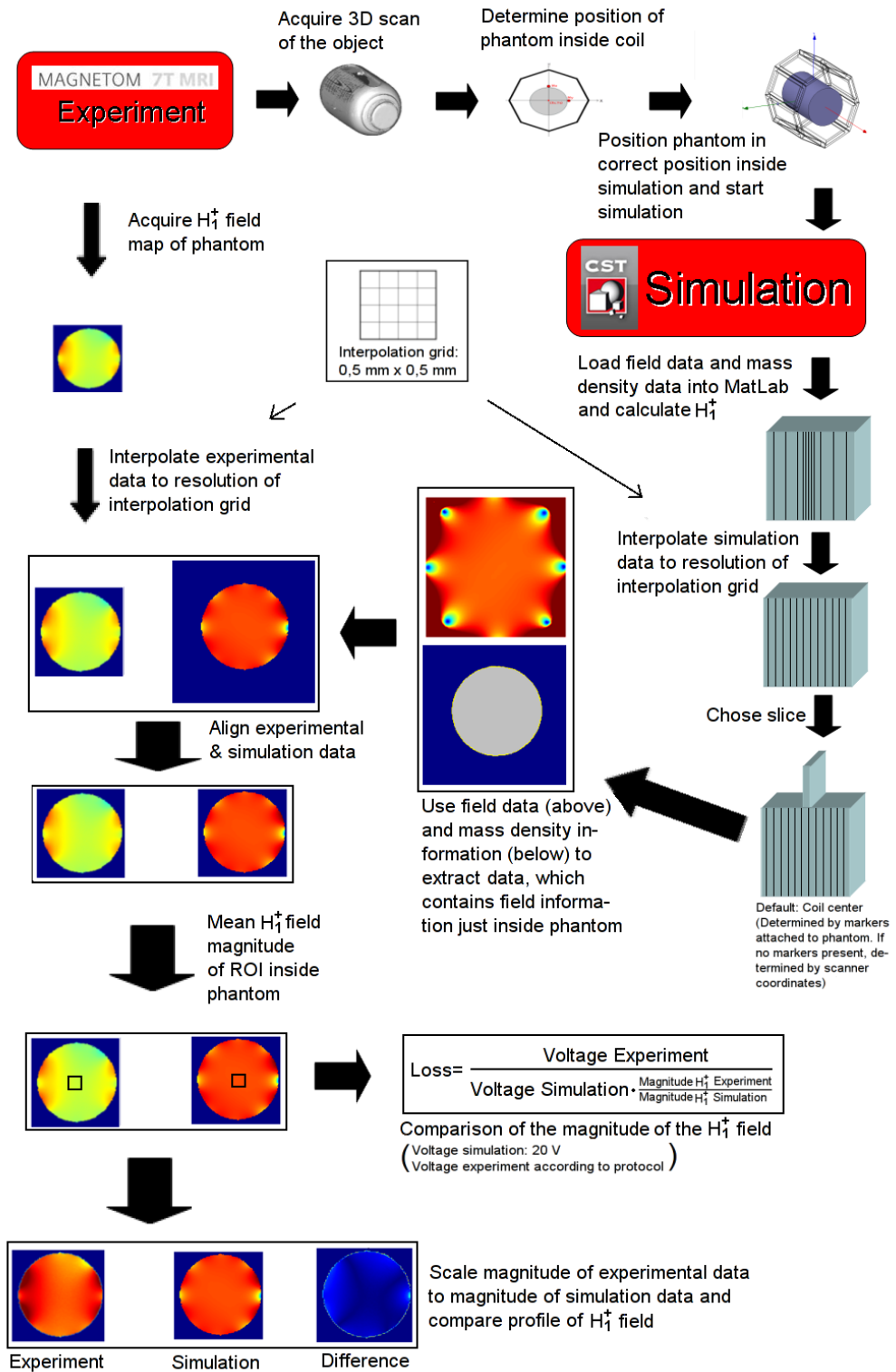
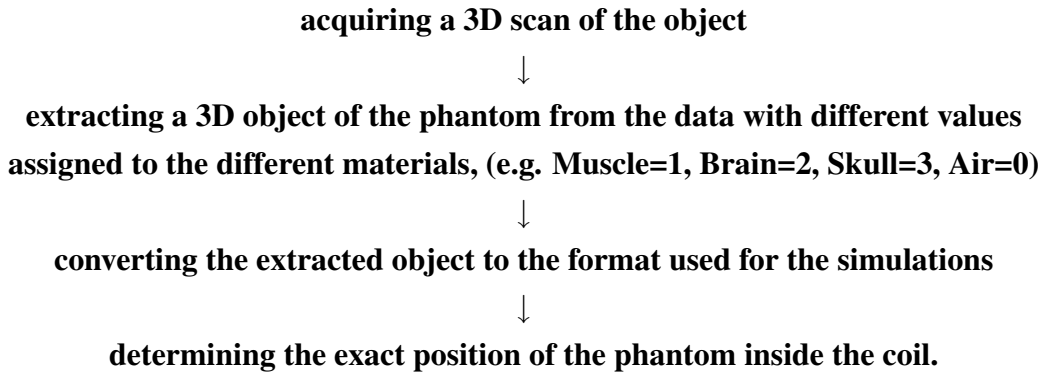


Figure 6.5: Schematic representation of the comparison procedure with CST.

6.3.1 Acquiring a 3D object and the position of the phantom

For these simulations the position and the shape of the phantom have to be known. This is achieved by:



This procedure is so far just done for the CST simulation program. For HFSS, analytical objects such as cylinders and spheres are used for the approximation of the real phantoms.

- *Acquiring a 3D scan of the object:* When acquiring a 3D scan of the object, it has to be made sure that all the voxels within the object have a signal intensity above a certain threshold. Otherwise the final 3D object will have parts from the object “cut off” or noise around the object which then cannot be differentiated from the phantom by the simulation program. In the following paragraph a sequence is described which was used for acquiring a 3D scan of a skull phantom.

Imaging sequence for acquiring 3D object of skull filled with gel A Turboflash-sequence was used with $TR = 3540\text{ ms}$, $TE = 2,24\text{ ms}$, Pixel Bandwidth = 300 Hz, receiver gain *high*, *Averages* = 1 and a pulse amplitude of 180 V. It was necessary to increase the SAR limit by decreasing the “Power-to-SAR-conversion factor“ to 1 in order to be able to apply such a strong pulse to ensure a sufficient high signal in every voxel within the phantom.

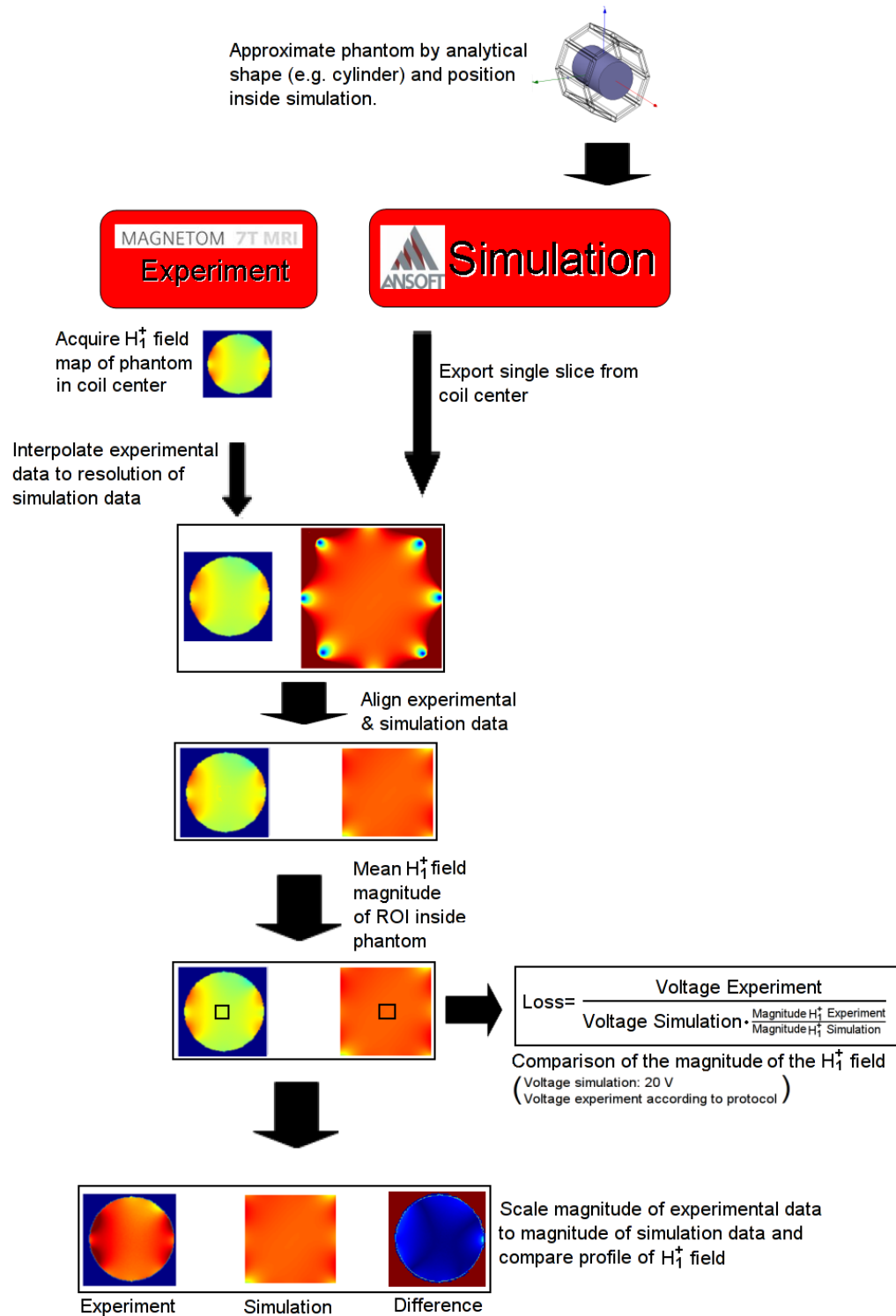


Figure 6.6: Schematic representation of the comparison procedure with HFSS.

- *Extracting a 3D object of the phantom containing information about the different materials:* When the phantom consists of more than one material, a segmentation has to be performed to differentiate between the different materials within the phantom. The main problem for this procedure are the inhomogeneities of the signal intensity within the 3D object (Fig. 6.7), also called the *bias field*.

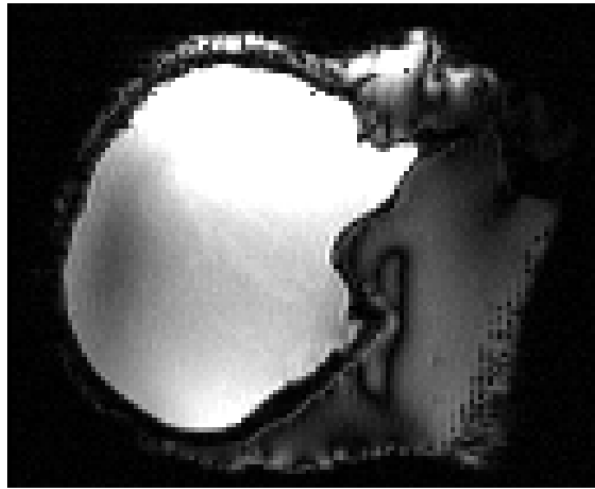


Figure 6.7: A T_1 weighted image of a headphantom. Due to the inhomogeneity in the signal intensity of the image, the so called bias field, parts with different T_1 times share the same signal intensity values.

In this work, the segmentation was performed manually with MatLab. Depending on the individual case, the segmentation was completed by either distinguishing the different materials by the signal gaps that existed between them or by setting different thresholds for materials with distinct signal intensity values.

Problems and possible solutions:

- The problem with the bias field in the phantom might be overcome by implementing a bias field correction algorithm which removes the inhomogeneities within the object. An algorithm for the bias field correction of a 3D object is currently being written by Thomas Rein-

hardt⁶.

- Materials such as the plastic skull which provide no signal are hard to distinguish from other parts without a signal such as air spaces. For a head phantom without any cavities, it is still possible to differentiate between the region inside the phantom and outside the phantom provided there is a thick enough layer of material completely covering the skull. For a head phantom with cavities simulating e.g. the sinuses, this is no longer possible. In such a case an x-ray scan of the phantom and later co-registration with the MRI data could make the distinction simpler to detect.
- *Converting the extracted object to the voxel format:* After the segmentation, the dimensions of the data, a 3D matrix containing information about the phantom, have to be transformed into the correct order suitable for the simulation program. For this purpose the script `Permutebox.m`, given in the appendix (Appendix .1) has to be run.
- *Finding the position of the phantom inside the coil:* For placing the phantom into the coil inside the simulation, the correct position of the phantom relative to the coil has to be determined.
The position of the slice is always given by three values $R \leftrightarrow L(x - direction)$, $A \leftrightarrow P(y - direction)$ and $H \leftrightarrow F(z - direction)$. E.g. for a value of $R = 0$, $A = 0$ and $H = 0$ the center of the slice and the isocenter of the magnet would coincide. Unfortunately, for the simulation not the position relative to the magnet but relative to the coil is important. For this reason the translation vector from the isocenter of the magnet to the center of the coil has to be found. The x- and z-direction of the coil can be aligned to the isocenter of the magnet with the help of the cross-hair of the scanner's built-in laser at the magnet opening. The only problem is the determination of the y-position of the coil center. For this purpose small

⁶Max Planck Institute for human cognitive and brain sciences, Leipzig

markers were attached to the phantom⁷ (Figure 6.8).

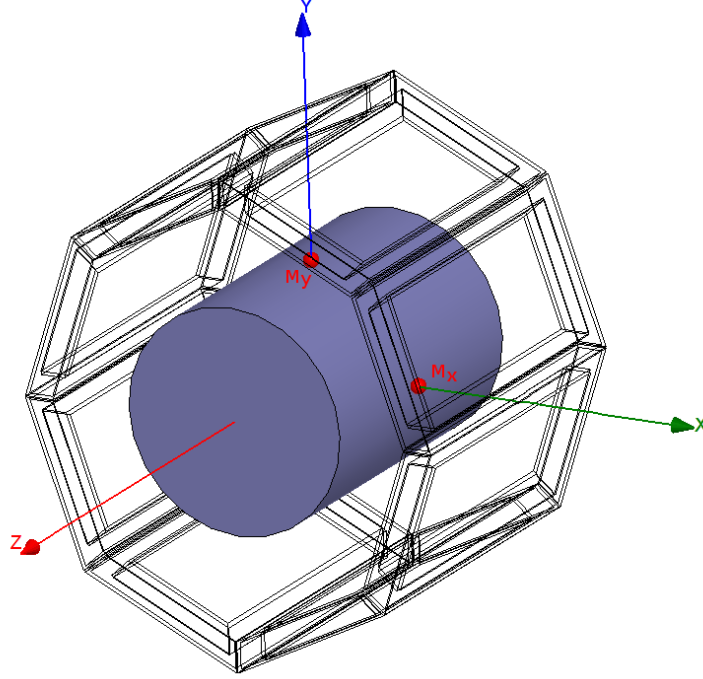


Figure 6.8: Rapid coil with Phantom inside and markers M_x and M_y attached to the phantom. The coordinate system originates from the center of the coil which does not necessarily coincide with the center of the phantom

The first marker M_y was placed on top of the phantom at the position where the transversal slice and the sagittal slice through the center of the coil intersect. The second marker M_x was placed at the intersection between transversal and coronal slice. Due to the relatively large size of the markers, care had to be taken to ensure that the location of intersection was always through the center of the markers⁸ (Fig. 6.9).

The markers were attached to the phantom, after positioning the phantom

⁷It has to be taken care that the markers have the same material like the phantom. Like described in section (2.2.11) there is a chemical shift of about 3, 5 ppm between water and fat. At 300 MHz this means that the resonance frequencies of fat and water differ by 1040 Hz. When applying a readout gradient with a very small pixelbandwidth of e.g. $BW = 130$ Hz, this would result in a shift of oil markers compared to a water phantom by 8 mm and hence an incorrect position of the coil center. Therefore care has to be taken to either use water-based gel markers when using a water-based phantom or to apply a steep readout gradient with a broad pixelbandwidth.

⁸It is also possible to attach the markers to the coil. But in this case the FOV has to be enlarged, resulting in longer scanning times.

in the coil. With the help of the laser cross hair, first the coil can be aligned to the isocenter and after that the markers are attached to the phantom at the specific points.

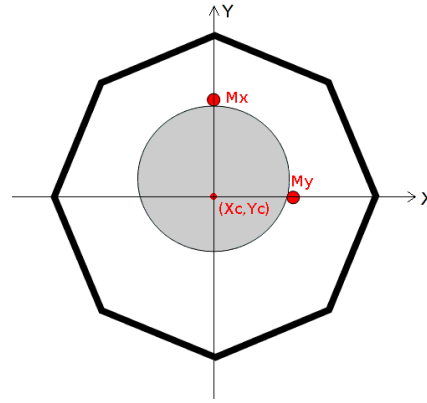


Figure 6.9: Rapid coil with the phantom inside and markers M_x and M_y attached. The x-coordinate of M_x provides the x-coordinate X_c of the coil center and the y-coordinate of M_y provides the y-coordinate Y_c of the coil center. In the z-direction, both markers are attached in the coil center (not visible in this figure), therefore both indicate the z-coordinate of the coil center Z_c .

The markers M_x and M_y deliver the coordinates (X_c, Y_c, Z_c) of the center of the coil. With these values and the values (X_b, Y_b, Z_b) ⁹ of the center of the MRI data, the exact position of the phantom within the coil could be determined (Fig. 6.10).

Problem: Theoretically, when this shift has been determined once, it should be valid for all further experiments with the same coil¹⁰. Unfortunately there are some inconsistencies in the positioning of the coil within the scanner. A variance in the z-position of the coil center of about 7 mm appeared. This distance could be observed due to a variation of the distance from the positioning laser to the isocenter of the magnet between 1793 mm and

⁹When placing the center of the slice into the isocenter of the magnet, these coordinates are (0,0,0)

¹⁰Most of the measurements showed that if the markers were positioned correctly and the x- and z-direction of the coil center were aligned to the isocenter of the magnet, these coordinates should deliver $(0, Y_c, 0)$ with $Y_c = 11,5$ for the Rapid coil

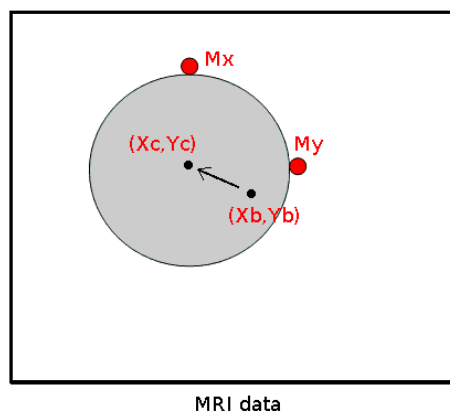


Figure 6.10: With the help of the markers the exact position of the coil center inside the MRI data can be reproduced.

1800 mm (Fig. 6.11). The reason for this deviation is currently being explored.

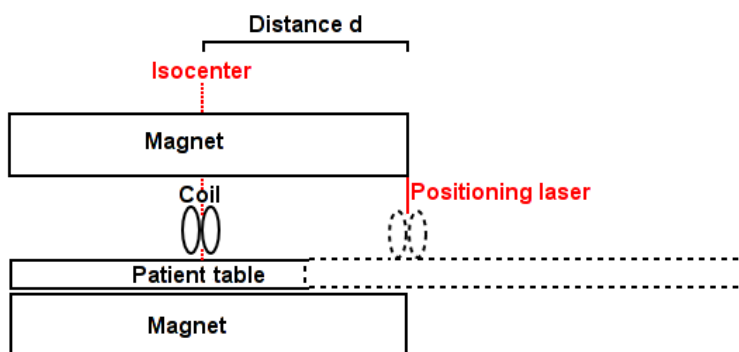


Figure 6.11: The distance d between the positioning laser and the xy -plane through the isocenter of the magnet varies between 1800 mm and 1793 mm.

Due to this variation of the coordinates, markers were placed on the phantom before every scan. This ensured that the position within the coil was determined correctly for every scan.

Another small shift of the coordinates may result from inexact coil positioning. If the coil axis is tilted even just very slightly towards the z -axis, this may result in a shift in x - or y -direction by a few mm.

6.3.2 Comparison software

The simulation data from CST is provided as an array of 3D objects which first have to be imported into MatLab with the program **ComparisonGUI.m**¹¹. The graphical user interface (GUI) of this program can be seen in figure 6.12.

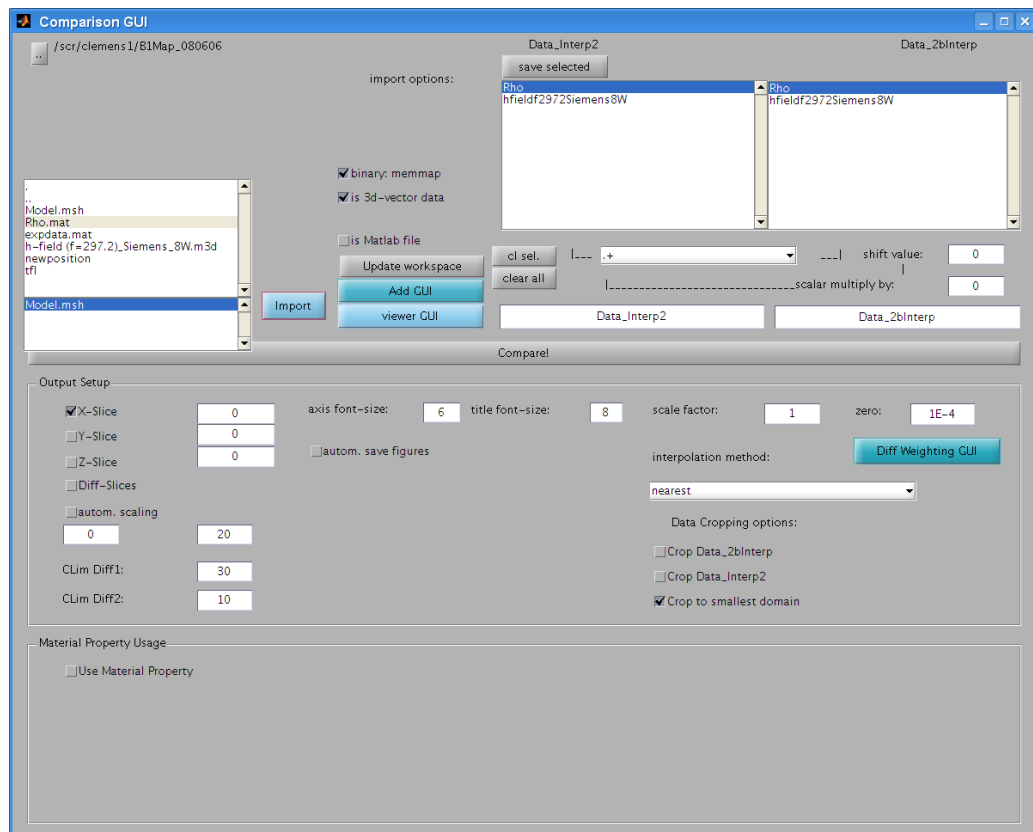


Figure 6.12: The MatLab program “ComparisonGUI.m”. In this example the data containing the information about the electromagnetic field (h-field(f=297.2)_Siemens_8W.m3d), about the mass density (Rho.mat) and for both the corresponding mesh-file (Model.msh) can be seen.

The simulation data from HFSS is provided in a table containing spatial and electromagnetic field information. The data can be converted into a form suitable for comparison by running the script Import.m (Appendix .1):

The comparison of simulation and experimental data can then be performed with

¹¹2007 by Markus Selme, University of Leipzig

the program **Compare.m** which was written by myself.

Compare.m for qualitative comparison

In this section, only the features concerning the comparison of the profile are introduced. The parts of the program that are used for the comparison of the magnitude of the B_1^+ field simulation and experiments will be presented in the next chapter (6.4).

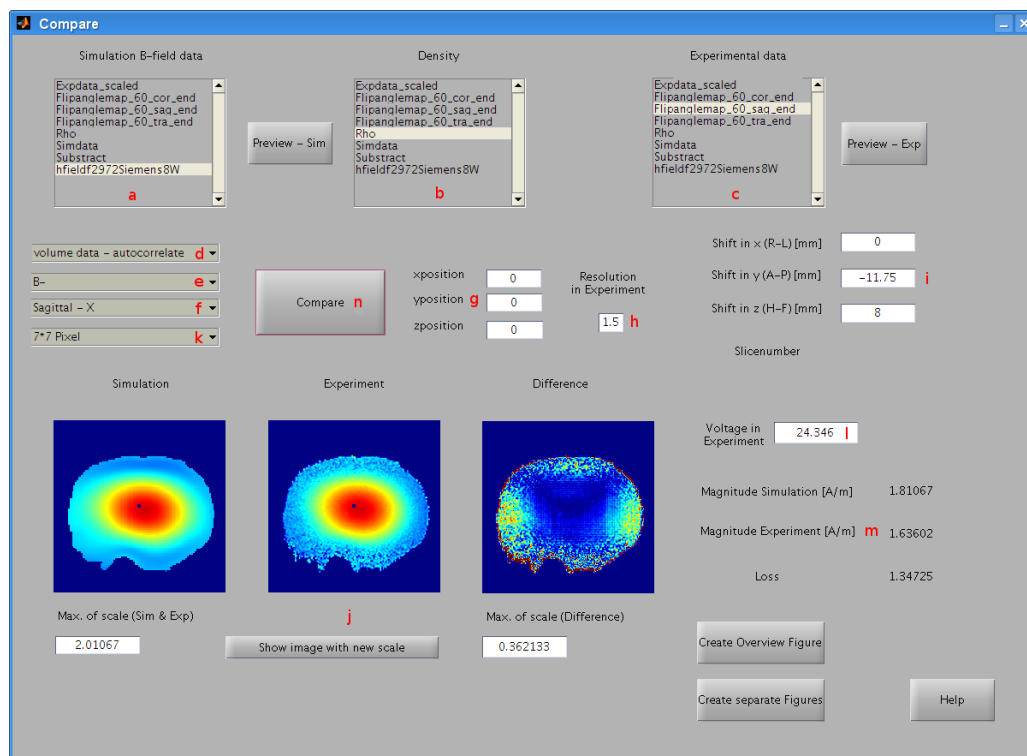


Figure 6.13: The MatLab program “Compare.m”. The explanation of the different parts from a) to n) are given in the text.

- a) Chose the electromagnetic field data from the simulation.
- b) The field for the mass density data. Using the mass density data, an image is constructed containing information about the shape of the phantom and the internal B_1^+ field distribution (Figure 6.14).
- c) The field for the experimental data that should be compared.
- d) The comparison method. CST usually delivers volume data while HFSS can

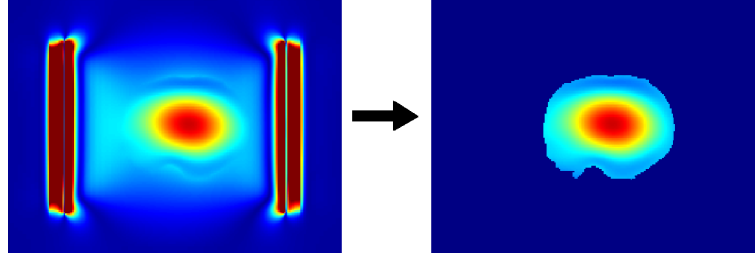


Figure 6.14: Excluding the B_1^+ field outside the phantom by using the mass density to acquire the shape.

export single slices to minimize file size and reduce export time.

To compare two images from simulation and experiment, they must be exactly aligned. The center of the simulation images is always in the coil center. To align the experimental data, it is either possible to find the coil center in the experimental image as described in section (6.3.1) or use the shapes of the phantoms to exactly superimpose both images. Because of inexact coil positioning, errors in estimation of the y-position of the coil center and inconsistencies in the scanner coordinates in z-direction (Figure 6.11), the manual positioning is sometimes erroneous and the autocorrelation therefore delivers better results.

- *Volume data - manual:* The manual positioning method is using the coordinates of the slice that are given by the scanner for matching the images. By determination of the shift between coil center and isocenter of the magnet in the experimental data, experimental data and simulation data can be aligned.
- *Volume data - autocorrelate:* When the B_1^+ map shows a phantom with sharp edges as is usually the case for reasonably small phantoms including the Skullphantom or very homogeneous phantoms such as the orange oil phantom, it is possible to perform the comparison by running a 2D cross-correlation function to match the shapes of the phantom in simulation and experimental data (Figure 6.15). For this purpose, only the shape of the phantom in the simulation and experimental data is taken to exclude any effects of the B_1^+ field. Since this method is independent of errors like

shifts in the coordinates (Fig. 6.11) or inexact coil positioning, it can provide more exact results.

However, the autocorrelation method just finds the correct position in the plane of the slice (e.g. x,y for the transversal slice), but not in the direction perpendicular to it¹².

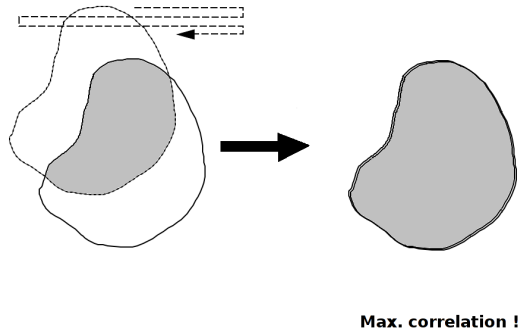


Figure 6.15: The correlation function finds the maximum correlation for the superposition of experimental and simulation data.

- *single slice*: The simulation data from HFSS comes in single slices instead of a 3D object as is the case with CST. Since at present, step b), where the shape of the phantom in the field data is acquired by using the mass density data is not yet implemented, comparison is also done manually by entering the scanner coordinates of the slices.

e) With this program, it is always intended to compare the transmit field. However, since the z-direction in the simulation may in fact be in the opposite direction than in the magnet, different equations must be used for the calculation of B_1^+ ¹³.

f) The orientation of the slices that are to be compared.

g) By default, the slice through the isocenter of the coil will be compared (*position* = 0). If another slice apart from the coil center should be compared the number of

¹²In such a case the comparison of the coronal or sagittal images can deliver the shift in z-direction. With the information about this shift, it is possible under point g) to chose another transversal slice in z-direction for comparison

¹³In this case the equation changes from equation (2.25) to (2.26)

the slice should be entered here.

h) The resolution of the experimental data.

CST For comparisons with CST, an interpolation grid with resolution 0,5mm x 0,5mm x 0,5mm is defined. Both simulation and experimental data are interpolated to the resolution of this grid.

HFSS Since the resolution of the simulation data is usually 1 mm isotropic, the experimental image has to be interpolated to the resolution of the simulation data in the case that the B_1^+ maps were acquired with a different resolution.

i) The shift of the simulation data versus the experimental data. When running the manual positioning method, the scanner coordinates of the experimental slices should be entered here. When entering the y-coordinate a value of +12 should be added to the scanner coordinate¹⁴.

If the autocorrelation is run, the shift in the x and z directions should coincide with the coordinates given by the scanner in the case that the coil positioning was correct and no deviation in z-direction occurred. The shift in y-direction should deliver the y-coordinate given by the scanner minus 12 cm for the Rapid coil.

j) The simulation data, experimental data and a subtraction of both images can be seen in this field. The difference shows the relative difference compared to the maximum magnitude of the simulation data. The scaling of the images can be changed to the desired values.

k) The region of interest that is used for the comparison of the magnitude values of the H_1^+ field. The possible sizes for the ROI are 1 pixel, 7x7 pixels and 21x21 pixels (Figure 6.23). Since noise or strong deviations of the H_1^+ field distribution in the image might result in quite different results when taking different sized ROI's, the influence of the ROI will be compared later in this chapter (Section 6.4.4).

l) The voltage of the rectangular pulse or the corresponding rectangular pulse¹⁵ (in the case a selective pulse was used) is entered here¹⁶.

¹⁴Due to the different y-position of the isocenter of the magnet and the center of the coil.

¹⁵Section 6.4

¹⁶For the double angle method where two images with angle φ and 2φ are taken, this has to be

m) The comparison of the magnitude values and the calculation of the Loss-value (Equation 6.1) for these magnitudes.

- *Magnitude simulation* shows the magnitude of the H_1^+ field of the simulation in A/m . The value shown is the mean value of the ROI chosen for the comparison.
- *Magnitude experiment* shows the magnitude of the H_1^+ field of the experiment in A/m . The value shown is the mean value of the ROI chosen for the comparison.
- *Loss* calculates the loss value by comparing the two magnitudes in the manner described in equation 6.1.

$$Loss = \frac{Voltage_{experiment}}{Voltage_{simulation} \cdot \frac{Magnitude_{experiment}}{Magnitude_{simulation}}} \quad (6.1)$$

n) Executes the comparison. The comparison consists of the following steps (Fig. 6.5):

- From the electromagnetic field data of the simulation, the B^+ field is calculated using equation (2.25) or (2.26) (depending on the selection in e)).
- The experimental data and the simulation data are interpolated to the resolution of the interpolation grid.
- The slice that should be compared is extracted from the 3D object containing the simulation data.

the value of the pulse used for the image with nominal flip angle φ

- Construct a slice containing shape and field information (point *b*)).
- Using one of the methods described in point d), the simulation and experimental data are aligned.
- Since the magnitudes of the experimental and simulation usually differ, the experimental data is scaled to the magnitude of the simulation data using the region of interest at the center of the phantom as a reference.
- The difference between simulation and experimental data is calculated.
- The magnitude values are compared.

6.4 Magnitude comparison: Simulation and Experiment

As described in section 2.2.7 the simulations deliver the magnitude of the H_1^+ field. Therefore in all the following magnitude comparisons, the magnitude of the H_1^+ field in A/m is given.

In the section above, just the qualitative comparison of the H_1^+ field profile was considered. Since the goal of the coil investigations will finally be to get a better understanding of the SAR values within the human head, a quantitative comparison is also necessary. For this purpose it must be determined how much power is delivered to the head or phantom by one pulse during the measurement. This value has to be either measured directly ¹⁷ or it has to be deduced from the pulse

¹⁷Direct measurement of the delivered power with the help of a coupler and a transient recorder would be the most exact solution to the problem. But at the time of the experiments the hardware to perform these measurements was not available yet.

shape, the length of the pulse and the maximum amplitude of the pulse.

Like described in section (2.2.4), the H_1^+ field can be extracted from the flip angle maps by

$$H_1^+ = \frac{\varphi}{2\pi\gamma\mu_r\mu_0 \int_0^\tau f(t)dt} \quad (6.2)$$

where $f(t)$ is a function describing the pulse shape, γ is the gyromagnetic ratio and μ_0 the magnetic constant.

For a rectangular pulse this equation simplifies to

$$H_1^+ = \frac{\varphi}{2\pi\gamma\tau\mu_r\mu_0}. \quad (6.3)$$

Due to the better slice profile, initial experiments were performed with a selective pulse. One way to calculate the magnitude of the H_1^+ field is to use the function $f(t)$ describing the pulse shape and calculate the magnitude with the help of equation (6.2). For various reasons the function $f(t)$ was not known to the author and also acquiring this information from Siemens was not possible. Therefore another way, leading to the same result, had to be applied. It consists of recalculating the real pulse to the corresponding rectangular pulse which delivers the same amount of power (Fig. 6.16), and then using equation (6.3) to calculate the magnitude of H_1^+ . Several methods for estimating the real pulse shape were applied.

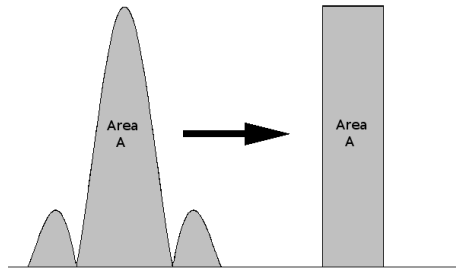


Figure 6.16: Recalculation from a selective pulse to a rectangular pulse.

It can be seen in equation (6.2) that the flip angle can be directly estimated from

the ratio of the signal intensity of two different images and which is therefore fixed for a certain experiment. On the other hand the magnitude of the H_1^+ field can vary depending on the pulse shape that is assumed for the calculations. Hence, a different pulse shape would result in a different pulse length or peak amplitude for the corresponding rectangular pulse¹⁸.

Example:

$$\varphi = 90^\circ, \tau = 2 \text{ ms} \rightarrow H_1^+ = \frac{90^\circ}{2\gamma\pi\mu_0 \cdot 2 \text{ ms}} = 2,34 \text{ A/m} \quad (6.4)$$

$$\varphi = 90^\circ, \tau = 1 \text{ ms} \rightarrow H_1^+ = \frac{90^\circ}{2\gamma\pi\mu_0 \cdot 1 \text{ ms}} = 4,68 \text{ A/m} \quad (6.5)$$

Note: The H_1^+ mapping methods in fact only deliver the actual flip angles. The magnitude of the H_1^+ field is not known! For the calculation of the magnitude, additional information about the applied pulses is necessary. Therefore in the following tables different magnitudes of the H_1^+ field are presented, even though the experimental data for each individual phantom remained the same. The goal of finding the real pulse shape is to find the correct value for τ to calculate the magnitude of the H_1^+ field.

6.4.1 Sinc pulse approximation

The pulse used for the experiments has a selective pulse shape, similar to a sinc pulse. According to Bottomley [Bottomley, Redington, Edelstein, & Schenck, 1985], a rectangular pulse and a sinc pulse of the same amplitude will produce equivalent flip angles if

$$\tau_r = \tau_z/2 \quad (6.6)$$

where τ_r is the length of the rectangular pulse and τ_z is the width of the central

¹⁸This is one important fact that is used for reducing the input power during an experiment! By applying pulses with a longer pulse length, the magnitude of the H_1^+ field is reduced and therefore the SAR value for the whole experiment can be decreased.

lobe of the sinc function at the zero point crossing.

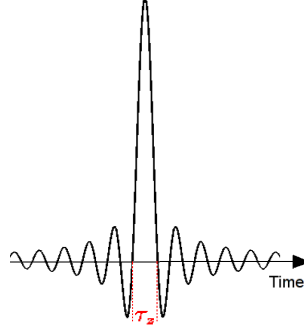


Figure 6.17: τ_z is the width of the central lobe at the zero point crossing.

For the following experiments, the amplitude of the selective pulse is $V = 94,2 V$, the total pulse length is $\tau = 2,56 ms$ and the length of the central lobe is $\tau_z = 2 ms$.

This means that the corresponding rectangular pulse would have an amplitude of $94,2 V$ over the time of $\tau_r = 1 ms$.

This rectangular pulse is now the basis for the calculations of the magnitude of the H_1^+ field of the experimental data in table 6.1. The *Loss* value is calculated by using equation (6.1) and represents the loss in driving voltage between the TALES and the coil element (Section 6.4.4).

Since the sinc pulse was just an approximation, further investigations of the pulse shape were made and the effect on the magnitude of the H_1^+ field depending on the approximation method examined.

	Pulse amplitude	Magnitude H_1^+ field
Experiment	94,2 V	3,97 A/m
Simulation	20 V	1,493 A/m
	↓	↓
Simulation _{rescaled}	53,18 V	3,97 A/m
	↓	
Loss ($\frac{Experiment}{Simulation_{rescaled}}$)	1,77	

Table 6.1: Comparison of the magnitude of the H_1^+ field in Phantom046 (Table 3.3). The calculation of the magnitude of the experimental data is based on a rectangular pulse with pulse length $\tau = 1\text{ ms}$ and amplitude given in the table.

6.4.2 Pulse length according to the IDEA Poet Simulation

Instead of approximating to a sinc pulse, a method to determine the real pulse shape was applied. The FLASH sequence was opened with the IDEA Poet Simulation tool (Fig. 6.18).

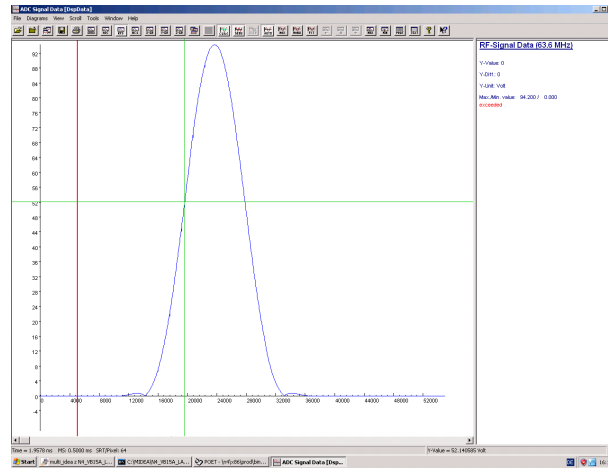


Figure 6.18: Pulse shape in the IDEA Poet sequence simulation tool

One pulse was chosen and 17 Amplitude-Time pairs between the beginning of this pulse and the main peak of this pulse were taken. The acquired data was fitted with MatLab to a 5th grade polynomial (Fig. 6.19).

This fitting function was then integrated in the time duration from the beginning of the pulse to the main peak of the pulse. The total area under the pulse could now be obtained by multiplying the resultant integral by a factor of 2, because

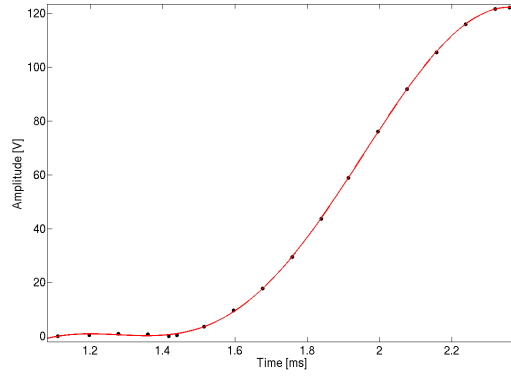


Figure 6.19: The pulse shape for of the actually applied pulse fitted with MatLab.

symmetric pulses were used. Since all the calculations are based on a rectangular pulse shape, the ratio between this integral and a rectangular pulse of the same pulse length and with the same maximum amplitude was calculated (Fig. 6.20). This ratio was found to be

$$\frac{Area_{actual\ pulse}}{Area_{rectangular\ pulse}} = 0,354 \quad (6.7)$$

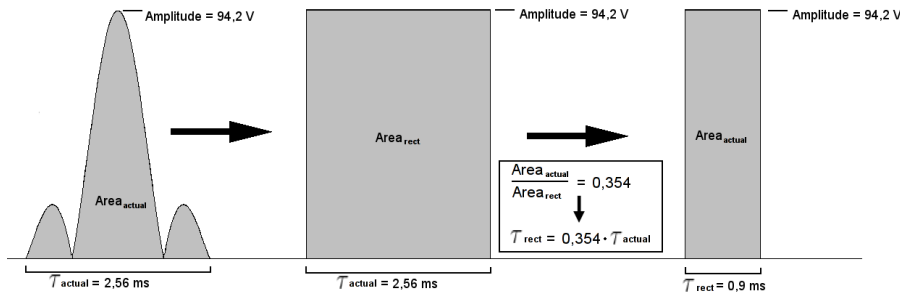


Figure 6.20: Recalculation from the selective pulse (left) to the corresponding rectangular pulse (right)

The magnitude of the H_1^+ field of the experimental data in Table 6.2 is now based upon a rectangular pulse with a pulse length of

$$\tau_{rect} = [\tau_{actual}] \cdot 0,354 = 2,56\ ms \cdot 0,354 = 0,91\ ms. \quad (6.8)$$

6.4. MAGNITUDE COMPARISON: SIMULATION AND EXPERIMENT 131

A rectangular pulse with pulse length $\tau = 0,91 \text{ ms}$ is therefore assumed for the calculations of the magnitude of the H_1^+ field in Table 6.2.

	Pulse amplitude	Magnitude H^+ field
Experiment	94,2 V	4,41 A/m
Simulation	20 V	1,493 A/m
	↓	↓
Simulation _{rescaled}	59,08 V	4,41 A/m
	↓	
Loss ($\frac{\text{Experiment}}{\text{Simulation}_{\text{rescaled}}}$)	1,59	

Table 6.2: Comparison of the magnitude of the H_1^+ field in Phantom046 (Table 3.3). The calculation of the magnitude of the experimental data is based on the a rectangular pulse with pulse length $\tau = 0,91 \text{ ms}$.

6.4.3 Acquiring the slices with a rectangular pulse

In the previous section two different attempts for approximating the selective pulse to a rectangular pulse delivered quite different results. If the recalculation from selective to rectangular pulse is incorrect, this leads therefore to a big error in the magnitude calculation.

To avoid this problem, the gradient echo sequence was modified in such a way that the selective pulses were replaced by rectangular pulses. The big advantage of using rectangular pulses is that by knowing the pulse length, the magnitude of the H_1^+ field can be calculated directly from the flip angle. In this way, errors which might occur from recalculations of the real pulse shape can be completely avoided.

The drawback of this procedure is the very bad slice selectivity of a rectangular pulse. This results in slightly worse image quality than the images taken with the former slice selective pulse sequence. However, experiments showed that differences in the image quality were quite low (Fig. 6.21).

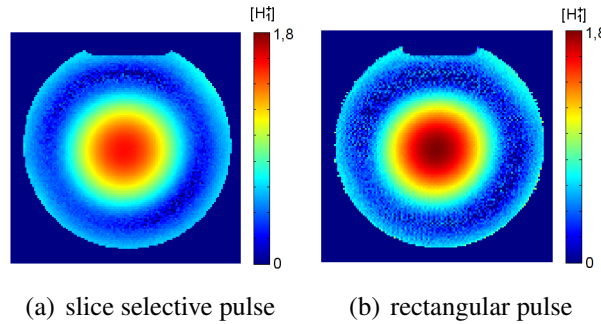


Figure 6.21: B_1^+ maps of Phantom046 (Table 3.3) showing the transversal slices through the center of the Rapid coil. The images were taken with a slice selective pulse and a rectangular pulse with a nominal flip angle of $\varphi_n = 60^\circ$. As described in section (5.4.2) the rectangular pulse delivers in the center a 16% higher magnitude than the selective pulse.

A rectangular pulse with amplitude 33, 3V and a pulse length of $\tau = 2,56\text{ ms}$ was the basis for the magnitude calculation in Table 6.3.

	Pulse amplitude	Magnitude H_1^+ field
Experiment	33,3 V	1,796 A/m
Simulation	20 V	1,493 A/m
	↓	↓
Simulation _{rescaled}	24,01 V	1,796 A/m
	↓	
Loss ($\frac{Experiment}{Simulation_{rescaled}}$)	1,38	

Table 6.3: Comparison of the magnitude of the H_1^+ field in Phantom046 (Table 3.3). The calculation of the magnitude of the experimental data is based on a rectangular pulse with pulse length $\tau = 2,56\text{ ms}$.

6.4.4 Loss between TALES and coil

The circuit between the power amplifier and the coil can be seen in figure 6.22.

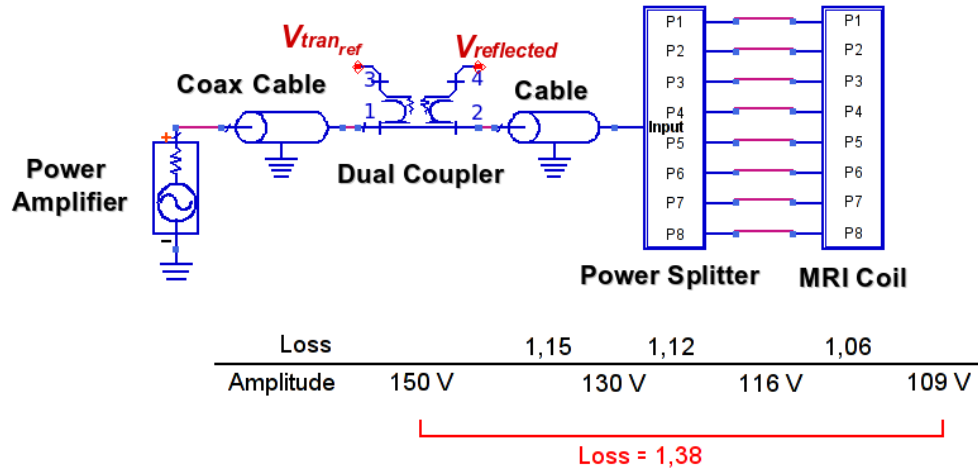


Figure 6.22: The circuit between power amplifier and coil. The losses for the different elements and the power amplitude of the pulse after experiencing the particular losses as indicated.

The amplitude value of the pulse that is used for the experiments is always measured at the TALES¹⁹, where the dual coupler is located. On the other hand, the amplitude value of the pulse for the simulation is exactly the amplitude that is leaving the MRI coil. Between the TALES and the MRI coil there are three components which decrease the amplitude of the pulse. These components are:

¹⁹Transmit Antenna LEvel Sensor

- the cable between coupler and splitter
- the splitter
- the phase shifter inside the MRI coil

In figure 6.22, the different loss values for the components and the amplitude of the pulse after passing such a component are included in Volts. This shows that the loss value estimated by using a rectangular pulse is quite realistic and the comparison of the simulation and experimental data is feasible. But a direct measurement of the Loss-value with the help of a network analyzer would still be desirable to confirm the theoretically estimated values.

For oil phantoms there is a deviation from this theoretically estimated loss value. Experiments with oil phantoms showed that the difference in magnitude between experimental data and simulation data leads to a loss value of about 1,46. The coils in the simulations are just tuned on water based phantoms. To reach a better match for oil based phantoms, comparison with the retuned coil in the simulation would be necessary.

Influence of ROI on Loss-value

It was examined whether or not the size of the ROI (Figure 6.23) that is used for the comparison of the magnitude values influences the final loss-value. As noise in the experimental data might lead to strong deviations of the magnitude value for one pixel, the magnitude value for the experiments was also estimated in bigger regions of interest in the center of the image where the signal was quite strong.

In addition, if the H_1^+ profile of the simulation and experiment differ very much, it is obvious that the magnitude values of the simulation and experiment also differ by a considerable amount if we increase the ROI used for this comparison. Therefore, examination of the change in the loss-value through a variation in the ROI size also gives an indication of the consistency of the H_1^+ profile in both simulations and experiments.

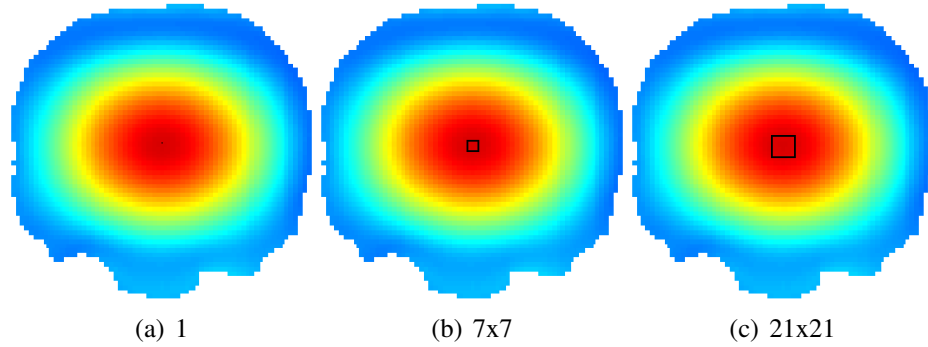


Figure 6.23: The different ROI sizes that were examined. The number shows the size of the ROI in pixels. The mean of the depicted ROIs was taken for the comparison of the magnitude values

Experiment: The influence of the size of the ROI was examined for 3 phantoms (Section 3.3) with very different characteristics:

- The orange oil phantom with an almost homogeneous H_1^+ field.
- The Sugarphantom with symmetric shape but strong central brightening
- A skull filled with brain-equivalent gel, with an unsymmetrical shape and central brightening.

For all 3 phantoms the simulation and experimental data were compared. For the magnitude of the H_1^+ field taken for the comparison, the mean of a ROI around the center of the phantom was taken. The comparison was performed for each phantom with three different ROI sizes. The simulation data was acquired with the CST Studio Suite. Hence, the loss-value could be calculated from the mean magnitude values. The calculated loss-values for all phantoms and all the different ROI sizes can be seen in table 6.4.

The results show that the size of the ROI does not have a big influence on the comparison of the magnitude values. This points to the stability of the comparison procedure and to a good agreement of the profiles of simulation and experimental data.

	ROI size in pixel	LOSS		
		transversal	coronal	sagittal
Orange Phantom	1	1,47	1,47	1,47
	7x7	1,46	1,46	1,46
	21x21	1,47	1,47	1,47
Skullphantom	1	1,33	1,33	1,33
	7x7	1,35	1,36	1,36
	21x21	1,34	1,35	1,35
Sugarphantom	1	1,38	1,38	1,38
	7x7	1,38	1,37	1,38
	21x21	1,36	1,36	1,36

Table 6.4: The mean of regions with a different size was used for the calculation of the loss-value. The mesh size for the Skullphantom was smaller than for the Sugarphantom, resulting in a slight difference in the loss-value.

6.4.5 Relation load - magnitude H_1^+ field

The influence of the loading of the coil on the magnitude of the H_1^+ field was investigated. For this purpose, a H_1^+ map with nominal flip angle of $\varphi_n = 60^\circ$ was acquired for 4 different water based phantoms with different electromagnetic parameters of different volume. Since the adjustments deliver a different reference amplitude depending on the loading of the coil, the amplitude of the pulses for φ_n differed for each phantom (Table 6.6). The phantoms and their parameters can be seen in Table (6.5).

Phantom	Volume inside coil	Conductivity
Skull	1,3 l	$\sigma = 0,50 S/m$
Phantom046	2 l	$\sigma = 0,46 S/m$
Siemens phantom 5512 608 K2205	5 l	$\sigma = 0,52 S/m$
Sugarphantom	3,5 l	$\sigma = 0,63 S/m$
Phantom091	2 l	$\sigma = 0,91 S/m$

Table 6.5: Phantoms with different load

The loading of the coil is increasing with bigger volume and rising conductivity. In table (6.6) the 4 water based phantoms are listed ascending with increasing load. The magnitude values of the H_1^+ field for all phantoms are scaled to the magnitude corresponding to a 50 V pulse.

Phantom	Pulse amplitude	Magnitude H_1^+	\Rightarrow	Magnitude H_1^+ for 50 V Pulse
Skull	24 V	1,65 A/m	\Rightarrow	3,44 A/m
Phantom046	33 V	1,79 A/m	\Rightarrow	2,71 A/m
Blue Siemens phantom	34 V	1,49 A/m	\Rightarrow	2,19 A/m
Sugarphantom	45 V	1,55 A/m	\Rightarrow	1,72 A/m
Phantom091	49 V	1,51 A/m	\Rightarrow	1,54 A/m

Table 6.6: Magnitude of the H_1^+ field for different phantoms

It is clear that with increasing load the magnitude of the H_1^+ field is decreasing. This coincides very well with the results shown by Ibrahim [Hue & Ibrahim, 2008]. The dampening of electromagnetic waves in a sample increases with the conductivity of the sample and with the propagation distance in the dielectric medium. Even though the input power of the RF radiation is the same, the power absorption for different media varies significantly depending on the sample size and conductivity.

6.4.6 Influence of the mesh size used for the simulations

As described in section 6.2, the simulation space is divided into a mesh. It is expected that a finer mesh will deliver more accurate results than a coarse mesh. **Experiment:** A H_1^+ field map of the blue Siemens phantom in the Rapid coil was compared with the simulation data from 5 different simulations. The number of mesh cells ranged from about 6 Mio. for the smallest mesh to almost 60 Mio. for the finest mesh. This corresponds to the size of an average mesh cell from 2,5 mm isotropic to 1 mm isotropic. Figure 6.24 shows the loss values for the different mesh sizes.

For very small mesh sizes, quite some difference in the calculation of the magnitude of the H_1^+ field can be observed leading to a deviation of the loss value. However, above a certain mesh size, in this figure above a size of 2 mm isotropic for a single mesh cell, changing the mesh size no longer leads to a big difference in the calculation of the magnitude.

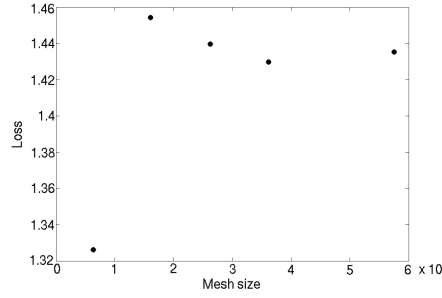


Figure 6.24: One H_1^+ map experiment is compared with 5 simulations, all performed with a different mesh size.

6.5 Profile comparison for several phantoms

In the following section, qualitative comparisons of the profile of the H_1^+ field (eq. 2.29) of the simulation and experiments were performed. Since the magnitude of the simulation data and the experimental data differed, the experimental data was scaled to the magnitude of the simulation data. The results for the magnitude comparisons are also given for each phantom.

1. The orange oil phantom was placed in the center²⁰ of the Rapid coil. A H_1^+ map was acquired using the double angle method (4.3.2). For the simulations a perfect sphere with radius $r = 85\text{ mm}$ was assumed. The electromagnetic parameters of the oil were $\varepsilon = 3,2$ and $\sigma = 0,003\text{ S/m}$ (Table 3.3).

The acquired maps and the difference between the simulation and experiment can be seen in Figures 6.25, 6.26 and 6.27.

The comparison of the magnitude of the H_1^+ field is given in table (6.7).

The H_1^+ maps of simulation and experiment show several differences. Additionally, the Loss-value is 0,08 higher than the theoretically estimated value (Fig. 6.22). There are various reasons for these deviations. First, in the simulations the orange oil phantom was approximated by a perfect sphere. On the other hand the real phantom from the experiments is not

²⁰for this particular phantom a blue positioning cushion can be used to position the phantom exactly in the coil center

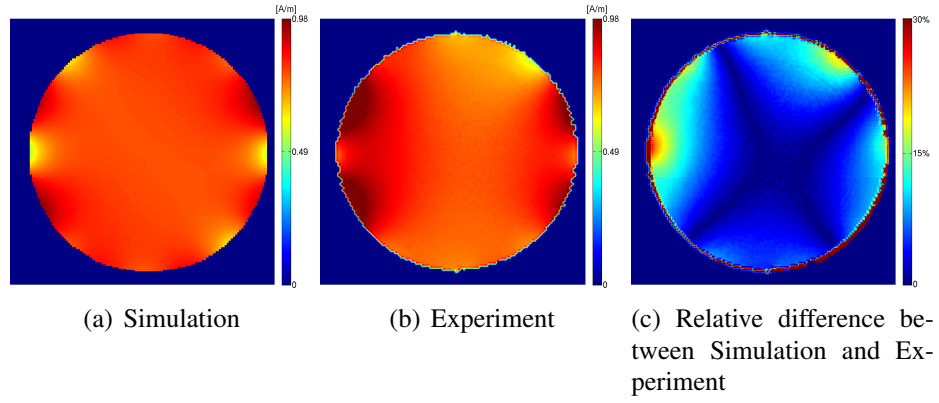


Figure 6.25: Comparison of the transversal slices of the orange oil phantom, scale bar shows absolute magnitude of the H_1^+ field.

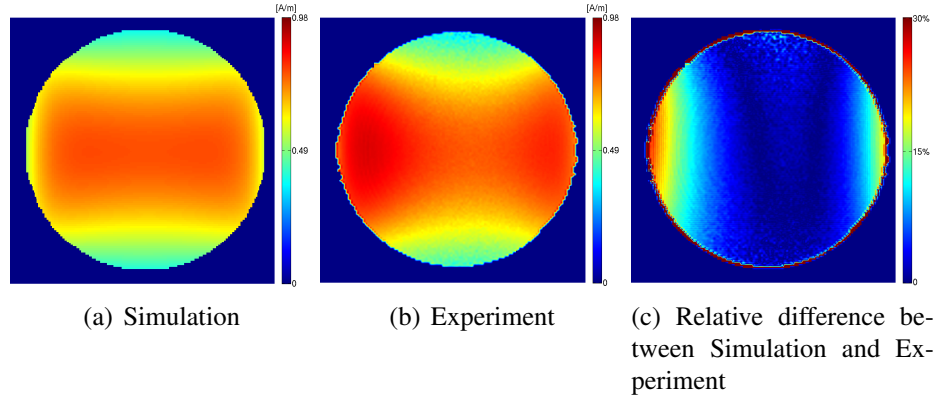


Figure 6.26: Comparison of the coronal slices of the orange oil phantom, scale bar shows absolute magnitude of the H_1^+ field.

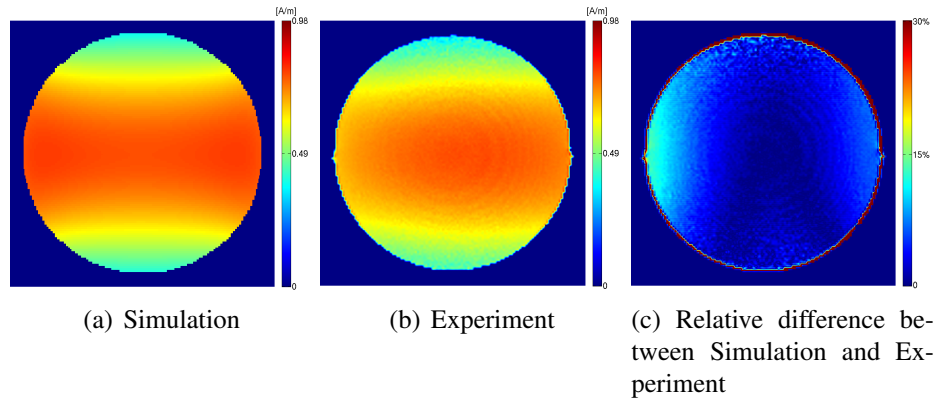


Figure 6.27: Comparison of the sagittal slices of the orange oil phantom, scale bar shows absolute magnitude of the H_1^+ field.

	Pulse amplitude	Magnitude H_1^+ field
Experiment	43 V	1,16 A/m
Simulation	20 V	0,79 A/m
	↓	↓
Simulation _{rescaled}	29,4 V	1,16 A/m
	↓	
Loss ($\frac{Experiment}{Simulation_{rescaled}}$)	1,46	

Table 6.7: Comparison of the magnitude of the H_1^+ field in the orange oil phantom (Table 3.3).

completely symmetric due to the lid. Secondly the coil in the simulation was not yet tuned for the phantom used by the coil vender, in this case the Siemens phantom 5512 608 K2205.

2. The Sugarphantom was placed inside the coil. Markers were attached to the phantom to determine its exact position relative to the coil. A H_1^+ map was acquired using the Double angle method (4.3.2). The electromagnetic parameters of the sugar-water mixture inside the bottle were $\varepsilon = 54$ and $\sigma = 0,63 \text{ S/m}$ (Table 3.3).

The simulations were performed with two different models:

- For the bottle body a cylinder with radius $r = 74 \text{ mm}$ and length $h = 206 \text{ mm}$ and for the bottle neck a cylinder with $r = 36 \text{ mm}$ and length $h = 32 \text{ mm}$ was assumed (Fig. 6.28 a)) The position of the bottle was approximated to be exactly in the coil center.
- A 3D scan of the bottle was performed and a 3D voxel data object could be acquired from the data (Fig. 6.28 b)) The position was determined exactly with the help of the attached markers.

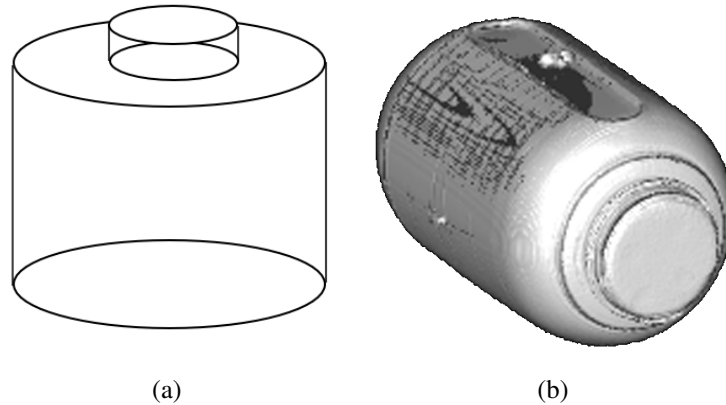


Figure 6.28: a) An approximation of the bottle by cylindrical objects (The picture shown is just a schematic representation. The radius, height and positioning were the same as for the real phantom.). b) The bottle as a 3D voxel object.

The acquired maps and the difference between the simulation and the experiment can be seen in Figures 6.29, 6.30 and 6.31. In the images shown, the comparison of the profile is done between the voxel data simulation and the experiment. To show the influence of the shape of the object on the field distribution, the cylindrical approximation simulation data was added. The comparison of the magnitude of the H_1^+ field is given in table (6.7). The

magnitude is compared for the voxel data model²¹.

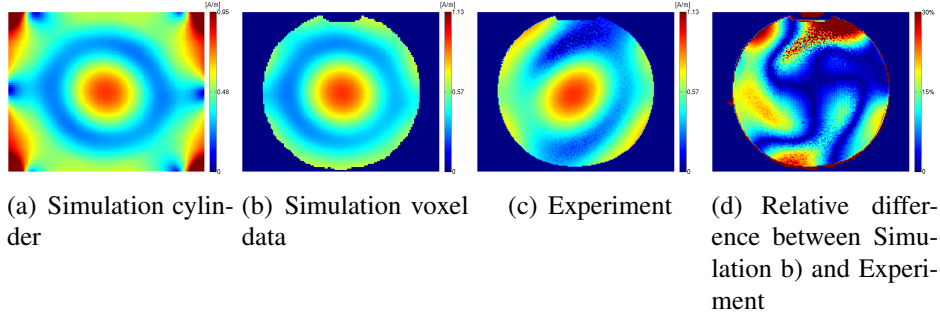


Figure 6.29: Comparison of the transversal slices of the Sugarphantom, the scale bar showing the absolute magnitude of the H_1^+ field. The magnitude of the experimental data is scaled to the simulation data acquired by simulating the voxel data model. In the simulation data acquired by simulating the approximation by cylindrical objects, the influence of the shape on the field distribution can be seen.

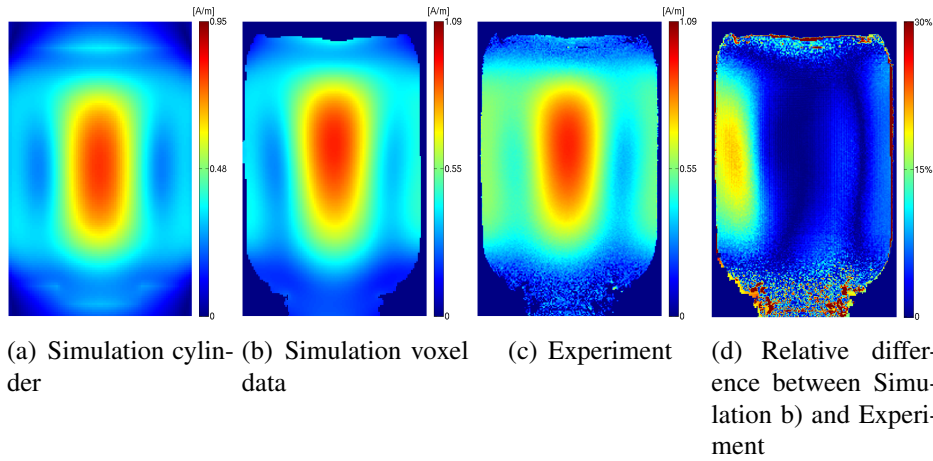


Figure 6.30: Comparison of the sagittal slices of the Sugarphantom, the scale bar showing the absolute magnitude of the H_1^+ field. The magnitude of the experimental data is scaled to the simulation data acquired by simulating the voxel data model.

The influence of phase definition for different coil elements Each of the 8 elements from the Rapid coil sends its own transmit H_1 field. In an array with N elements, the application of a phase shift between neighbouring

²¹The difference in the magnitude values for the analytical shape and the real shape of about 0, 2 A/m might be due to a different mesh size for the simulations of the different shapes.

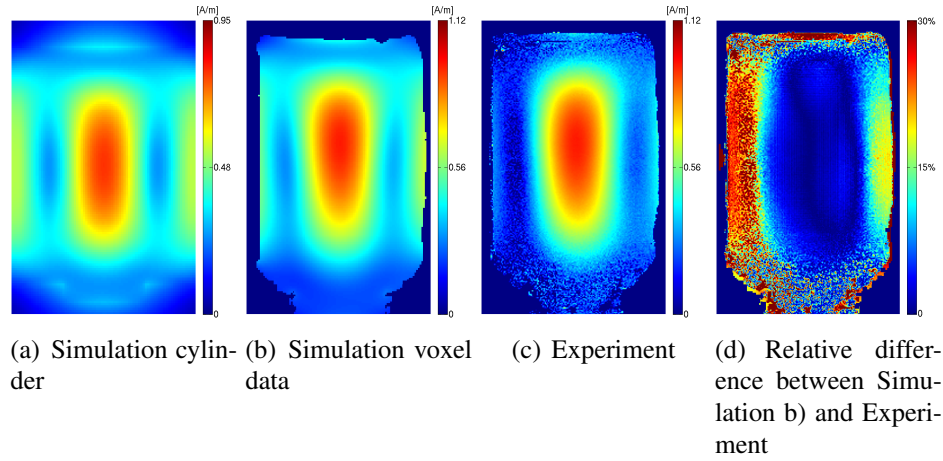


Figure 6.31: Comparison of the sagittal slices of the Sugarphantom, the scale bar showing the absolute magnitude of the H_1^+ field. The magnitude of the experimental data is scaled to the simulation data acquired by simulating the voxel data model.

	Pulse amplitude	Magnitude H_1^+ field
Experiment	51,6 V	1,69 A/m
Simulation	20 V	0,89 A/m
	↓	↓
Simulation _{rescaled}	37,9 V	1,69 A/m
	↓	
Loss ($\frac{Experiment}{Simulation_{rescaled}}$)	1,36	

Table 6.8: Comparison of the magnitude of the H_1^+ field in the Sugarphantom (Table 3.3).

elements of $\frac{360^\circ}{N}$ leads to an almost circularly polarized H_1 field. Therefore, the main part of the H_1 field would contribute to the circularly polarized transmit H_1^+ field (Section 2.2.6). This way the H_1 field is used most effectively for rotating the spins. In the simulation data of the transversal slices a distinctive shape of the part with the low signal and also a slight distortion of the area with high magnitude can be observed. The same pattern can be observed in the experimental data but shifted in another direction. The mismatch of these patterns may result from a discrepancy in the phase of the coil elements in the simulation data. The effect of a change in the phase definition of the coil elements on the H_1^+ field distribution can be seen in fig. (6.32).

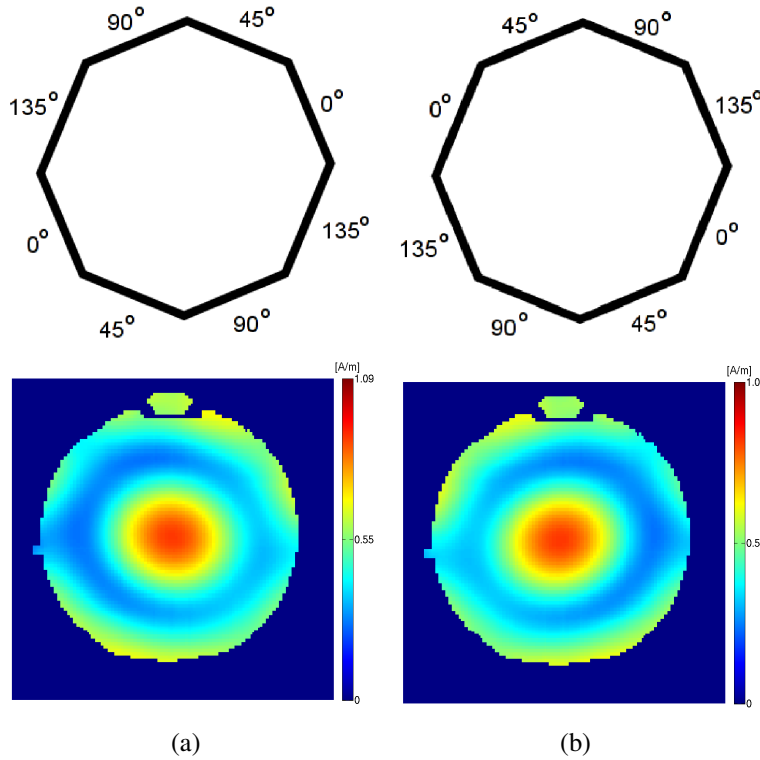


Figure 6.32: The images in the upper row show the phase definition of the coil elements. The images in the lower row show the resultant H_1^+ maps. Because the current in two elements which show the same phase runs in opposite directions, a phase shift of 180° must be added to one of the values to determine the absolute value.

The images clearly show the influence of the phase of the coil elements on the H_1^+ map. Further enhancement of the simulation data by adjusting the phase of each element to reach a perfect match has not yet been accomplished.

This mismatch in the phase of the elements also leads to the big differences between experimental and simulation data at the periphery of the phantom in Figures (6.30) and (6.31)²².

²²Update: Recently it was indeed confirmed that the Rapid coil used for at least some of the latest experiments had an incorrect phase value in 2 elements that lead to these deviations in the H_1^+ profile.

3. A skull filled with a brain-equivalent gel was placed into the coil. A 3D scan was taken to acquire a voxel object of the skull for the simulations. The electromagnetic parameters of the gel were $\varepsilon = 50, 2$ and $\sigma = 0, 5 S/m$. The acquired maps and the difference between the simulation and the experiment can be seen in Figures 6.33, 6.34 and 6.35.

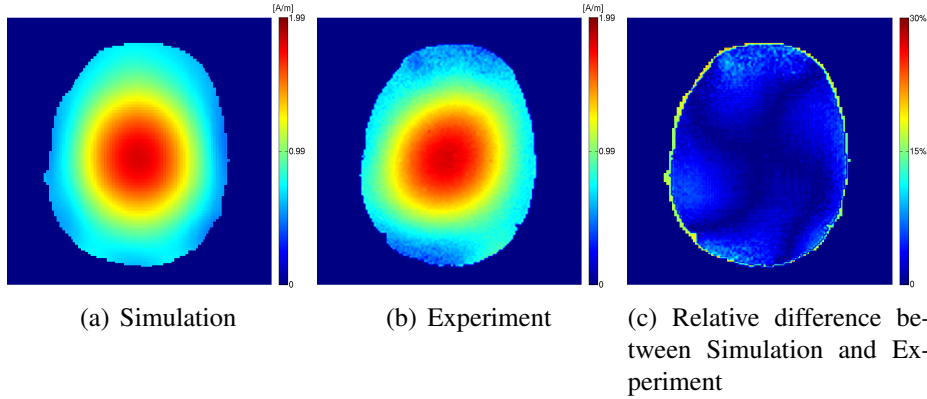


Figure 6.33: Comparison of the transversal slices of the skull phantom, the scale bar showing the absolute magnitude of the H_1^+ field.

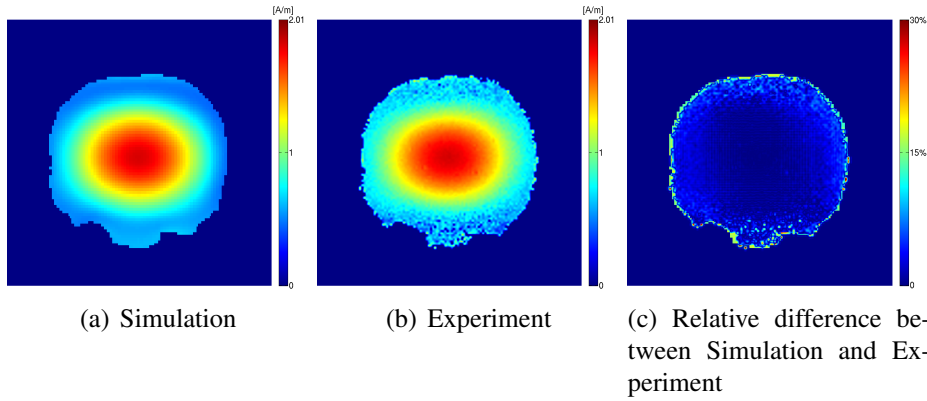


Figure 6.34: Comparison of the coronal slices of the skull phantom, the scale bar showing the absolute magnitude of the H_1^+ field.

In the comparison of the transversal slices again the influence of the phase definition on the H_1^+ map can be observed. This leads so a slightly different shape of the H_1^+ field in simulation and experiment. Otherwise the match between the images is very good and also the Loss-value acquired from these images is very close to the theoretically estimated value of 1,38.

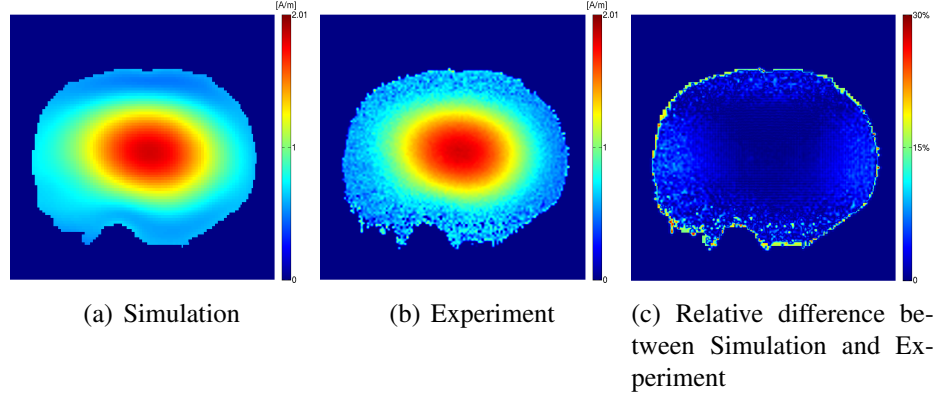


Figure 6.35: Comparison of the sagittal slices of the skull phantom, the scale bar showing absolute magnitude of the H_1^+ field.

	Pulse amplitude	Magnitude H_1^+ field
Experiment	24,3 V	1,65 A/m
Simulation	20 V	1,83 A/m
	↓	↓
Simulation _{rescaled}	18 V	1,65 A/m
	↓	
Loss $\left(\frac{Experiment}{Simulation_{rescaled}}\right)$	1,35	

Table 6.9: Comparison of the magnitude of the H_1^+ field in the skull phantom.

4. A head phantom, consisting of 3 different materials for the head, the skull and the brain was placed into the coil. Several body tissues were simulated with different gels. The electromagnetic parameters of the head phantom can be seen in table (6.10). A 3D scan was taken to acquire a voxel object of the head phantom for the simulations. The segmentation of the different parts was performed with MatLab (Fig. 6.36). H_1^+ maps using the double angle method (GRE) were acquired.

The resultant maps and the difference between the simulation and the experiment can be seen in Figures 6.37, 6.38 and 6.39.

Simulated body tissue	Material	Properties
Brain	Agar gel	$\varepsilon = 50, 2; \sigma = 0, 5 S/m$
Muscle	Agar gel	$\varepsilon = 57, 5; \sigma = 0, 9 S/m$
Skull ²³	Polyurethane	$\varepsilon = 2, 3; \sigma = 0 S/m$

Table 6.10: Properties of the different materials in the head phantom.



Figure 6.36: The segmented head phantom that was used for the simulations. Different materials are assigned with different values. Some of the gaps which are visible in this image result from the segmentation process and not from the real phantom. This might lead to some deviations of the H_1^+ map from the experimental data.

Significant differences can be observed in both the H_1^+ field distribution and the magnitude of the H_1^+ field compared to the former experiments. Besides the known problems from the phase definition of the coil elements, another problem appears. At present, the primary problem in simulating of

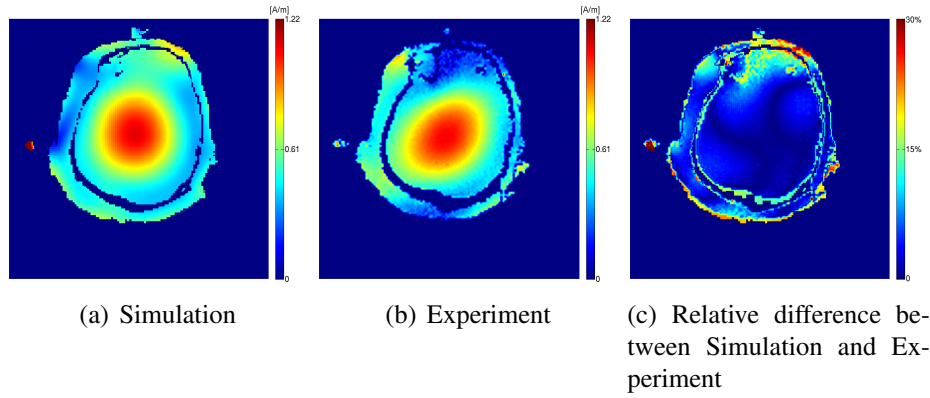


Figure 6.37: Comparison of the transversal slices of the head phantom, scale bar shows absolute magnitude of the H_1^+ field.

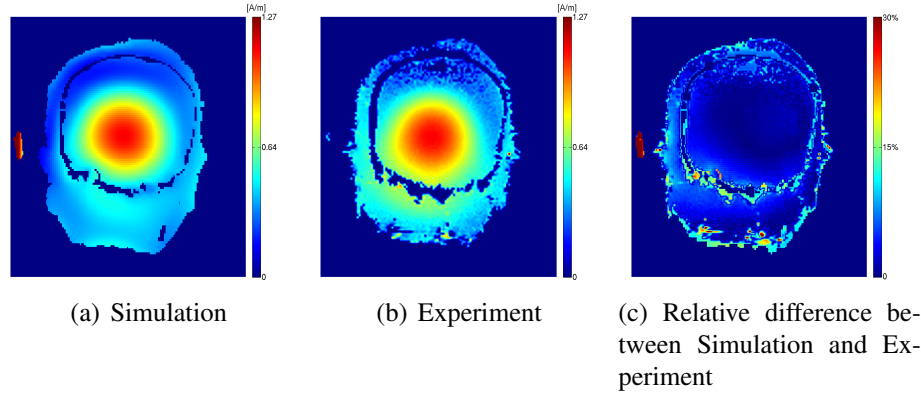


Figure 6.38: Comparison of the coronal slices of the head phantom, scale bar shows absolute magnitude of the H_1^+ field.

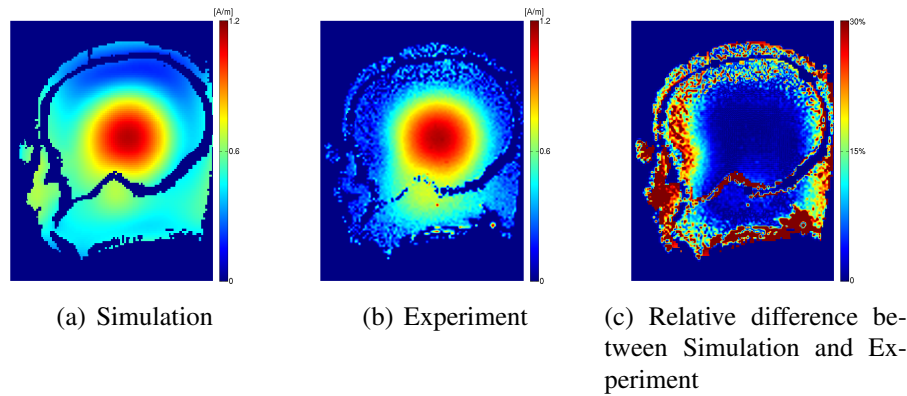


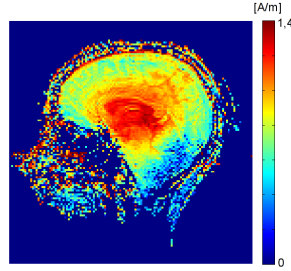
Figure 6.39: Comparison of the sagittal slices of the head phantom, scale bar shows absolute magnitude of the H_1^+ field.

	Pulse amplitude	Magnitude H_1^+ field
Experiment	32,8 V	1,41 A/m
Simulation	20 V	1,07 A/m
	↓	↓
Simulation _{rescaled}	26,3 V	1,41 A/m
	↓	
Loss ($\frac{Experiment}{Simulation_{rescaled}}$)	1,25	

Table 6.11: Comparison of the magnitude of the H_1^+ field in the skull phantom.

phantoms such as the head phantoms is to get the correct voxel data representation for the simulations. During the segmentation process the shape of the phantom is slightly altered²⁴. During the comparison procedure this also causes problems for the autocorrelation method because of the differences in the shape of simulation data and experimental data. A more accurate segmentation algorithm for achieving a voxel data object which resembles the original phantom 1 : 1 will therefore be necessary.

An in vivo measurement of a female patient with a small head size comparable to the head phantom can be seen in Fig. (6.40).

Figure 6.40: An H_1^+ map of a female volunteer with a comparable head size to the phantom size.

Both the phantom and the head show in the center a region with a very strong H_1^+ field magnitude. The comparison of the reference amplitude and the magnitude values can be seen in Table 6.12.

²⁴This can be observed in the comparison images, where the shape of the phantom in simulation and experimental data is varying in some parts.

	Reference amplitude	Head mass	Maximum Magnitude H_1^+ field
Head Phantom	252 V	4,8 kg	1,54 A/m
Volunteer	246 V	5,1 kg	1,36 A/m
Difference	2%		12%

Table 6.12: Comparison of the reference amplitude and the H_1^+ field magnitude in the head phantom and a female volunteer. The magnitude value is the maximum magnitude of the H_1^+ field measured in the bright region around the center of the phantom and the head.

Since the shape as well as the size of the phantom and the head of the volunteer is not exactly the same, a difference between the values is expected. But as it is relatively small it can be concluded that the phantom provides a realistic dielectric environment and can be used for simulating the behaviour of the H_1^+ field in the human head²⁵.

6.6 Summary

At present simulations of a well defined model that is obtained from experimentally measured phantoms are only possible with the CST Studio Suite. With HFSS just approximations of the phantoms by analytical elements can be performed.

The comparison program “Compare.m” makes various comparison methods possible. These methods are

Autocorrelation, which finds the best match of the phantom position for simulation and experimental data

Position, where the estimated position of the phantom within the coil is taken for the superposition of simulation and experimental data.

While the autocorrelation method naturally just works, if the whole shape of the phantom is visible in the H_1^+ maps the positioning method works always, but needs sometimes adjustments of the position due to inconsistencies of the scan-

²⁵The presented in vivo measurement was the only experiment in this thesis that was already performed with the correctly working Rapid coil that was received as a substitute for the old coil. The incorrect phase definition in the coil used for the head model measurement might also have lead to a small deviation of the values.

ner coordinates.

Different methods were applied to retrieve information about the magnitude of the H_1^+ field in the experiments. With a known flip angle the amplitude, length and shape of a certain pulse must be known to deduce the magnitude of the field. Since for non-rectangular pulse shapes only amplitude and length of the pulse were known, several methods for approximating the real pulse shape were applied. However, since they all delivered quite different results, a rectangular pulse was implemented to avoid the error that might occur when approximating the pulse shape.

The experiments with rectangular pulses provided valuable results that matched closely with the numerical values from the simulations. The good agreement for various phantoms also underlines the robustness of the current comparison procedure.

However, as soon as the required tools are available, confirmation of the Loss-value by direct measurement with a network analyzer is would be helpful.

Concerning the magnitude of the H_1^+ field, for different phantoms a connection between the loading of the coil and the necessary input power for achieving a certain flip angle was observed.

The B_1^+ field magnitude values delivered by the simulations differed slightly with the mesh size, suggesting that the quality of the simulations increases for finer mesh grids. The figures of the comparisons of the four different phantoms showed a very good match between simulation and experimental data. This certainly verifies the validity of the simulations of the H_1^+ field distribution within the phantoms.

The presented comparisons are, to my knowledge, the precisest comparisons between MRI experiments and simulations that are currently available (Compare [de Moortele et al., 2005][Collins et al., 2005][Collins & et al., 2002][Ibrahim et al., 2007][Yang & et al., 2002][Tropp, 2004]). And they are the only ones that provide a comparison of phantoms with a realistic shape.

Chapter 7

Conclusion

The 7T whole body MR scanner from Siemens is an experimental device used only for research so far. Therefore, concerning the operating system, many different issues appeared during the course of this diploma thesis which demanded thorough investigation of the scanner hardware. Investigated were the imaging coils and their field profile, as well as the scanner software e.g. the adjustment methods or the amplitude recalculation for the various pulses.

Several different B_1^+ mapping methods have been tested to find the method that is most suitable for performing the experiments. Due to the intrinsic knowledge of the magnitude of the transmit field for a certain flip angle inherent to an imaging sequence with rectangular pulses, the double angle method with one rectangular pulse per repetition period proved to be the most adequate for a quantitative comparison of the magnitude data of the simulations and experiments.

Other B_1^+ mapping methods which are advantageous in terms of the scanning time have also been implemented and are therefore easily available also for further use in other experiments where only information about the B_1^+ field profile is important.

Recently, with the help of the acquired B_1^+ and B_1^- maps of simple oil phantoms, it was possible to discover tuning problems of an imaging coil which resulted in a decrease of the image quality. A coil with better performance reduced this prob-

lem, leading to an increase of the image quality.

Aqueous phantoms with the purpose of varying the load of the coil have been constructed and delivered some insight in the influence on the magnitude of the B_1^+ field within phantoms with a different load.

For the construction of phantoms closer to the human anatomy, gel phantoms were prepared. Examination of the influence of various ingredients on the conductivity, permittivity, rigidity as well as longitudinal relaxation time have made it possible to prepare a phantom exactly adjusted to one's needs. A manual for the creation of a realistic head phantom is also provided in this thesis. In terms of the ease of construction, price, adjustability of the electromagnetic properties and maintenance of the shape without external support, an imitation of the human head by taking a plastic skull as a base and different agar agar gel mixtures to simulate different human tissues provided the best results.

The durability could also be improved by adding preservatives and also through the wrapping of the phantom. Further experiments are necessary, trying to extend this even further by completely preventing any water evaporation by sealing the phantoms with mixtures containing carnauba wax as used in the sweets industry.

Another improvement of the phantoms would be an even more realistic anatomy by implementing air spaces, e.g the sinuses into the head. This was limited so far by the inability during the segmentation process to differentiate between the skull which has no signal in the MRI scanner and air gaps, which also do not provide any signal. Between the skull and air outside this is still possible because there is a thick enough layer of material in between, but between the skull and air gaps which simulate the sinuses etc. this layer would be either partially not existent or too thin to provide a sufficient signal. A solution to this problem could be a CT scan of the complete phantom and then a subsequent registration with the MRI data. This way a reliable segmentation for providing the 3D data for the simulations could still be possible.

Overall, the experiments with various phantoms have shown very good agreement with the simulations concerning the distribution of the B_1^+ field inside the examined object. The comparisons of the field distribution and the magnitude of the field in Section 6.5 are the precisest comparisons currently available and show a very good match between simulation and experiment. The comparison of the magnitude values also delivered quite realistic results after consideration of the various components of the RF circuit between the TALES and the imaging coil. For really hard evidence of a match of the magnitude in the experimental and simulation data, a measurement of the Loss-value with the help of a network analyzer would be valuable. This could not be performed to date due to the missing hardware, but with regard to the available information about the properties of the RF circuit components a confirmation of the validity of the achieved results is expected.

Since the reliability of the simulations is proven with the help of the provided experimental results, they can certainly be used for the examination of the effects of the RF field on the human subject. For this purpose various different scenarios have to be tested. Different head sizes and varying head positions have a strong impact on the SAR value. 3D electromagnetic simulations can therefore be used for a fast evaluation of the power deposition within the subject during various worst case scenarios such as small head size or close proximity of certain body parts to the coil elements.

Furthermore phantoms such as the head model can be used as a tool for testing out various imaging sequences and prove further simulation results concerning RF effects on human tissue. Temperature mapping experiments can provide further experimental evidence concerning the effects of electromagnetic waves on an examined object. In these experiments, the temperature increase of a sample after exposure to RF radiation during an imaging experiment can be measured and hence provide very valuable information regarding the safety of a human subject in an MRI scanner.

Appendix

.1 MatLab scripts

.1.1 Permutebox.m

```
% In this script the variable "Box" represents the
3D matrix with the MRI data. It can be used for
images converted to MatLab data with the program
miconv.exe (Version 29.08.07)

% transformation from the MatLab coordinate system to the
%simulation coordinate system (y,z,x) -> (x,y,z)

Box_permute=permute(Box,[3 1 2]);

% change z-direction to match z-direction in simulation
Box_permute_flip=flipdim(Box_permute,3);

% export data to the file "Phantombox"
fid = fopen('/scr/clemens1/B1Map_080627_Markersugarbottle
/tfl/Phantombox','w');
fwrite(fid,Box_permute_flip);
fclose(fid);
```

.1.2 Import.m

```
% Determine the size of the data
sizedata=size(data,1);
m=sqrt(sizedata);

% Delete the rows that just contain spatial information
data(1:(3.*sizedata))=[];

% Fill a quadratic matrix with the magnitude values
% of the B1 field. (Just works in this form if the data
% was made available in a quadratic form

Magnitude=reshape(data,m,m);
```

.2 Productlist

Product	Manufacturer	Retailer
Sodium Chloride ($NaCl$)	Alfa Aesar	SAP markets
Sucrose (Saccharose)	Suedzucker	Supermarket
	USB Europe GmbH	SAP markets
Manganese(II) Chloride tetrahydrate	Sigma-Aldrich	SAP markets
Copper(II) sulfate pentahydrate	Alfa Aesar	SAP markets
Gadolinium(III) Chloride hexahydrate	ALEXIS	SAP markets
Nickel(II) sulfate hexahydrate	Alfa Aesar	SAP markets
Sodium azide (NaN_3)	Sigma-Aldrich	SAP markets
ι -carrageenan	Fluka	SAP markets
κ -carrageenan	Fluka	SAP markets
Agarose	Sigma-Aldrich	SAP markets
Agar agar	cant't read it, it's Thai	Asia market
Polyvinyl alcohol Moviol	Kuraray	www.kuraray.co.jp
Natrosol 250 Pharm HEC HX	Fagron	www.fagron.de
TX-151	Oil research center Intl.	www.oilcenter.com
Polyethylene powder	Sumitomo Seika Chemicals	Sumitomo Seika
Quick Lac	Alfred L. Wolff GmbH	www.alwolff.com
Quick Oil	Alfred L. Wolff GmbH	www.alwolff.com
Quick Gum 8048	Alfred L. Wolff GmbH	www.alwolff.com
Plastic skull	Anatomical Chart Company	www.anatomical.com
	Erler-Zimmer	www.erler-zimmer.de
Head Model	Moch - Figuren GmbH	www.moch.com

Table 1: The products that were used for experiments. SAP markets is a so called Supplier-Relationship-Management Service that is used by the Max-Planck-Society for purchasing products at different suppliers.

List of Figures

2.1	Energy levels of the hydrogen atom	7
2.2	Rotating frame of reference	9
2.3	Motion of M around effective field B_{eff}	10
2.4	Single frequency pulse	11
2.5	Rectangular pulse	11
2.6	Sinc pulse	12
2.7	Recovery of the magnetization after an RF pulse	14
2.8	Transversal relaxation	15
2.9	Free induction decay	17
2.10	Spin echo	17
2.11	Decaying amplitude of multiple echoes	18
2.12	Shielding of the magnetic field	19
2.13	Structure and chemical shift of water	20
2.14	Structure and chemical shift of sucrose	20
2.15	Maxwell coil	23
2.16	Timing diagram for a GRE sequence	25
2.17	Transverse magnetization after a low flip angle	26
3.1	Signal intensities versus inversion time	33
3.2	B_1^+ maps of water and gel phantom	40
3.3	NaCl - conductivity relation	42
3.4	Sucrose - permittivity relation	43
3.5	NaCl - conductivity relation for sugarmixture	44
3.6	Head mold	45
3.7	Realistic head phantom	48

3.8	Network Analyzer	49
3.9	Coaxial Probe method	50
3.10	a) The different probes used for the calibration b) Measurement of a liquid sample	52
3.11	The measured parameters of acetone	53
3.12	The measured parameters of the sugar-water mixture	54
3.13	The measured parameters of the Siemens phantom 5512 608 K2205	54
4.1	Headphantom with bright center	61
4.2	Damping of dielectric resonance	62
4.3	Field focusing in a water phantom	63
4.4	Interference between coil elements	65
4.5	Steady state	68
4.6	B_1^+ map - Double angle method (GRE)	70
4.7	Noisy B_1^+ maps	71
4.8	The functions $\sin \varphi$ and $\sin^3 \varphi$	73
4.9	B_1^+ map - Double angle method (SE)	73
4.10	Multi angle method - fit	75
4.11	B_1^+ and B_1^- maps - Multi angle approach	76
4.12	Timing diagram of Siemens WIP B_1^+ mapping sequence	77
4.13	B_1^+ map - Siemens WIP package	79
4.14	Transverse magnetization for different TR	79
4.15	B_1^+ map - Signal null method	81
4.16	Fitting problem - signal null method	81
4.17	Double-delayed spoiled gradient-echo pulse sequence	82
5.1	Taskcard "Routine"	86
5.2	Positioning the slices	87
5.3	The 3 different imaging planes	88
5.4	Folding artifact	89
5.5	Taskcard "Contrast"	90
5.6	Taskcard "Resolution"	91
5.7	Taskcard "Geometry"	91
5.8	Taskcard "System,Transmitter/Receiver"	92

5.9	Reference pulse - pulse recalculation	93
5.10	Flip angle maps for different coils	96
5.11	Profiles of flip angle maps for different coils	96
5.12	Experimental adjustment - rectangular pulse	100
5.13	Flip angle maps for different pulse shapes	101
5.14	Experimental adjustment - selective pulse	101
6.1	Simple phantoms are used for verification of the coil design	106
6.2	The procedure how 3D electromagnetic simulations can be used for acquiring knowledge about more sophisticated phantoms. . . .	107
6.3	Simulation - Experiment inconsistency	109
6.4	Inhomogeneity of the B_1^+ field for different coil positions	110
6.5	Comparison procedure - CST	111
6.6	Comparison procedure - HFSS	113
6.7	Bias field	114
6.8	Phantom with attached markers inside Rapid coil	116
6.9	Markers defining coil center	117
6.10	Translation from image image center to coil center	118
6.11	Z-position of coil center within magnet	118
6.12	The MatLab program "ComparisonGUI.m"	119
6.13	The MatLab program "Compare.m"	120
6.14	Shape of the phantom within simulation	121
6.15	The correlation function finds the maximum correlation for the superposition of experimental and simulation data.	122
6.16	Recalculation from a selective pulse to a rectangular pulse. . . .	126
6.17	sinc pulse - central lobe	128
6.18	Pulse shape in the IDEA Poet sequence simulation tool	129
6.19	The pulse shape for of the actually applied pulse fitted with MatLab.	130
6.20	Recalculation from the selective pulse (left) to the corresponding rectangular pulse (right)	130
6.21	Comparison H_1^+ map: Selective and rectangular pulse	132
6.22	The circuit between power amplifier and coil	133
6.23	Different ROI sizes used for comparison	135
6.24	Loss value for different mesh sizes	138

6.25	Comparison orange oil phantom - transversal	139
6.26	Comparison orange oil phantom - coronal	139
6.27	Comparison orange oil phantom - sagittal	139
6.28	Simulation objects - Sugarphantom	141
6.29	Comparison Sugarphantom - transversal	142
6.30	Comparison Sugarphantom - coronal	142
6.31	Comparison Sugarphantom - sagittal	143
6.32	Phase shift of coil elements	144
6.33	Comparison skull - transversal	146
6.34	Comparison skull - coronal	146
6.35	Comparison skull - sagittal	147
6.36	Head phantom - segmented data	148
6.37	Comparison head - transversal	149
6.38	Comparison head - coronal	149
6.39	Comparison head - sagittal	149
6.40	H_1^+ map invivo - sagittal	150

List of Tables

3.1	Different ingredients and their properties	31
3.2	T_1 times for different concentrated $MnCl_2$ solutions	33
3.3	Different kinds of aqueous phantoms	34
3.4	Ingredients of the gel and the water phantom	39
3.5	Dielectric properties of different tissue types	40
3.6	Ingredients for a realistic head phantom	45
4.1	B_1^+ mapping methods	83
5.1	The orientation of the slices in the scanner and the corresponding slices in the simulations	87
5.2	Comparison of the SAR values for the Invivo and the Rapid coil .	95
5.3	The mean flip angles for the transversal slice through the coil center of Invivo and Rapid coil	97
5.4	Results of the manual adjustment for different starting values . . .	99
5.5	The difference in flip angle for different pulse shapes	100
5.6	The reference amplitude estimated with different adjustment meth- ods for the orange oil phantom in the Invivo coil	102
6.1	H_1^+ field comparison - sinc pulse	129
6.2	H_1^+ field comparison - pulse from IDEA	131
6.3	Comparison of the magnitude of the H_1^+ field in Phantom046 (Table 3.3). The calculation of the magnitude of the experimen- tal data is based on a rectangular pulse with pulse length $\tau =$ $2,56\text{ ms}$	133

6.4	Influence of the ROI on the loss value	136
6.5	Phantoms with different load	136
6.6	Magnitude of the H_1^+ field for different phantoms	137
6.7	H_1^+ field comparison - Orange oil phantom	140
6.8	H_1^+ field comparison - Sugarphantom	143
6.9	H_1^+ field comparison - Skullphantom	147
6.10	Properties of the head phantom	148
6.11	H_1^+ field comparison - Skullphantom	150
6.12	Head phantom - invivo	151
1	Productlist	159

References

- Agilent. (2005). *Basics of measuring the dielectric properties of materials*.
- Atkinson, D. J., Burstein, D., & Edelmann, R. R. (1990). First-pass cardiac perfusion: evaluation with ultrafast mr imaging. *Radiology*, 174, 757–762.
- Bernstein, M. A., King, K. F., & Zhou, X. J. (2004). *Handbook of mri pulse sequences*. Elsevier Academic Press.
- Bloch, F. (1946). Nuclear induction. *Physical Review*, 70, 460–474.
- Bodenhause, G., Freeman, R., & Turner, D. L. (1977). Supression of artifacts in 2d j spectroscopy. *Journal of Magnetic Resonance*, 27, 511–514.
- Bottomley, P. A., & Andrew, E. R. (1978, July). *Rf magnetic field penetration, phase shift and power dissipation in biological tissue: implications for nmr imaging*. (No. 4).
- Bottomley, P. A., Redington, R. W., Edelstein, W. A., & Schenck, J. F. (1985, August). *Estimating radiofrequency power deposition in body nmr imaging*. (No. 4).
- Bruker*. (www.bruker-biospin.com).
- Chou, C. K., Chen, G. W., Guy, A. W., & Luk, K. H. (1984). *Formulas for preparing phantom muscle tissue at various radiofrequencies*. (No. 4).
- Collins, C. M., & et al. (2002). Different excitation and reception distributions with a single-loop transmit-receive surface coil near a head-sized spherical phantom at 300 mhz. *Magnetic Resonance in Medicine*, 47, 1026–1028.
- Collins, C. M., Liu, W., Schreiber, W., Yang, Q. X., & Smith, M. B. (2005, February). *Central brightening due to constructive interference with, without, and despite dielectric resonance*. (No. 2).
- Cunningham, C. H., Pauly, J. M., & Nayak, K. S. (2006, June). Saturated double-

- angle method for rapid b1+ mapping. *Magn Reson Med*, 55(6), 1326–33.
- de Moortele, P.-F. V., Akgun, C., Adriany, G., Moeller, S., Ritter, J., Collins, C. M., et al. (2005, December). *B(1) destructive interferences and spatial phase patterns at 7 t with a head transceiver array coil*. (No. 6).
- Demtröder, W. (1999). *Experimentalphysik 2* (2. ed.). Springer.
- Dowell, N. G., & Tofts, P. S. (2007, September). *Fast, accurate, and precise mapping of the rf field in vivo using the 180 degrees signal null*. (No. 3). *Easy measure*. (www.easymeasure.co.uk).
- Feiweier, T. (2006). *B1-mapping sequence, ice and protocol works-in-progress package*.
- Gabriel, C. (1995). Compilation of the dielectric properties of body tissues at rf and microwave frequencies. *Physics Department, King's College London*.
- Hahn, E. L. (1950). Spin echoes. *Physical Review*, 80, 580–594.
- Hartsgrove, G., & Surowiec, A. (1987). Simulated biological materials for electromagnetic radiation absorption studies. *Bioelectromagnetics*, 8, 29–36.
- Hennig, J. (1991). Echoes-how to generate, recognize, use or avoid them in mr-imaging sequences. *Concepts in Magnetic Resonance*, 125–143.
- Hornak, J. P. (<http://www.cis.rit.edu/htbooks/mri/>). *The basics of mri*.
- Hoult, D. I. (2000). The principle of reciprocity in signal strength calculations - a mathematical guide. *Concepts in Magnetic Resonance*, 12.
- Hoult, D. I., & Phil, D. (2000, July). *Sensitivity and power deposition in a high-field imaging experiment*. (No. 1).
- Hue, Y. K., & Ibrahim, T. (2008). Detailed experimental and computational analyses of the rf field at 7t: Effects of the load content on achieving 90o tip without sar/power violations. *ISMRM*(77).
- Ibrahim, T. S., Mitchell, C., Abraham, R., & Schmalbrock, P. (2007, February). *In-depth study of the electromagnetics of ultrahigh-field mri*. (No. 1).
- Insko, E. K., & Bolinger, L. (1993). Mapping of the radiofrequency field. *Journal of Magnetic Resonance*, 103, 82–85.
- Ito, K. (2001). Development and characteristics of a biological tissue-equivalent phantom for microwaves. *Electronics and Communications in Japan*, 84(4).
- Kato, H., Kuroda, M., Yoshimura, K., Yoshida, A., Hanamoto, K., Kawasaki, S.,

- et al. (2005, October). *Composition of mri phantom equivalent to human tissues*. (No. 10).
- Mano, I., Goshima, H., Nambu, M., & Iio, M. (1986, December). *New polyvinyl alcohol gel material for mri phantoms*. (No. 6).
- Mazzara, G. P., Briggs, R. W., Wu, Z., & Steinbach, B. G. (1996). Use of a modified polysaccharide gel in developing a realistic breast phantom for mri. *Magnetic Resonance Imaging*, 14.
- Nolting, W. (1997). *Grundkurs theoretische physik 3 elektrodynamik* (5. ed.). vieweg.
- Onishi. (2005, September). Biological tissue-equivalent agar-based solid phantoms and sar estimation using the thermographic method in the range of 3-6 ghz. *IEICE Trans. Commun.*, E88-B(9).
- Röschmann, P. (1987). *Radiofrequency penetration and absorption in the human body: limitations to high-field whole-body nuclear magnetic resonance imaging*. (No. 6).
- Saylor, C., & Reza, S. (2006). Excitation of a tem mode in a birdcage resonator. *ISMRM*(1387).
- Schmitt, F., Stehling, M. K., Turner, R., & Mansfield, P. (1998). *Echo planar imaging*. Springer.
- Shmueli, K., Thomas, D. L., & Ordidge, R. J. (2007). Design, construction and evaluation of an anthropomorphic head phantom with realistic susceptibility artifacts. *Journal of Magnetic Resonance*, 26, 202–207.
- Slichter, C. P. (1992). *Principles of magnetic resonance* (Vol. 3). Springer.
- Stogryn, A. (1971, August). Equations for calculating the dielectric constant of saline water. *IEEE Transactions on Microwave Theory and Techniques*, 733–736.
- Stollberger, R., & Wach, P. (1996, February). *Imaging of the active b1 field in vivo*. (No. 2).
- Tropp, J. (2004). Image brightening in samples of high dielectric constant. *Journal of Magnetic Resonance*, 167, 12–24.
- Tsuwi, J. (2007). *Permittivities of measured common solvents, eps' and eps''*.
- Vaughan, J. T., Hetherington, H. P., Otu, J. O., Pan, J. W., & Pohost, G. M. (1994, August). *High frequency volume coils for clinical nmr imaging and*

- spectroscopy*. (No. 2).
- Wade, T. (2007). Comparison of current b1-mapping techniques. *ISMRM*.
- Wang, J., Mao, W., Yang, Q., Smith, B. M., & Constable, T. R. (2005, September). Measurement and correction of transmitter and receiver induced nonuniformities in vivo. *Magnetic Resonance in Medicine*, 53, 408–417.
- Weisser, A., & Lanz, T. (2006). A volume head array with 8 transmit / receive channels for 7t. *ISMRM*(2591).
- Yang, Q. X., & et al. (2002). Analysis of wave behaviour in lossy dielectric samples at high field. *Magnetic Resonance in Medicine*, 47, 982–989.
- Yang, Q. X., Wang, J., Collins, C. M., Smith, B. M., Zhang, X., Ugurbil, K., et al. (2004). Phantom design method for high-field mri human systems. *Magnetic Resonance in Medicine*, 52, 1016–1020.
- Yarnykh, V. L. (2007, January). *Actual flip-angle imaging in the pulsed steady state: a method for rapid three-dimensional mapping of the transmitted radiofrequency field*. (No. 1).
- Yoshimura, K., Kato, H., Kuroda, M., Yoshida, A., Hanamoto, K., Tanaka, A., et al. (2003, November). *Development of a tissue-equivalent mri phantom using carrageenan gel*. (No. 5).

Acknowledgements

I hereby want to thank all the people who supported me during the course of this Diplom thesis.

Foremost I would like to thank Prof. Dr. Turner for providing me with the topic for this thesis and his continual support during the course of my work. Under his leadership there is always a very good working atmosphere within our Neuro-physics group.

Furthermore I would like to thank Prof. Dr. Käs for sparking my interest in the field of neuroscience and his help in finding this topic.

I am very grateful for the constant support from Dr. Kozlov throughout the whole course of this thesis. He provided all the simulations and he was always very helpful and quick when I had some questions or when he was checking my work. Also thank you very much to Prof. Dr. Kremer for giving me the possibility to make dielectric measurements in his laboratories.

Thank you very much to Dr. Robberd Trampel for patiently answering all my questions, checking the whole thesis and being a reliable victim during our conferences on the fourth floor.

I would also like to thank Dr. Robin Heidemann for his advice and his answers on hardware related questions.

Thank you very much to Enrico Reimer. Without him I would have probably ended up writing my thesis by hand instead of using the computer with this very convenient Linux system.

I want to thank Aline Dathe for being always there for me when I needed support. And I must admit that she was a much better Ombudsperson than Archibald Winterbottom!

Furthermore I want to thank James Dedrick for checking my English and especially for marking all my comma errors, which I happened to make, during this thesis.

Thank you also to the people from the NMR group, Stefan Hetzer, Dirk Müller and Christian Labadie for their help concerning several of my problems.

The whole group I was working with was really wonderful and made the work here at the Max Planck Institute a really enjoyable time!!! Thank you to everybody for being here, bringing me some Spongebob souvenirs from abroad, accompanying me for lunch and all the other things that made my time over here a time to remember.

I want to thank my parents for their constant assistance during my whole study. I could always rely on them and they made my physics study here in Leipzig possible.

And finally thank you to Ayuko for giving me always something to look forward to and being always there for me.

I will miss you all when I will be in Japan!!!

Selbstständigkeitserklärung

Hiermit erkläre ich, dass ich die vorliegende Arbeit selbstständig und nur unter Verwendung der angegebenen Literatur, Geräte und Hilfsmittel angefertigt habe.

Ort, Datum

Unterschrift

Erklärung für die Bibliothek

Hiermit erkläre ich mich einverstanden, dass meine Diplomarbeit nach positiver Begutachtung zur Nutzung in der Zweigstelle der Universitätsbibliothek zur Verfügung steht.

Ort, Datum

Unterschrift